

https://dspace.org/

MXene-based nanostructures for electrochemical CO oxidation

Hussien, Belal Salah Mohammed

2024

https://hdl.handle.net/10539/37478

Downloaded from a DSpace repository. https://dspace.org/



MXene-based nanostructures for electrochemical CO oxidation.

BY

Belal Salah Mohammed Hussien

Student Number: 2435467

A dissertation submitted to the Faculty of Science, University of the Witwatersrand, Johannesburg, in fulfillment of the requirements for the degree of Master of Science.

Supervisors: Prof. Kenneth I. Ozoemena, Prof. Aboubakr M. Abdullah, and Dr. Kamel Eid.

University of the Witwatersrand, Johannesburg, 2022

DECLARATION

I declare that this dissertation is my own, unaided work. It is being submitted for the Degree of Master of Science at the University of the Witwatersrand, Johannesburg. It has not been submitted before for any degree or examination at any other University.



(Signature of candidate)

12 day of july 2023 at Johannesburg

ABSTRACT

2-D MXene based nanostructure owns several unique physicochemical and catalytic properties. Herein, this research used MXene ($Ti_3C_2T_x$) for the electrochemical CO_{oxid} reaction experimentally for the first time. This work divided to two sections, the first is using mono metal decorated $Ti_3C_2T_x$ and the second using binary metals decorated $Ti_3C_2T_x$ to investigate and compered the electrochemical CO_{oxid} reaction activity of mono and binary metals with $Ti_3C_2T_x$. At first, $Ti_3C_2T_x$ (T_X=OH, O, and F) well-ordered and highly exfoliated 2-D nanosheets used as substrate for the NPs growth and prepared via the selective chemical etching and delamination of MAX phase (Ti_3AlC_2) with sonication assistance to form $Ti_3C_2T_x$ nanosheets. After that, Mono and binary metals were prepared via using a facile method by in situ impregnation of Pd or Pt or both salts with $Ti_3C_2T_x$ in aqueous medium under sonication without using reducing agent or surfactant.

The as prepared Pt/Ti_3AlC_2, Pd/Ti_3AlC_2, and $PtPd/Ti_3AlC_2$ composition and structure were characterized by the scanning electron microscope (SEM), Energy Dispersive X-Ray Analyzer (EDX), the transmission electron microscope (TEM) equipped with high-angle annular dark-field scanning transmission electron microscopy (HAADF-SEM), energy dispersive spectrometer (EDS), The X-ray photoelectron spectroscopy (XPS) spectra and The X-ray diffraction patterns (XRD).

The electrochemical CO_{oxid} activity were explored using The cyclic voltammogram (CVs), linear sweep voltammogram (LSV), chronoamperometry (CA) and electrochemical impedance spectroscopy (EIS) for all prepared of different samples using Gamry electrochemical analyzer using a three-electrode system contains a Pt wire (counter electrode), Ag/AgCl (reference electrode), and glassy carbon ((3mm) WE) in an aqueous solution saturated with CO of three electrolytes acidic (0.1 M $HClO_4$), neutral (0.5 M $NaHCO_3$) and basic (0.1M KOH) at different sweep rate.

The first study showed the electrochemical activity and effect of mono metals NPs of $Pd/Ti_3C_2T_x$ compared with metal-free $Ti_3C_2T_x$ in acidic electrolyte, Interestingly, $Ti_3C_2T_x$ displayed poorer CO_{oxid} activity and the integrating of Pd NPs enhance the activity, ascribed to the combination between outstanding physical and chemical properties of $Ti_3C_2T_x$ and the catalytic advantages of Pd. In contrast, the second study the electrochemical CO_{oxid} activity for binary compared with mono NPs decorated $Ti_3C_2T_x$. Results showed PdPt/ $Ti_3C_2T_x$ was substantially superior to Pd/ $Ti_3C_2T_x$, Pt/ $Ti_3C_2T_x$, and metal-free $Ti_3C_2T_x$ in three electrolytes experimentally, owing to the electronic and synergetic effect of PdPt and physiochemical properties of $Ti_3C_2T_x$. This study may pave the way for the employment of $Ti_3C_2T_x$ in electrochemical CO_{oxid}.

DEDICATION

I dedicate my dissertation work to my whole family and friends. A special feeling of gratitude to my loving parents, and my wife whose words of encouragement and push for tenacity ring in my ears.

I also dedicate this dissertation to my supervisors (Prof. Kenneth Ozoemena, Prof. Aboubakr Abdullah, and Dr. Kamel Eid.) who have supported me throughout the process. I will always appreciate all they have done, especially Dr. Kamel Eid for helping me continuously to develop my skills.

ACKNOWLEDGEMENTS

I would like to express my gratitude and deep thanks to Professor Kenneth Ozoemena, Professor Aboubakr M. Abdullah, and Dr. Kamel Eid for the great chance to work on this interesting project. There are not enough words to thank you for your continuous support since the first day of my registration, patience, guidance all the time.

I am thankful to Dr. Kamel Eid and Professor Aboubakr M. Abdullah for assisting me in using the chemistry lab for the electrochemical CO_{oxid} application at Qatar University and the different analysis techniques for the materials characterization.

Many thanks to all members of the School of Chemistry who assisted me on my MSc journey. Special thanks to Dr. Adewale of the Ozoemena group for helping me get settled and finding my wayaround Wits University and my project.

I would also love to express my sincere appreciation for financial support by (i) the Qatar National Research Fund (QNRF, a member of the Qatar Foundation) through the National Priority Research Program Grant (NPRP) NPRP12S-0227-190168, (ii) International Research Collaboration Co-Fund grant, IRCC-2021-015 and (iii) the South African National Research Foundation (NRF). And the Open Access funding is provided by the Qatar National Library (QNL)

My heartfelt gratitude to the Ozoemena family for supporting and to my family and friends for good wishes.

RESEARCH OUTPUT ARISING FROM THIS WORK

PUBLICATION

. **Salah, B**., Eid, K., Abdelgwad, A. M., Ibrahim, Y., Abdullah, A. M., Hassan, M. K., & Ozoemena, K. I. (2022). Titanium Carbide (Ti3C2Tx) MXene Ornamented with Palladium Nanoparticles for Electrochemical CO oxidation. Electroanalysis, 34(4), 677-683. (doi.org/10.1002/elan.202100269).

. Ahmed Abdelgawad, Belal Salah, Kamel Eid, Aboubakr M. Abdullah, Rashid S. Al-Hajri, Mohammed Al-Abri, Mohammad K. Hassan, Leena A. Al-Sulaiti, Doniyorbek Ahmadaliev, andKenneth I. Ozoemena. Pt-Based Nanostructures for Electrochemical Oxidation of CO: Unveiling the Effect of Shapes and Electrolytes. Int. J. Mol. Sci. 2022, 23(23), 15034; (doi.org/10.3390/ijms232315034)

MANUSCRIPTS FOR PUBLICATION

. **Belal Salah**, Kamel Eid, Abobakr Abdullah, and Kenneth I. Ozoemena. PdPt Nanoparticles Supported Ti3C2Tx MXene for Electrochemical CO oxidation Over a Wide pH Range. (answer question and resubmitted to Energy & Environmental Science RSC publisher **impact factor= 38.5**)

CONFERENCE PRESENTATIONS

Belal Salah, Kamel Eid, Abobakr Abdullah, and Kenneth I. Ozoemena. Controlled fabrication of Titanium Carbide ($Ti_3C_2T_x$) MXene Decorated with Palladium Nanoparticles for Electrochemical CO oxidation. 2021 international conference on materials science and engineering Brisbane, Australia.

Belal Salah, Kamel Eid, Abobakr Abdullah, and Kenneth I. Ozoemena. Controlled fabrication of Titanium Carbide ($Ti_3C_2T_x$) MXene Decorated with Palladium Nanoparticles for Electrochemical CO oxidation. Qatar University Annual Research Forum and Exhibition October 3-4, 2022, Qatar.

Table of Contents

DECLARATION 2
ABSTRACT 3
DEDICATION 4
ACKNOWLEDGEMENTS 5
RESEARCH OUTPUT ARISING FROM THIS WORK 6
PUBLICATION 6
MANUSCRIPTS FOR PUBLICATION 6
CONFERENCE PRESENTATIONS 6
LIST OF FIGURES 10
LIST OF SCHEMES 13
LIST OF TABLES 13
LIST OF ABBREVIATIONS AND NOMENCLATURE 13
Chapter 1 17
INTRODUCTION 17
Motivation and Rationale 17
Statement of Research Problem 17
Research Aims and Objectives 18
Structure of the Dissertation 18
Refrences ..... **Error! Bookmark not defined.**
Chapter 2 20
Introduction 20
Carbon monoxide sources 20
Effects of Carbon monoxide 21
Effects on the human health 21
Effects on the plant 22
Effects on the environment 22

Carbon monoxide oxidation (reactions mechanisms) 23
Carbon monoxide oxidation methods 23
Thermal CO oxidation 24
Photocatalytic CO oxidation 26
Electrochemical CO oxidation 28
Parameters effect on the CO oxidation activity 30
Carbon-based materials 33
References 38
CHAPTER 3 43
Abstract 43
Introduction 43
Experimental 44
Chemicals and materials 44
Synthesis of Ti3C2Tx nanosheets 44
Synthesis of Pd/Ti3C2Tx 45
Materials characterization 45
Electrochemical CO oxidation reaction 45
Results and discussion 45
Conclusion 51
References 51
CHAPTER 4 54
Abstract 54
Graphical Abstract 54
Introduction 54
Results and discussion 56
Electrocatalytic CO oxidation activity in acidic media 62
CO oxidation activity in neutral electrolyte 65

CO oxidation activity in alkaline electrolyte 66
Conclusions 68
Experimental methods 68
Chemicals and materials 68
Synthesis of $Ti_3C_2T_x$ nanosheets 69
Synthesis of PdPt/$Ti_3C_2T_x$ 69
Materials characterization 69
Supporting information 69
Electrochemical CO oxidation reaction 69
References 74
Chapter 5 77
Conclusion 77
Chapter 1 77
Chapter 2 77
Chapter 3 77
Chapter 4 78
Future Prospects 79

LIST OF FIGURES

Figure 2.1 : The anthropogenic sources of CO emissions. Data is obtained from ref [19]

Figure 2.2 : The effect of CO gas on human health.

Figure 2.3: (a) SEM image and (b) TEM image of Pd/Cu/gC_3N_4NTs and (c) CO conversion efficiency related to the temperature. copyright permission Elsevier [10] (d) SEM image, and (e) TEM of the as-prepared CeO_2-ZnO. (c) the XRD, and (f) Thermal CO_{oxid} for the prepared catalysts. Copyright permesiion elsevir [28].

Figure 2.4: (a) SEM image Cu_2O/g-C_3N_4-4 (b) TEM and (c) Catalytic activities of Cu_2O and Cu_2O/g-C_3N_4. Copyright permission RSC [32].

Figure 2.5: (a) Photocurrent–voltage relations of Pt/TiO_2 catalysts: a1, b1, c1 denote Pt content 0.5, 1, 2 wt.% stabilized under N_2 respectively. a2, b2, c2 denote Pt content 0.5, 1, 2 wt.% annealed in air respectively. (b) Pt/TiO2 was annealed at 423 K for 2 h under N_2 and then annealed at 673 K under air for 2 h, copyright permission from Elsevier [41].

Figure 2.6: (a) TEM of RP-AH, (b) Transient photocurrent response of prepared catalysts at a bias of10 mV vs SCE under UV irradiation, (c) A- Photocatalytic CO_{oxid} for the prepared catalyst, B- The stabilty recycling test of RP-AH. Copyright permission ACS 2016 [42].

Figure 2.7: (a) TEM image of multicubic PtNi, and (b) CO-stripping in (1 M) KOH electrolyte at a scan rate of 50 mVs^{-1}, Copyright permission RSC [48]. (c) TEM image of PtPdRu NDs, and (d) CO-stripping CV of different catalysts measured in 1 M NaOH CO-saturated at rate of 50 mVs^{-1} and Copyright permission RSC [51].

Figure 2.8: (a) SEM images, (b) TEM image of PtPd/gC_3N_4 nanorods. CVs in a CO-saturated aqueous solution of 0.1 M KOH at rate of 50 mVs^{-1} (c) in dark, and (d) under the light. Copyright permission RSC [6].

Figure 2.9: (a) CO_{oxid} conversation versus temperature over supported noble metal. Copyright permission 2010, Elsevier [54]. (b)TEM of the prepared Pd/COP-4 in DMF and water, and (C)the CO_{oxid} of Pd/COP-4 prepared by different solvents. Copyright permission 2013, RSC [55].

Figure 2.10: (a) Top and side views of the charge density difference of Pd/OV–Mo_2CO_2 (b) Reaction mechanism of CO_{oxid} via TER-mechanism, and (c) Adsorption configurations and adsorption energies. copyright permission RSC [60].

Figure 2.11: (a) The diagram for Cu3 active site of Cu_3/d-Mo_2CO_2 works as an electron reservoir to facilitate the CO_{oxid} conversation rate. (b) CO_{oxid} pathways reactions (side views) over Cu_3/d-Mo_2CO_2 by diffrent mechanisms. Copyright 2018, American Chemical Society [61].

Figure 2.12: Periodic tables showing compositions of MXenes and MAX phases. (a) Elements of MXenes chemical structure. (b) Elements of different MAX phases, Copyright 2019 American Chemical Society [67].

Figure 2.13: (a) the chemical structure for MAX and MXene phase (b) Schematic illustration of the development path of MXenes synthesis. Copyright 2022 Elsevier [69].

Figure 3.1: (a-b) SEM image of $Ti_3C_2T_x$ MXene. SEM image (c) and TEM images (d-e) of Pd/$Ti_3C_2T_x$, HRTEM (f) of the marked area in (e).

Figure 3.2: (a) SAED and elemental mapping images of (b) Ti, (c) C, (d) O, (e) F, and (f) Pd of Pd/$Ti_3C_2T_x$.

Figure 3.3: XRD analysis of Pd/$Ti_3C_2T_x$ and $Ti_3C_2T_x$.

Figure 3.4: (a) XPS survey of Pd/$Ti_3C_2T_x$ and $Ti_3C_2T_x$. High-resolution XPS spectra of (b) Ti, (c) C, (d) O, (e) F, and (f) Pd.

Figure 3.5: (a) CVs measured in a N_2 saturated 0.1 M $NaHCO_3$ of Pd/$Ti_3C_2T_x$ and $Ti_3C_2T_x$. (b) CVs and (c) LSV of Pd/$Ti_3C_2T_x$ and $Ti_3C_2T_x$. (d) CVs measured at different scan rates in a CO-saturated an aqueous solution of 0.1 M $HClO_4$ at 50 mV s^{-1} and (e) the corresponding plots of forwarding peak currents against the square root of the scan rates. (f) EIS of Pd/$Ti_3C_2T_x$ and $Ti_3C_2T_x$ measured in a frequency range from 100 kHz to 5 Hz with an AC voltage amplitude of 0.8 V at an open circuit potential in 0.1 M $HClO_4$.

Figure 3.6: (a) The I-T tests measured for 2000 s at 0.8 V in a CO-saturated 0.1 M $HClO_4$, (b) TEM image of Pd/$Ti_3C_2T_x$ after CO_{oxid} stability test.

Figure 4.1: images of SEM for (Ti_3AlC_2 MXene, (b) Pd/$Ti_3C_2T_x$, (c) Pt/$Ti_3C_2T_x$, (d-e) PdPt/$Ti_3C_2T_x$. (f-g) TEM images of PdPt/$Ti_3C_2T_x$ and (i) HRTEM of PdPt NPs and (j) SAED of PdPt NPs The fabrication process of PdPt/$Ti_3C_2T_x$.

Figure 4.2: Elemental mapping of elements for PdPt/$Ti_3C_2T_x$: (a) HAADF/STEM, (b) Ti, (c) C, (d) O, (e) F, (f) Pt, (g) Pd. (h) EDS, and (i) EDX.

Figure 4.3: (a) XRD and (b) XPS surveys of the as-prepared catalyst. High-resolution XPS spectra of (c) Ti, (d) C, (e) O, (f) F, and (g) Pd, and (h) Pt.).

Figure 4.4: (a) CVs, and (b) LSVs of the as-prepared catalysts. CVs measured under different scan rates in saturated 0.1 M $HClO_4$ aqueous solution by CO at 25 ^oC at 50 mV s^{-1} of (c) $PdPt/Ti_3C_2T_x$ and (e) $Pd/Ti_3C_2T_x$ with the corresponding plots of the forward peaks currents against the square root of the scan rates of (d) $PdPt/Ti_3C_2T_x$ and (f) $Pd/Ti_3C_2T_x$.

Figure 4.5: (a) CVs and (b) LSV of the as-prepared materials. CVs measured under different scan rates in saturated 0.5 M $NaHCO_3$ aqueous solution by CO at 25 ^oC at 50 mVs^{-1} of (c) of $PdPt/Ti_3C_2T_x$ (e) $Pd/Ti_3C_2T_x$ with the corresponding plots of the forward peaks currents against the square root of the scan rates (d) of $PdPt/Ti_3C_2T_x$, and (f) of $Pd/Ti_3C_2T_x$.

Figure 4.6: (a) CVs and (b) LSV of the as-prepared catalyst. CVs measured under different scan rates in saturated 0.1 M KOH aqueous solution by CO at 25 ^oC at 50 mV s^{-1} of (c) of $PdPt/Ti_3C_2T_x$ (e) of $Pd/Ti_3C_2T_x$ with the corresponding plots of the forward peaks currents vs the square root of the scan rates of (d) $PdPt/Ti_3C_2T_x$, and (f) $Pd/Ti_3C_2T_x$.

Figure 4.S1: cyclic voltammetry measured in N_2 saturated 0.1 M $HClO_4$ at 50 mV s^{-1} of the as-prepared catalyst.

Figure 4.S2: (a) The I-T tests measured for 2000 s in CO-saturated 0.1 M $HClO_4$ of $PdPt/Ti_3C_2T_x$ at 0.71 V and $Pd/Ti_3C_2T_x$ at 0.84V. CVs before and after stability tests (b) of $PdPt/Ti_3C_2T_x$, and (d) of $Pd/Ti_3C_2T_x$. LSV before and after stability tests (c) of $PdPt/Ti_3C_2T_x$, and (e) of $Pd/Ti_3C_2T_x$ tested in 0.1 M $HClO_4$ aqueous solution saturated by CO at 50 mV s^{-1} and (f) EIS of the as-prepared catalyst (frequency, 100 kHz - 5 Hz) of 0.78V in 0.1 M $HClO_4$.

Figure 4.S3*:* (a)TEM, and (b) EDX of $PdPt/Ti_3C_2T_x$ after CO_{oxid} stability test in 0.1 M HClO4*.*

Figure 4.S4: (a) The I-T tests recorded for 2000 s in CO-saturated 0.5 M $NaHCO_3$ of PdPt/ $Ti_3C_2T_x$ at 0.23 V and Pd/ $Ti_3C_2T_x$ at 0.39V. CVs before and after stability tests (b) of PdPt/ $Ti_3C_2T_x$, and (d) of $Pd/Ti_3C_2T_x$. LSV before and after stability tests (c) of PdPt/ $Ti_3C_2T_x$, and (e) of Pd/ $Ti_3C_2T_x$ tested in 0.5 M $NaHCO_3$ aqueous solution saturated by CO of at 50 mV s^{-1} and (f)) EIS of the as-prepared catalyst (frequency, 100 kHz - 5 Hz) of 0.3V in 0.5 M $NaHCO_3$.

Figure 4.S5: (a) The I-T tests measured for 2000 s in CO-saturated 0.1 M KOH of $PdPt/Ti_3C_2T_x$ at -0.19 V and $Pd/Ti_3C_2T_x$ at 0.02 V. CVs before and after stability tests (b) of $PdPt/Ti_3C_2T_x$, and (d) of $Pd/Ti_3C_2T_x$. LSV before and after stability tests (c) of PdPt/ $Ti_3C_2T_x$, and (e) of Pd/T $Ti_3C_2T_x$ tested in 0.1 M KOH

aqueous solution saturated by CO at 50 mV s^{-1} and (f) EIS of the as-prepared catalyst (frequency, 100 kHz - 5 Hz) of 0.15V in 0.1 M KOH.

LIST OF SCHEMES

Scheme 4.1: The fabrication process of PdPt/ $Ti_3C_2T_x$ N.

Scheme 4.2: The proposed CO_{oxid} mechanism on PdPt/ $Ti_3C_2T_x$ in $HClO_4$ electrolyte

LIST OF TABLES

Table 2.1: The CO_{oxid} performance for different catalysts and (T100) the temperature required for complete CO_{oxid} to CO_2.

Table 2.1: The electrochemical CO_{oxid} performance for different catalysts in different mediums.

Table 4.1: The CO adsorption capacity on thus obtained materials in different electrolytes obtained from the integration of the anodic peak current area.

Table 4.S1 Detailed XPS binding energies of Ti, C, F, O, d, and Pt in as-synthesized PdPt/ $Ti_3C_2T_x$

LIST OF ABBREVIATIONS AND NOMENCLATURE

Abbreviation	Description
2-D	two-dimensional
Ag|AgCl	Silver/Silver Chloride
BET	Branauer-Emmett-Teller
CA	Chronoamperometry

CE	Counter electrode
CH3CH2OH	Ethanol
cm	Centimeters
CPE	Constant Phase Element
CV	Cyclic Voltammetry
CO_{oxid}	CO oxidation
D.C.	Direct Current
DLC	Double Layer Capacitance
E	Ideal potential of the cell
ECSA	Electrochemically Active Surface Area
EDS	Energy Dispersive X-ray Spectroscopy
EEC	Electronic Equivalent Circuit
EIS	Electrochemical Impedance Spectroscopy
F	Faraday's constant
FC	Fuel Cell
FWHM	Full Width at Half Maximum
GCE	Glassy carbon electrode
GDL	Gas diffusion layers
HRTEM	High resolution transmission electron microscopy
I	Current
J	Current density
jo,s	Exchange current density
jo,m	Mass activity

LSV	Linear Sweep Voltammetry
mA	Milliamperes
mm	Millimeter
mg	Milligram
min	Minutes
mL	Millilitre
N2	Nitrogen
nm	Nanometer
O2	Oxygen
Pd	Palladium
PEIS	Potentiostatic Electrochemical Impedance Spectroscopy
Pt	Platinum
PXRD	Powder X-ray diffraction
R	Resistance
Rct	Capacitive resistance
RE	Reference electrode
rpm	Revolution per minute
Rs	Series connection resistance
RT	Room temperature
s	Seconds
SEM	Scanning electron microscopy
TEM	Transmission electron microscopy
um	Micrometer
WE	WE

wt %	Weight percentage
XAS	X-Ray Absorption Spectroscopy
XPS	X-Ray Photoelectron Spectroscopy
XRD	X-Ray Diffraction
Z’	Real impedance
Z”	Imaginary impedance
θ	Scattering angle
λ	Wavelength
ω	Frequency

Chapter 1

INTRODUCTION

This chapter summarizes the motivation and objectives of this research project, as well as the structure of the dissertation.

Motivation and Rationale

The need for traditional energy alternatives such as coal and petroleum is vital to protect and enhance the surrounding environment from the effect of emitted toxic gases like CO_2, and CO that led to climate change and negatively affected living organisms [1-3]. So, clean and renewable energy is one of the most important topics in the scientific arena like solar cell energy and wind. In contrast, Proton exchange membrane fuel cells are sustainable, environmentally green, and efficient energy conversion technologies. however, poisoning by CO reduces their catalytic activity [4, 5]. Therefore, the CO_{oxid} reaction is of particular interest in industrial, fuel cells, and environmental applications. Engineering new low cost with higher activity compared to the commercial catalyst Pt/C is crucial for electrochemical CO_{oxid} [6-10]. This study paves a new avenue for the facile preparation of new catalysts via the combination of unique physicochemical properties of MXene and the superior catalytic properties of Pt and Pd mono and binary NPs. MXene is used here for the first time experimentally in electrochemical CO_{oxid} and will pave the way to use it in different electrochemical applications.

Statement of Research Problem

Electrochemical CO_{oxid} reaction is highly attractive in environmental applications due to the higher toxicity towards the living organism with low ppm concentration, and also an as undesirable product in the industry. In contrast, the CO poisoning in the proton exchange membrane fuel cells which is highly efficient energy weakens their performance [11-13]. The need for low-cost catalysts with high performance is highly important for the industry. Also, Pt and Pd are the most promising catalysts for CO_{oxid} but their high cost, stability, and self-poisonings are critical issues that faced the commercialization process. So the need for designing new low-cost catalysts for electrochemical CO_{oxid} is important with higher activity and stability [14-16]. Interestingly, the unique physicochemical properties of MXene like , abundant active sites, electron density great defects, abundant surface functionalities (i.e., O_2, OH, and F), and high electrical conductivity, which are significant merits in various catalytic applications, [17-24] when combined with the unique catalytic properties of Pt and Pd as mono or binary NPs with less than 15nm size and low amount > 3wt% found promising for electrochemical CO_{oxid}. This study used MXene for the first

time experimentally in CO_{oxid}, and will pave the way for applying it in different application.

Research Aims and Objectives

The aim of this research is to explore the feasibility of combination between the low cost with outstanding physicochemical properties of $Ti_3C_2T_x$ nanosheets and low wt% (>3) of the catalytic merits of mono and binary Pd and Pt NPs experimentally for the first time in the electrochemical CO_{oxid} application in wide PH range.

This study involves synthesizing different catalysts of mono palladium decorated $Ti_3C_2T_x$ in the first study and PtPd decorated $Ti_3C_2T_x$ in the second study, and the evolution of their physical characteristics – structural and morphological properties besides studying the catalytic effect by the combination between $Ti_3C_2T_x$ and metals NPs and catalysts effect on the electrochemical CO_{oxid} reaction properties. The electrochemical CO_{oxid} was evaluated using cyclic voltammetry (CV), linear sweep voltammetry (LSV), chronoamperometry (CA), and electrochemical impedance spectroscopy (EIS).

The microelectrochemical CO_{oxid} is designed, fabricated, and tested to prove the CO_{oxid} concept.

Structure of the Dissertation

Chapter one: discusses the rationale behind this research, as well as the aims and objectives.

Chapter two gives a brief overview of the electrochemical CO_{oxid} related to my work.

Chapter three presents the first experimental study of mono metals nanoparticles (Pt and pd) decorated MXene for the electrochemical CO_{oxid} (published in an electro analysis journal).

Chapter four the experimental studying and comparison of electrochemical CO_{oxid} activity for mono or binary metals Nanoparticles in wide PH rang (Answer questions and resubmitted to the Energy & Environmental Science)

Finally, Chapter five concludes the dissertation and gives suggestions for future directions.

References

1. Panneerselvam, G., V. Thirumal, and H.M.J.A.o.A. Pandya, *Review of Surface Acoustic Wave Sensors for the Detectionand Identification of Toxic Environmental Gases/Vapours.* 2018: p. 357-367-357-367.
2. Lu, Q., et al., *Engineering graphitic carbon nitride (gC 3 N 4) for catalytic reduction of CO 2 to fuels and chemicals: strategy and mechanism.* 2021. **23**(15): p. 5394-5428.
3. Huang, S., et al., *Green catalysis for selective CO oxidation in hydrogen for fuel cell.* 2009. **2**(10): p. 1060-1068.
4. Wagner, N. and E.J.J.o.P.S. Gülzow, *Change of electrochemical impedance spectra (EIS) with time during CO-poisoning of the Pt-anode in a membrane fuel cell.* 2004. **127**(1-2): p. 341-347.
5. Chatterjee, S., et al., *Free standing nanoporous palladium alloys as CO poisoning tolerant electrocatalysts for the electrochemical reduction of CO2 to formate.* 2019. **9**(6): p. 5290-5301.
6. Eid, K., M.H. Sliem, and A.M.J.N. Abdullah, *Unraveling template-free fabrication of carbon nitride nanorods codoped with Pt and Pd for efficient electrochemical and photoelectrochemical carbon monoxide oxidation at RE.* 2019. **11**(24): p. 11755-11764.

7. Zheng, Y., et al., *Rational design of PdRu/TiO2 composite material for advancing electrochemical catalysis of methanol oxidation.* 2020. **472**: p. 228517.
8. Rodriguez, P., et al., *New insights into the catalytic activity of gold nanoparticles for CO oxidation in electrochemical media.* 2014. **311**: p. 182-189.
9. Li, X., et al., *Functional MXene materials: progress of their applications.* 2018. **13**(19): p. 2742-2757.
10. Talib, S.H., et al., *Non-noble metal single-atom catalyst of Co1/MXene (Mo2CS2) for COoxid.* 2021. **64**(3): p. 651-663.
11. Lu, S., et al., *One-pot synthesis of PtIr tripods with a dendritic surface as an efficient catalyst for the oxygen reduction reaction.* 2017. **5**(19): p. 9107-9112.
12. Wang, H., et al., *Fabrication of mesoporous cage-bell Pt nanoarchitectonics as efficient catalyst for oxygen reduction reaction.* 2018. **6**(9): p. 11768-11774.
13. Wei, C., et al., *A Three-Dimensionally Structured Electrocatalyst: Cobalt-Embedded Nitrogen-Doped Carbon Nanotubes/Nitrogen-Doped Reduced Graphene Oxide Hybrid for Efficient Oxygen Reduction.* 2017. **23**(3): p. 637-643.
14. Liu, X., et al., *Superior catalytic performance of atomically dispersed palladium on graphene in COoxid.* 2020. **10**(5): p. 3084-3093.
15. Xie, S., et al., *Highly Active and Stable Palladium Catalysts on Novel Ceria–Alumina Supports for Efficient Oxidation of Carbon Monoxide and Hydrocarbons.* 2021. **55**(11): p. 7624-7633.
16. Salama, R.S., et al., *Palladium supported on mixed-metal–organic framework (Co–Mn-MOF-74) for efficient catalytic oxidation of CO.* 2021. **11**(8): p. 4318-4326.
17. Li, X., et al., *Applications of MXene (Ti 3 C 2 T x) in photocatalysis: A review.* 2021. **2**(5): p. 1570-1594.
18. Tahini, H.A., X. Tan, and S.C.J.C. Smith, *Facile CO oxidation on Oxygen-functionalized MXenes via the Mars-van Krevelen Mechanism.* 2020. **12**(4): p. 1007-1012.
19. Chen, Z., et al., *Grafted MXene/polymer electrolyte for high performance solid zinc batteries with enhanced shelf life at low/high temperatures.* 2021. **14**(6): p. 3492-3501.
20. You, Z., et al., *State-of-the-art recent progress in MXene-based photocatalysts: a comprehensive review.* 2021. **13**(21): p. 9463-9504.
21. Zhao, R., et al., *Self-assembled Ti 3 C 2 MXene and N-rich porous carbon hybrids as superior anodes for high-performance potassium-ion batteries.* 2020. **13**(1): p. 246-257.
22. Gao, Q., et al., *Tracking ion intercalation into layered Ti 3 C 2 MXene films across length scales.* 2020. **13**(8): p. 2549-2558.
23. Peng, Y.-Y., et al., *All-MXene (2D titanium carbide) solid-state microsupercapacitors for on-chip energy storage.* 2016. **9**(9): p. 2847-2854.
24. Zhao, D., et al., *Alkali-induced 3D crinkled porous Ti 3 C 2 MXene architectures coupled with NiCoP bimetallic phosphide nanoparticles as anodes for high-performance sodium-ion batteries.* 2019. **12**(8): p. 2422-2432.

Chapter 2

(LITERATURE REVIEW)

Introduction

CO_{oxid} is considered a hot research topic due to the high toxicity of CO with severe threats to the environment and human health. CO is a colorless, tasteless, and odorless poisonous gas, even in small traces. It's therefore important to purify the air and enclosed atmospheres from the CO by controlling the main sources either by using catalysts to prevent the formation CO as a byproduct or via catalytic oxidation of the produced CO directly to CO_2; or indirectly to valuable products. This requires designing new low-cost catalysts with high catalytic activity and durability.

Interestingly, CO can be involved in a wide range of catalytic reactions, such as mixing CO and hydrogen (syngas) and convert thermally to light olefins via (Fischer-Tropsch) synthesis [1-3]. Additionally, CO can be electrochemically oxidized to CO_2 for electric power production [4-6]. Likewise, it can be catalytically oxidized thermally or photo-oxidation to CO_2 [7, 8]. The electrochemical or photoelectrochemical of CO_2 produce fuels like formic acid, methanol, and methane in addition to electric power production [9-12]. Pt-based catalyst is a highly efficient catalyst but the high cost and the poisoning effect are the main problems [6, 13]. So the need for designing a new low-cost and efficient catalyst for CO_{oxid} is an important issue, where carbon-based materials are considered a good option to use as a catalyst for CO_{oxid} related to the unique catalytic properties as well as the low cost and earth-abundant. The research presented here focuses on designing new catalysts based on using MXene as the carbon-based catalyst for the first time in experimental CO_{oxid}.

Carbon monoxide sources

CO is released via several natural and anthropogenic sources. Naturally, methane oxidation that derived from the photochemical reactions in the soil, which is the main source of CO emissions in the environment [14]. Additionally, CO can be naturally released from the molten rocks of volcanos and also from the photochemical oxidation of the organic materials in wastewater and solid waste. It is estimated that 60% of the emitted CO come from anthropogenic sources and can be classified into three different categories [19]: wood burning, industry, and transportation which is the largest anthropogenic source of CO production. Figure (1) shows the contribution of different pollutants to CO emissions [19]. It can be seen that the CO released from transportation including on-road mobile sources and non-road mobile sources accounts for 71% of total CO emissions. Another report suggests that 90% of anthropogenic CO emissions come from the transportation sector [20]. The incomplete combustion that occurs inside the engine of the vehicle is responsible for the CO production; the mount of which depends on the engine efficiency. The amount of CO released from the engine is increased in cold climates, during the cold start of mobile and while vehicles are

moving at low speeds [20].

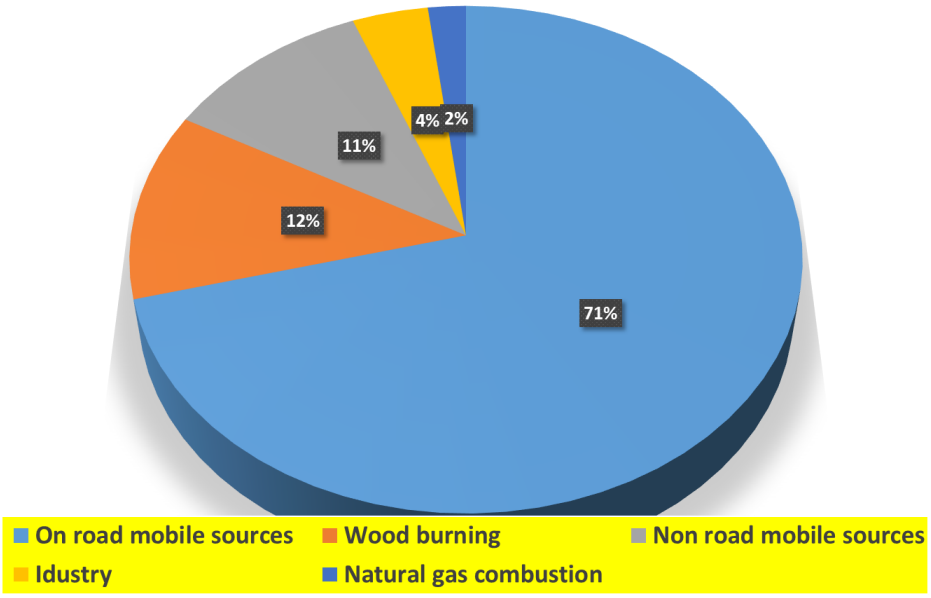


Figure 1: The anthropogenic sources of CO emissions. Data is obtained from ref.[19]

Effects of Carbon monoxide

CO is a highly toxic, flammable, colorless, tasteless, and odorless gas with a lower density than air. The effect of CO on human health, plants, and the surrounding environment is discussed in detail below.

Effects on the human health

All living organisms are affected by CO gas toxicity even at low concentrations in air. CO can cause headache or dizziness at concentrations lower than 50 ppm as seen in Figure 2 [14, 19]. At slightly higher concentratons (50-1200ppm), CO leads to more dangerous symptoms such as dyspnoea, loss of vision, and coma. At higher concentrations up to 1200 ppm, CO can lead to a serious health effects such as comma or seizures. At concentrations higher than 1900, exposure to CO can be lethal. This lethal effect is related to the faster interaction of the CO molecules with the hemoglobin of red blood cells at a rate (200 times) faster than the O_2-producing carboxyhemoglobin (CoHb) which disrupts the normal O_2 level in blood.

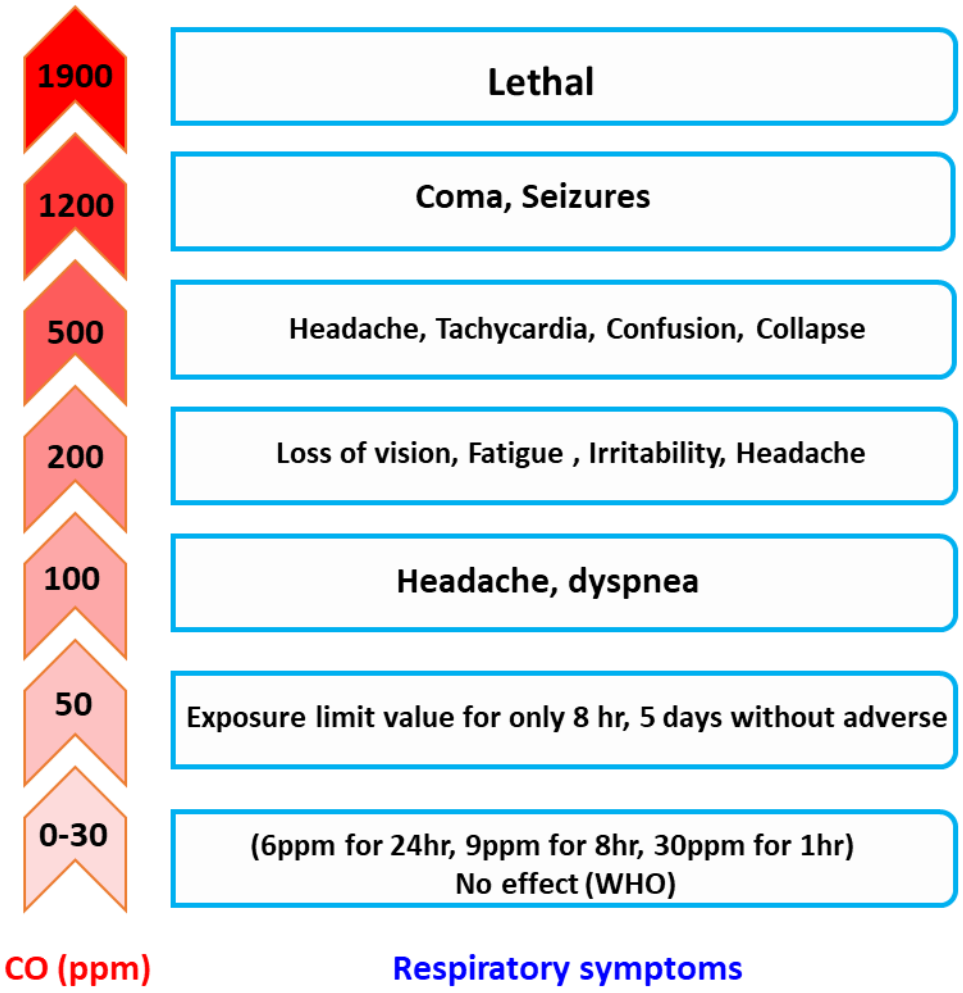


Fig 2. The effect of CO gas on human health.

Effects on the plant

Most plants have the ability to oxidize the CO to CO_2 and used it with water under sunlight to produce energy and oxygen which is known as the photosynthesis process. Although, continuous exposure to CO is harmful to the plant with time. CO can affect the nitrogen and protein that are responsible for the growth process and damage the germination system which leads to a negative effect on food quality.[14, 19] in addition to the ability to damage the cellular respiratory system of plants and reduce water adsorption.

Effects on the environment

The negative effect of CO also extends to the environment and is considered one of the green gas groups responsible for global warming. Indirectly, CO can increase the global warming potential of green gases at a higher level in the atmosphere and can increase the depletion of the ozone layer and global warming where CO has the ability to react with OH radicals decreasing its level in the atmosphere.[19] Moreover, the higher concentration of CO in the atmosphere leads to the form of toxic ozone (tropospheric greenhouse gas) which affects the respiratory system. The amount of CO in the atmosphere varies widely all over the

world and over the year.[19] Remarkably, there was a significant drop in CO level in the atmosphere after spreading the catalytic converters in vehicles all over the world which convert it to CO_2.

Carbon monoxide oxidation (reactions mechanisms)

There are two mechanisms commonly used for CO_{oxid}: Langmuir-Hinshelwood (LH) and Mars-van Krevelen (MvK)) mechanisms. In LH mechanism, both CO and O_2 gases are adsorbed (CO_{ads} and O_{ads}) while the metal oxide interface and the utilized support boost the catalytic activity of the oxides of the transition metal group as a promotor [14, 15]. The CO_{oxid} reaction happens over the catalyst surface via 3 steps as described in the following equations: -

$$CO\ (g) \rightarrow CO\ ads$$

$$O_2(g) \rightarrow 2O\ ads$$

$$CO\ ads + O\ ads \rightarrow CO_2(g)$$

In the case of MvK mechanism, the CO and O_2 reactants molecules are adsorbed on the surface of the catalyst. This is followed by the O2 splitting into two oxygen atoms and having the ability to spread over the whole metal surface to combine with CO to give CO_2 [14, 16]. Lastly, the formed CO_2 is desorbed leaving the catalyst surface into the gas phase. The rate of CO reaction is controlled by the adsorption of CO and O_2 dissociation, which in general happen at higher temperatures. The CO molecules in the gas phase are directly oxidized to CO_2 in presence of O species but the reaction rate of CO_2 formation is directly proportional to the catalyst surface coverage with O_{ads} and CO_{ads} as described in the following equations: -

$$O_2 + 2* \rightarrow 2O\ ads$$

$$CO\ ads + O\ ads \rightarrow CO_2 + 2*$$

$$CO + * \rightarrow CO\ ads$$

In the oxidation step, the oxygen of the metal oxide surface is responsible for the oxidation of CO which leaves oxygen vacancies behind that reduce the oxidation state of metal ions to a lower value. The metal ions get oxidized again by consuming the available oxygen gas phase.

Another mechanism knows as Eley-Rideal (ER) mechanism suggests that the CO and adsorbed O_2 reactants directly reacted to form CO_2 [17, 18].

$$CO\ (g) + O_2\ ads \rightarrow CO_2 + O\ ads$$

Carbon monoxide oxidation methods

CO can be catalytically converted into CO_2 gas by thermal, photocatalytic, electrochemical or

photo-electrochemical means. In thermal catalytic CO conversion, CO gas reacts with O2 at a higher temperature and catalysts are used to decrease the required temperature to save energy. In the case of the photocatalytic CO conversion, CO converts to CO_2 by using photo catalysts where the catalyst surface splits O_2 into two Oxygen atoms with light photons' assistance and then combined with CO to form CO_2. In the case of the electrochemical CO conversion, the oxidation reaction can occur in different electrolytes over a wide range of pH under applied potential. The methods are described below in detail with examples.

Thermal CO oxidation

In the thermal CO_{oxid} method CO gas reacts with O_2 gas in the presence of an assistance heat source and the CO conversion proportional to the reaction temperature and is function of gas flow rate, catalyst type and loading amount. To satisfy the standers of fuel efficiency with low emission of toxic gases, especially CO. In addition, complete CO conversion to CO_2 at a low temperature lower than 100°C. Many efforts have been made to design different catalysts for CO_{oxid} at low temperatures (T_{100}) as revealed in table (1) [21-25]. Nobel metals like (Pt, Pd, Au, and Ag) as mono, binary, and ternary metals-based catalysts, and their mixtures are most commonly used for thermal CO_{oxid} due to their high catalytic properties and work at lower temperatures even it can work atRTor 0^{o}C. [62]. Where Au-based catalyst is the best for thermal CO_{oxid} even can work atRTand (Pt, Pd) have good thermally catalytic conversion but not lower than 100^{o}C. But the rarity in nature, high cost, and also the poisoning effect of CO barred to use of it directly in catalytic CO converters. So is reinforced by using different supporters like metal oxides, and carbon materials which can rise the catalytic activity and stability besides to be cost-effective to be applicable. For example, in figure (3a-c) the CO_{oxid} activity for porous gC_3N_4 nanotubes doped with Pd and Cu (Pd/Cu/gC_3N_4NTs) was superior complete conversion temperature (T_{100}) 154 °C related to the synergatic effect throug the combination between Pd and Cu and the outstanding catalytic propertirs of gC_3N_4 as suborter [10]. Pd-impeded 3D porous graphene with nanohole structrue has a complete conversion temperature (T100) at 190°C[26]. The binary metals AuPd NPs decorated TiO_2 catalyst gave a full CO conversion at (T_{100}) 190 °C [27]. Fan et al. have synthesized Pt/CeO_2 nanorodes with a complete

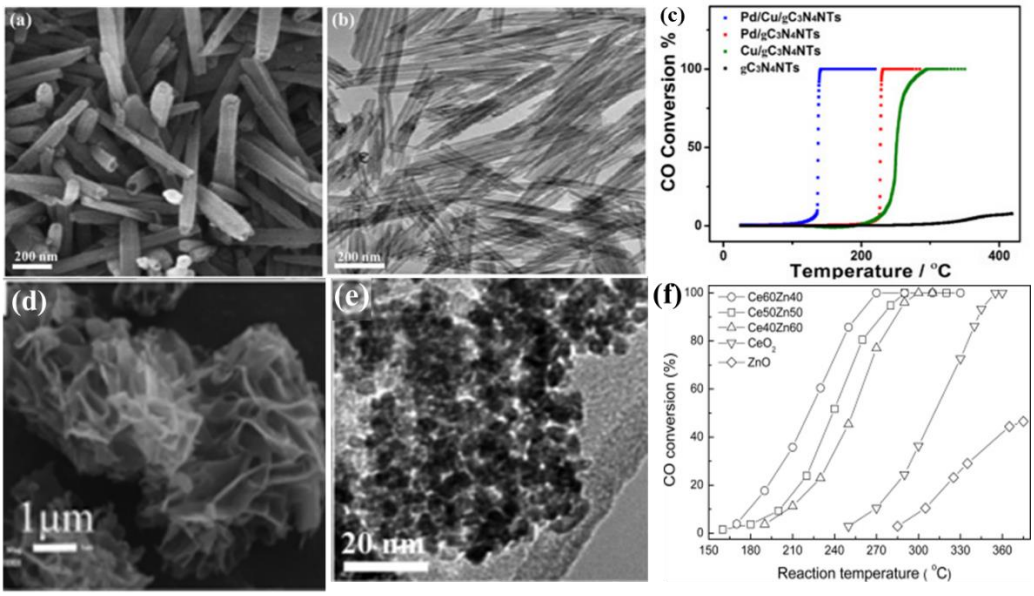


Fig.3 (a) SEM image and (b) TEM image of Pd/Cu/gC_3N_4NTs and (c) CO conversion efficiency as a function of temperature. copyright permission Elsevier [10] (d) SEM image, and (e) TEM of the as-prepared CeO_2-ZnO. (c) the XRD, and (f) Thermal CO_{oxid} for the prepared catalysts. Copyright permesiion elsevir [28].

CO converted to CO_2 at 80 °C when Ce-BTC was used, where the MOF-derived CeO_2 is superior to synthesis CeO_2 [29]. Transition metal oxides or mixed are greatly active towards the thermal CO_{oxid} like (Fe_2O_3, CeO_2, MnO_2, NiO, Co_3O_4, CuO, Cr_2O_3, etc). low price high performance and different preparation methods with high yield make it easily applicable commercially. The cobalt-based catalysts are highly active catalysts in CO conversion and have an outstanding thermal resistance.[30, 31] Fig (3d-f) showed a mixed oxide of hierarchically CeO_2-ZnO nanostructure with higher surface area (100 m^2/g), which was used for thermal CO_{oxid} [28]. The meso-/macroporous structure contains wurtzite ZnO and cubic CeO_2 phases confirmed by the XRD. The hierarchical structure was found to be a significant way to increase the CO_{oxid} activity. The CO_{oxid} activity for $Ce_{60}Zn_{40}$ is better compared to the other prepared catalysts with complete CO conversation at 250°C [28]. Additionally, combination the merties catalytic properties of oxides and outstanding physicochemical advantages of carbon materials is good in CO conversion. For example, figure 4 shows Cu_2O/g-C_3N_4 with amass ratio 4:10 showed a good catalytic conversation at (T_{100}) ~200 °C due to the synergetic effects act between the 2D lamellar g-C_3N_4 and Cu_2O besides the stable shape and structure [32].

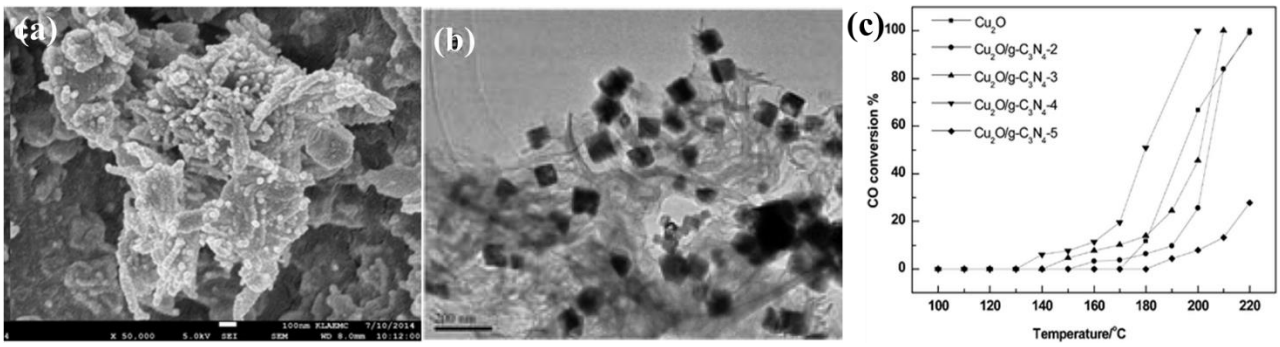


Fig.4 (a) SEM image Cu2O/g-C3N4-4 (b) TEM and (c) Catalytic effeciency of Cu_2O and Cu2O/g-C3N4 with different mass ratios. Copyright permission RSC [32].

Furthermore, there are different materials like chalcogenides (MoS, CuS, and FeS) and perovskites which have the potential for CO conversion [33-35]. A theoretical study investigated that Al-doped MOS_2 is a promised single atom catalyst in CO_{oxid} [35]. Macroporous structure $La_{0.8}Sr_{0.2}CoO_3$ perovskites with oxygen vacancy-rich have a superior activity in CO_{oxid} with a complete CO conversion lower than 200°C.[36]

Table 1. The CO_{oxid} performance for different catalysts and (T100) the temperature required for complete CO_{oxid} to CO_2.

Catalyst	**T_{100} (°C)**	**Ref.**
Au/Pd/gC_3N_4NFs	144	[24]
Pd/Cu/gC_3N_4NTs	154	[10]
Pd-impeded nanohole structured 3D porous graphene	190	[26]
AuPd/TiO_2	190	[27]
Pt/CeO_2	80	[29]
Cu_2O/C_3N_4	200	[32]
AuPd/SiO_2	182	[37]
AuPd@Al_2O_3	200	[38]
Pd/La-doped γ-alumina	175	[25]
MnO_x	310	[22]
Cu_1/Mn_1	180	[21]
Co_3O_4/mesoporous g-C_3N_4	160	[23]

Photocatalytic CO oxidation

Herein, the Photocatalytic $_{COoxid}$ method uses photocatalysts which work depending on the e^- and h^+ that are generated by photo power assist as redox reactants. Where the CO_{oxid} rate depends on generated photocurrent velocity [39, 40]. Nobel metals are known as the best catalysts with superior the photo-induced electron transfer rate when added to photocatalytic active materials like TiO_2, CeO_2, and

carbon materials [40]. Furthermore, the superior photocurrent means more charge transfer which accelerates the chemisorption dissociation of O_2 on the catalyst surface. TiO_2 is known as one of the most photocatalytic activities. For instance, fig 5 shows Pt/TiO_2 catalyst that is treated under air (673 K) has superior photocatalytic CO_{oxid} compared to only the treated under N_2 and increases with increasing the Pt content which increases the kinetic reaction and also proved by measuring the photoelectrochemical current [41].

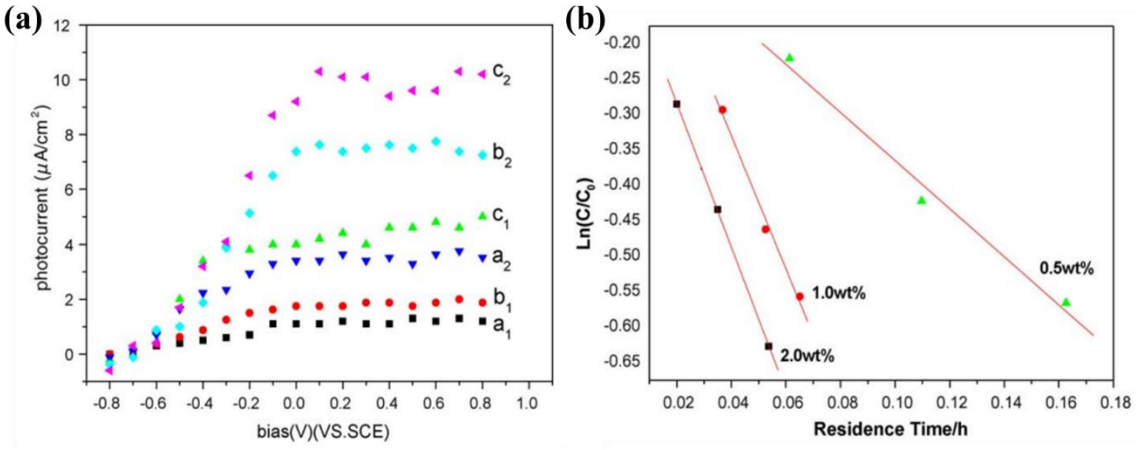


Fig 5 (a) Photocurrent–voltage relations of Pt/TiO_2 catalysts: a1, b1, c1 denote Pt content 0.5, 1, 2 wt.% stabilized under N_2 respectively. a2, b2, c2 denote Pt content 0.5, 1, 2 wt.% annealed in air respectively. (b) Pt/TiO2 was annealed at 423 K for 2 h under N_2 and then annealed at 673 K under air for 2 h, copyright permission from Elsevier [41].

The RP-AH (p-type) catalyst shows a superb photocatalytic activity compared to RP, RP-A, and RP-H ($Ru/TiO_2/Pt$) in CO_{oxid} for 1000 ppm CO under UV irradiation and completely oxidized after 2hr. the higher hole mobility assets of RP-AH benefit the holes reactivity in converting CO into CO_2 with O− [42]. The RP-AH has a stable reactivity after 4 cycles of 100% that is related to the synergetic and the alloying effect of both Pt and Ru metals as well as combined with TiO_2 figure 6.

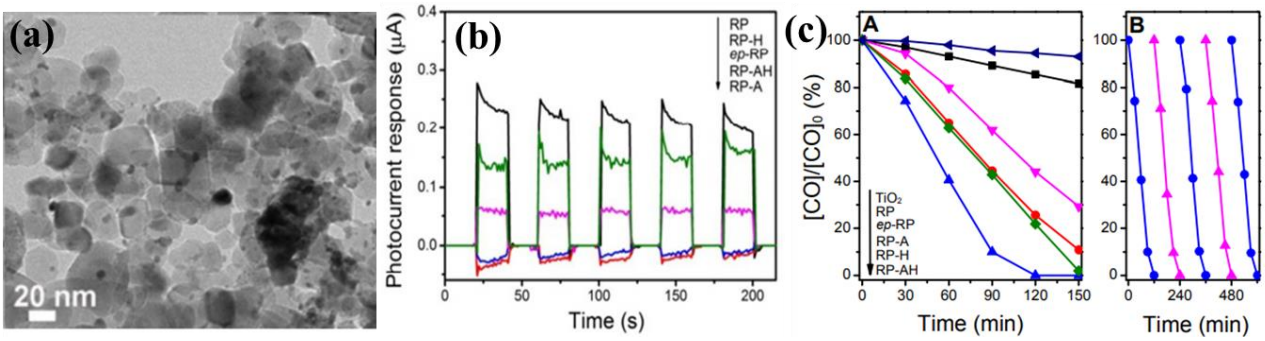


Fig 6 (a) TEM of RP-AH, (b) Transient photocurrent response of prepared catalysts at a bias of10 mV vs SCE under UV irradiation, (c) A- Photocatalytic CO_{oxid} for the prepared catalyst, B- The stabilty recycling test of RP-AH. Copyright permission ACS 2016 [42].

In contrast, the electrochemical CO_{oxid} can be enhanced when the catalyst is exposed to a light source like $PtPd/gC_3N_4$ nanorods was found to be 1.48 fold current density higher than in dark in KOH electrolyte

related to the unique photocatalytic properties of gC_3N_4 fig(8d) [6].

Electrochemical CO oxidation

The electrochemical CO_{oxid} conversion is greatly important to convert the dissolved CO in different electrolytes to CO_2 under applied voltage between the WE loaded with the catalyst and the counter. The technique can be also used to convert CO indirectly to valuable fuels, in addition, to examining the catalyst's surface stability towards CO poisoning through the electrochemical CO stripping measurements that affect the catalytic activity in different electrochemical reactions like MOR. [43-47]. This method converts the dissolved CO in electrolytes to CO_2 under applied potential in a wide PH range (table 2). Nobel metals have superior activity in CO_{oxid} related to their outstanding catalytic properties [48, 49]. For instance, The electrochemical CO_{oxid} for Pt dendrimer-encapsulated nanoparticles provided a current density of 0.2 $mAcm^{-2}$ in 1M $HClO_4$ and a sweep rate of 50 mV/s vs reference electrode (Hg/Hg_2SO_4) at 0.3 V [49]. The Pt/SnOx catalysts shows a good CO_{oxid} current density of about 0.87 $mAcm^{-2}$ with a lower onset potential of 0.7 V compared to commercial Pt/C Pt/SnO_x with a sweeping rate of 20 mV s^{-1} in 1 M $HClO_4$ vs RHE [50]. Binary PtNi multi cubes with particle sizes of about 40nm were conducted with the CO stripping after adsorption of CO electrochemically in 1M KOH at 0.1V for 900s followed by flushing in N_2 gas (Fig 7a-b). The CVs display a higher current density of (0.58 mA cm^{-2}) at 0.65 V at a rate of 50 mV s^{-1} compared to commercial Pt/C. This shows the multi-cubic structure of PtNi has a superior activity for CO_{oxid} [48]. Fig 7c shows a ternary porous nanodendrites PtPdRu (NDs) with highly porosity degree which displays a superior anti CO-poisoning compared with PtPdRu nanoflowers, PtPd NDs, and commercial catalyst (Pt/C) fig 7d [34].

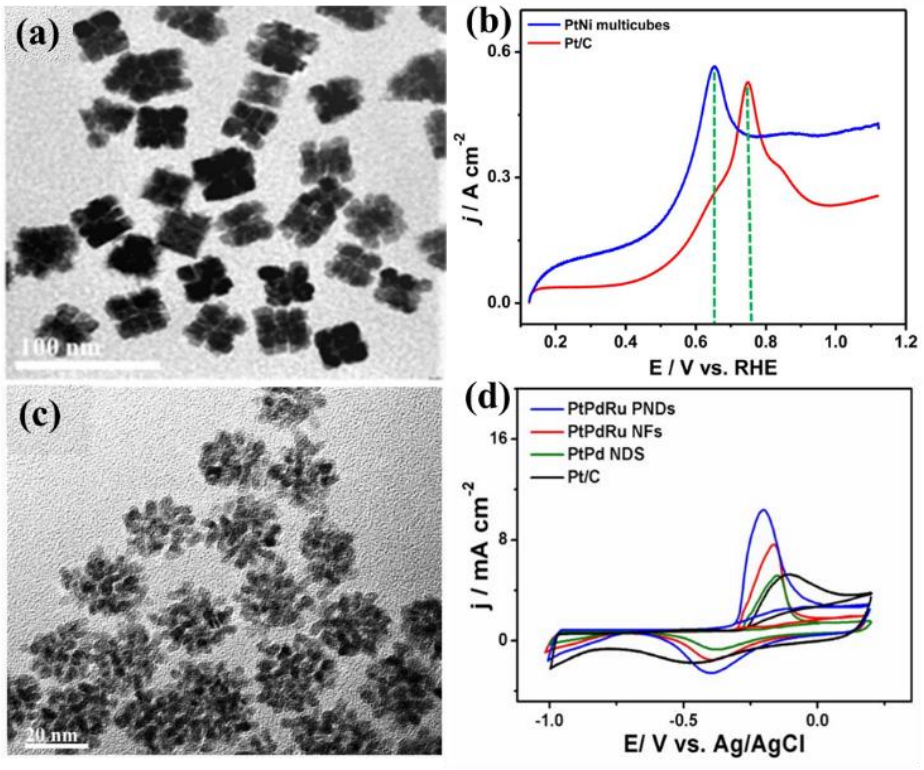


Fig.7 (a) TEM image of multicubic PtNi, and (b) CO-stripping in (1 M) KOH electrolyte at a scan rate of 50 mVs^{-1}, Copyright permission RSC [48]. (c) TEM image of PtPdRu NDs, and (d) CO-stripping CV of different catalysts measured in 1 M NaOH CO-saturated at rate of 50 mVs^{-1} and Copyright permission RSC [51].

The CO stripping for PtRu/C gave a higher current density in 0.1 M H_2SO_4 at a scan rate of 20 mV/s of 5 mA cm^{-2} versus the WE RHE at 0.6 V [52]. In another study, the CO_{oxid} activity for PtPd/gC_3N_4 nanorods with 1.5 wt.% metals was greater than commercial Pt/C in KOH electrolyte [6]. Which gave a higher current density of 14.75 mA/cm^2 at a lower voltage for PtPd/gC_3N_4 nanorods 2 times more than Pt/C as shown in fig (8a-c). This is owing to the superior electrochemical surface area for the prepared nanorods 75 m^2 /g in addition to the synergetic effect electronic of PtPd together. As shown below, the integration between the unique catalytic properties of noble metals and the physicochemical merits of carbon-based materials gave a good activity and stability with low cost and high production yield.

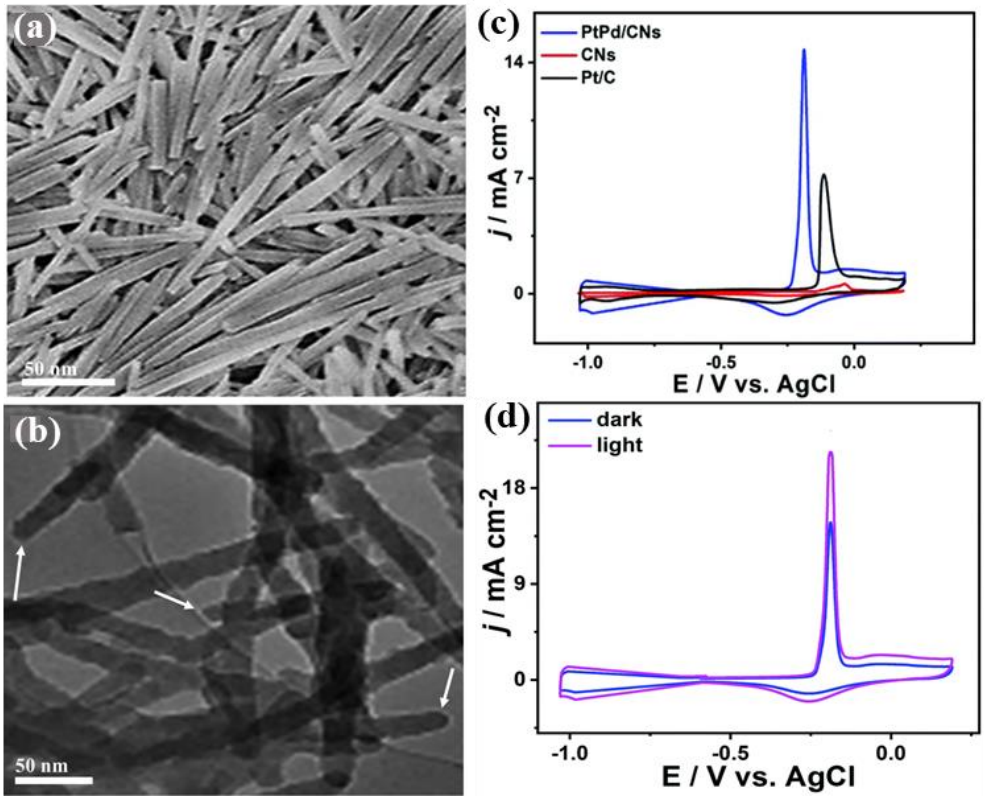


Fig.8 (a) SEM images, (b) TEM image of PtPd/gC_3N_4 nanorods. CVs in a CO-saturated aqueous solution of 0.1 M KOH at rate of 50 mVs^{-1} (c) in dark, and (d) under the light. Copyright permission RSC [6].

Table 2. The electrochemical CO oxidation performance for different catalysts in different mediums.

Catalyst	**Medium / Scan rate / reference electrode**	**Maximum Current (mA/cm^{-2}) /**	**Ref**

		Voltage (V)	
60 wt % Pt/C	0.5 H_2SO_4 10 mVs^{-1} SHE	0.2 & 0.64	[43]
Well-ordered Pt(111)	0.1 M NaOH 50 mV/s RHE	0.5 & 0.8	[44]
PtNi multicubes	1 M KOH 50 mV/s RHE	0.58 & 0.65	[48]
PtPd Nanodendrites	1 M KOH 50 mV/s Ag/AgCl	5.1 & -0.15	[51]
Pt dendrimer-encapsulated nanoparticles	0.1m $HClO_4$ 50 mV/s Hg/Hg_2SO_4	0.2 & 0.3	[49]
Pt(110)–Ru	0.5 M H_2SO_4 100 mV/s RHE	0.025 & 0.5	[45]
Pt/SnO_x	1 M $HClO_4$ 20 mV s^{-1} RHE	0.87 & 0.7	[50]
Pt-NbOx	0.5 M H_2SO_4 20 mV/s RHE	0.5 & 0.75	[46]
Pt(FAM)	0.1 M H_2SO_4 50 mV/s RHE	0.32 & 0.72	[47]
PtRu/C	0.1 M H_2SO_4 20 mV/s RHE	5 & 0.6	[52]

Parameters effect on the CO oxidation activity

CO conversion activity and durability to CO_2 for catalysts may be influenced by various parameters like the catalyst type and its composition as (Nobel metals, transition metals oxides, carbon materials,

halloysite, and chalcogenides), morphology (shape structure, size, and surface area), preparation methods, supporter type and loading amount in addition to the CO conversion method and the parameters of the pretreatment [53]. These parameters can predict and determines the catalytic activity, catalyst stability, and durability towards CO_{oxid}. Noble metals are among the most active catalysts towards CO_{oxid}, ascribed to the outstanding catalytic activity and electronic behavior [44]. Moreover, noble metals give a superior current density in electrochemical CO_{oxid} and can significantly promote the photocatalytic CO conversion [51]. However, the high cost, rarity, and CO poisoning hinder makes them non-ideal candidates. Various efforts were dedicated to developing low-cost, efficient catalysts for CO_{oxid} and preventing CO poisoning in fuel cells and came to fruition in tailoring. Transition metals, carbon materials, and other developed materials show a good catalytic activity toward CO_{oxid}, and the activity is enhanced when combined with Nobel metals due to their unique catalytic properties. In addition to the parameters mentioned above, other parameters can improve the catalytic activity as well as the stability. For instance, The preparation method can affect the CO_{oxid} efficiency, Santos et al. found the metallic dispersion of different noble metals (Pd, Rh, Pt, Au, and Ir) over TiO_2 as a support affected by the synthesis method, for instance, the Pd NPs synthesized by incipient wetness impregnation (IMP) was 8 nm and by liquid-phase reduction deposition (LPRD) was 3nm with higher dispersion, as shown in fig 9a using LPRD method is preferred to prepare the catalyst that gave a complete CO conversation at a lower temperature compared with the applied IMP method [54]. Binary metals AuPd NPs decorated TiO_2 catalyst gave a complete CO conversion at (T_{100}) 190 °C when thermally treated in reducing (H_2), but gave a lower (T_{100}) 240 °C if treated under O_2 (oxidizing). This is related to morphological changes [27]. Also, the surface area and the pore size for AuPd@Al_2O_3 have been affected by the calcination temperature which increased by increasing the temperature where the catalyst calcined at 473K gave the highest activity with complete CO conversion at 423K [38]. The solvent type that used in the preparation of catalysts

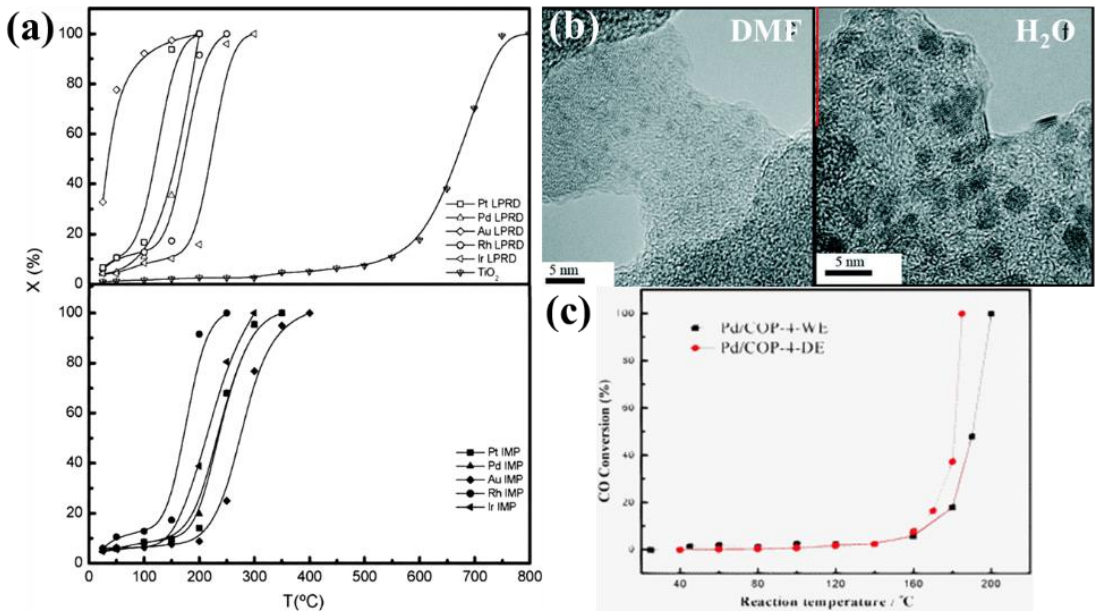


Fig. 9 (a) CO_{oxid} conversation versus temperature over supported noble metal. Copyright permission 2010,

Elsevier [54]. (b)TEM of the prepared Pd/COP-4 in DMF and water, and (C)the CO_{oxid} of Pd/COP-4 prepared by different solvents Copyright permission 2013, RSC [55].

can affect its catalytic activity towards the CO_{oxid}. For example, when the water was used as a solvent for the preparation of Pd/COP-4, the Pd size outside pores of COP-4 was found about 2.4 nm, and in the case using the DMF as solvent was found 1.1 nm inside the pores due to the DMF contains Pd ions can easily enter the pores as well as reduced inside the pores while water cannot [55]. The CO_{oxid} activity for Pd/COP-4 prepared by the DMF solvent displays an excellent CO_{oxid} activity compared with the water fig 9b-c. The shape and size can enhance the catalytic CO_{oxid} activity by increas the active surface area. where, The CO conversion for Ru nanoworms decorated TiO_2 gave a complete CO conversion at a lower temperature (150 °C) compared with using Ru nanoparticles, which attributed to the unique structure of 1-D with a low diameter of 1.6 nm and 13.6 nm in length also the high dispersity and high active surface area. The catalyst morphology has an effect on the catalytic activity, the wormlike shape of Ru NWs on TiO_2 supporters was found to have a complete CO conversion lower than using Ru NPs by 50 ^oC [56]. Due to the catalytic properties of shape and sub-nanosize effect rushes the kinetic reaction. The CO_{oxid} activity for $AuPd/SiO_2$ was found to depend on the preparation method, Au: Pd weight ratio in catalyst, and also the ratio effect on the PdAu particle size. The alloying prevents oxidation compared to the monometallic Pd which negatively affects the activity [37]. The addition of additives can affect the catalytic activity, Tanikawa et al, this group prepared two different heterogeneous mixtures (Pd/Ba/Al) and (Pd/Ba/CZ) and investigated the outcome of Ba loading on the CO_{oxid} activity. They found the increase of Ba loading in Pd/Ba/Al catalyst, the CO_{oxid} activity enhanced. Contrary to for Pd/Ba/CZ, the activity decreased. They suggested that the increase of Ba when combined with CZ supporter it avoided the direct contact between CZ and Pd so the supply rate of oxygen from CZ to Pd will decrease and the CO_{oxid} rate will reduce [57]. Pt-based catalysts like $Pt/CeO_2/I3\text{-}Al2O_3$, and Pt/CeO_2 have a great activity toward the CO_{oxid} conversation [58, 59]. Surprisingly, the electrochemical CO_{oxid} for the prepared one-dimensional doped graphitic carbon nitride (1-D PtPd/gCNs) shows a superior catalytic activity and gave current density of 14.75 mA/cm^2 at a lower voltage -0.19V in aqueous 0.1 M KOH that is two times lower than the commercial (Pt/C), that's due to the integration between the catalytic and synergetic properties of co-atomic doping of Pt and Pd with the outstanding physicochemical properties of 1-D g-CNs [6]. As well as, when comparing the electrochemical method with the photoelectrochemical method, the current density for the CO_{oxid} increased 1.4 times photo electrochemically with UV-vis light compared to in the dark. lower complete conversion temperature (T100) with fast CO_{oxid} kinetics was observed when binary Pd and Cu doped gC_3N_4NTs (154 °C) figure (3a-c) [10]. When compared with Pd doped gC_3N_4NTs and Cu doped gC_3N_4NTs 210 °C and 250 °C respectively fig (x), because of the combination between electronic and synergetic effect of Pd and Cu besides to the physicochemical properties of 1-D poures gC_3N_4. Interstingely the of catalytic activity of $Pd/Cu/gC_3N_4NTs$ was significantly greater compered to Pd-impeded 3D porous graphene with nanohole structrue complete conversion temperature (T_{100}) at 190°C [26]. This shows the designed shape and size (1D,2D, or 3D), physicochemical properties of suporter, and the loding amount with the type of metals as dopent or NPs

are the mainely effect on the CO_{oxid} activity.

Carbon-based materials

The type of catalysts and their composition plays a vital role in the CO_{oxid} activity according to their own physicochemical properties. There are need to design new low-cost catalysts, high yield, good catalytic activity, stability, and also stability toward CO poisoning. Carbon-based materials like (graphene, carbon dot, carbon nanotube, carbon nitride, fullerenes, Metal-organic frameworks (MOF), and MXene) are one of the most promising catalysis for CO_{oxid} related to their superior catalytic activity in different catalytic reactions owing to their physicochemical properties like high electrical conductivity and surface area, corrosion resistance, surface functionalities, tunable porosity, thermal and chemical stability [26]. In addition to easy preparation with a high yield from various synthetic or natural abundant materials, low price, and friendly to the environment. As described above some examples of carbon-based materials showed good catalytic activity and also stability toward the CO_{oxid} reactions.

Novel carbon-based catalyst (MXenes)

Herein, among carbon-based materials, this work focuses on using 2D-MXenes nanomaterials as a support for mono and binary Pd and Pt nanoparticles for the electrochemical CO_{oxid} due to the sample preparation of MXene with high yield, low cost, earth-abundant, and its significant physicochemical properties of high active surface area, high electron mobility/density, abundant catalytic active sites, surface hydrophilicity with rich functional groups, outstanding mechanical strength, and good thermal and electrical conductivity. But it's rarely reported only theoretically for CO_{oxid}. For instance, cheng et al. found the Mo_2CO_2 MXene act as a superior supporter of the single atomic catalyst (SACs) (fig 10), where The CO_{oxid} activity for Pd as SAC occupied the defective sites of Mo_2CO_2 monolayer and oxygen vacancy was better than the Pd(111) according to the TER mechanism with low energy [60].

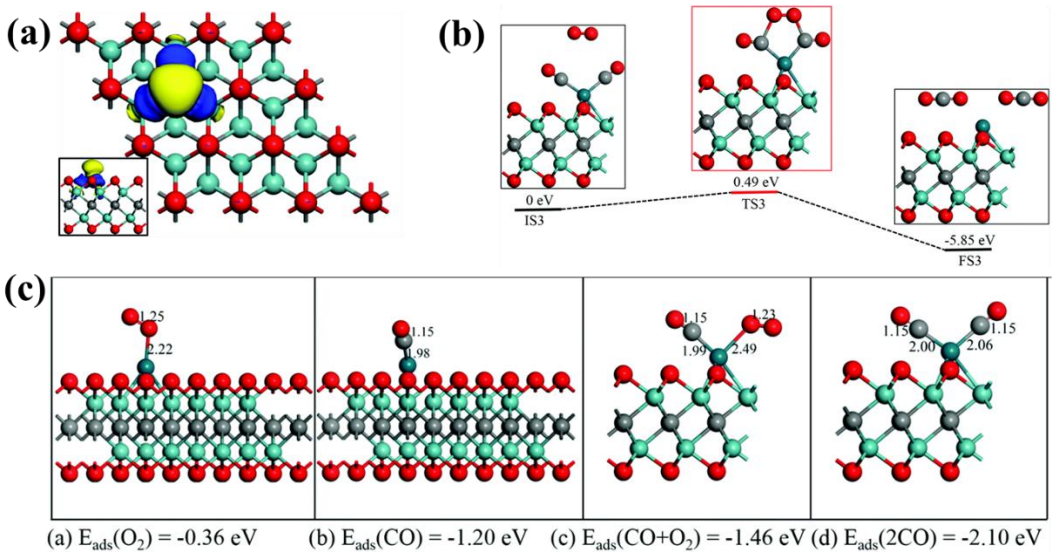


Fig. 10 (a) Top and side views of the charge density difference of Pd/OV–Mo_2CO_2 (b) Reaction mechanism of CO_{oxid} via TER-mechanism, and (c) Adsorption configurations and adsorption energies. copyright permission RSC [60].

Fig 11 showed that Mo_2CO_2 supported by the Cu3 clusters gave a good catalytic CO_{oxid} activity and good stability [61]. Where, the Cu3 cluster operated as a reservoir of the electrons to control the gained or loosed electrons to promote the CO_{oxid} reaction and found the rate-limiting energy barrier 0.72 eV lower than Pt and Pd [62, 63] which showed a high catalytic CO_{oxid} activity.

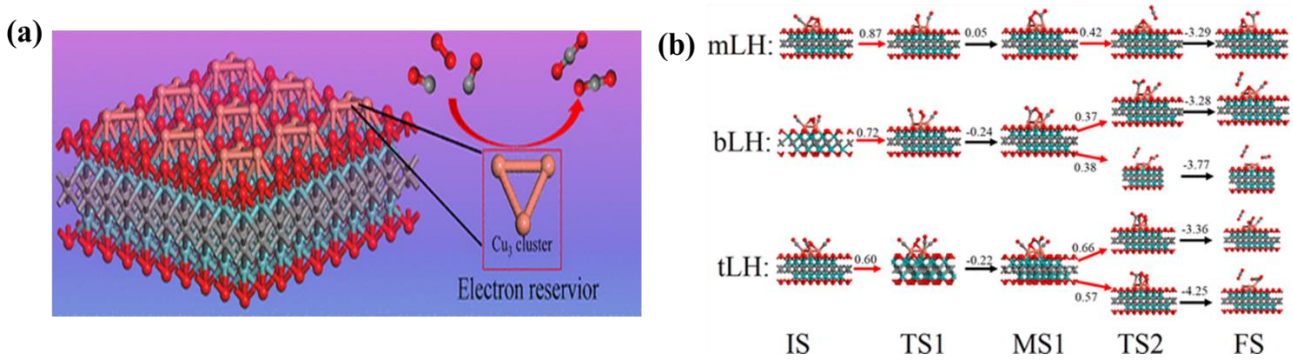


Fig. 11 (a) The diagram for Cu3 active site of Cu_3/d-Mo_2CO_2 works as an electron reservoir to

facilitate the CO_{oxid} conversation rate. (b) CO_{oxid} pathways reactions (side views) over Cu_3/d-Mo_2CO_2 by diffrent mechanisms. Copyright 2018, American Chemical Society [61].

In another study, Zn-doped $Mo_2CO_2^{-\delta}$ [64] was found a promising catalyst for CO_{oxid} compared to other different catalysts via the ER mechanism with barrier energy of 0.15 eV that is lower than Pt and Pd catalysts (1.05 and 0.93 eV) [62, 63]. Furthermore, the Ag monolayer supported on Mo_2C MXene exhibited excellent CO poisoning resistance [65], and also the Ti anchored Ti_2CO_2 MXene [66] own a good catalytic activity towards the CO_{oxid} theoretically. So, combining the outstanding catalytic properties of Pt and Pd and the superior physicochemical properties of MXene was superior for the electrochemical CO_{oxid} experimental reactions in a wide pH range.

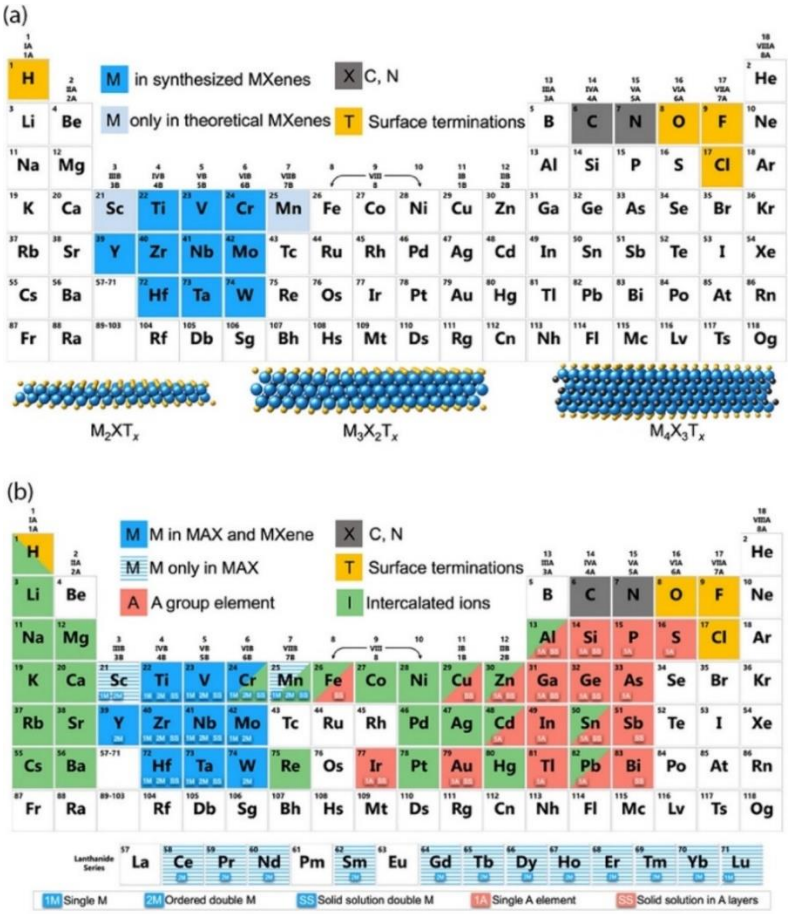


Fig. 12 Periodic tables showing compositions of MXenes and MAX phases. (a) Elements of MXenes chemical structure. (b) Elements of different MAX phases, Copyright 2019 American Chemical Society [67].

History and structure

MXenes belong to 2D transition carbonitrides, metal carbides, and nitrides which discovered at Drexel University by researchers (Yury Gogotsi and Michel Barsoum) in 2011 [68]. More than 30 MXene structures successively prepared since 2011 after selectively etching MAX phases with some different chemical compositions as shown in (Fig 12a). The formula of MXenes is $M_{n+1}X_nT_X$, where n = 1, 2, or 3, demonstrating three common structures. M means a transition metal, for instance, V, Ti, and Mo, X refers to C/N, while T_X represents various surface functionalization by F^-, OH^-, and/or oxygen O^{-2} as shown in fig (12b).

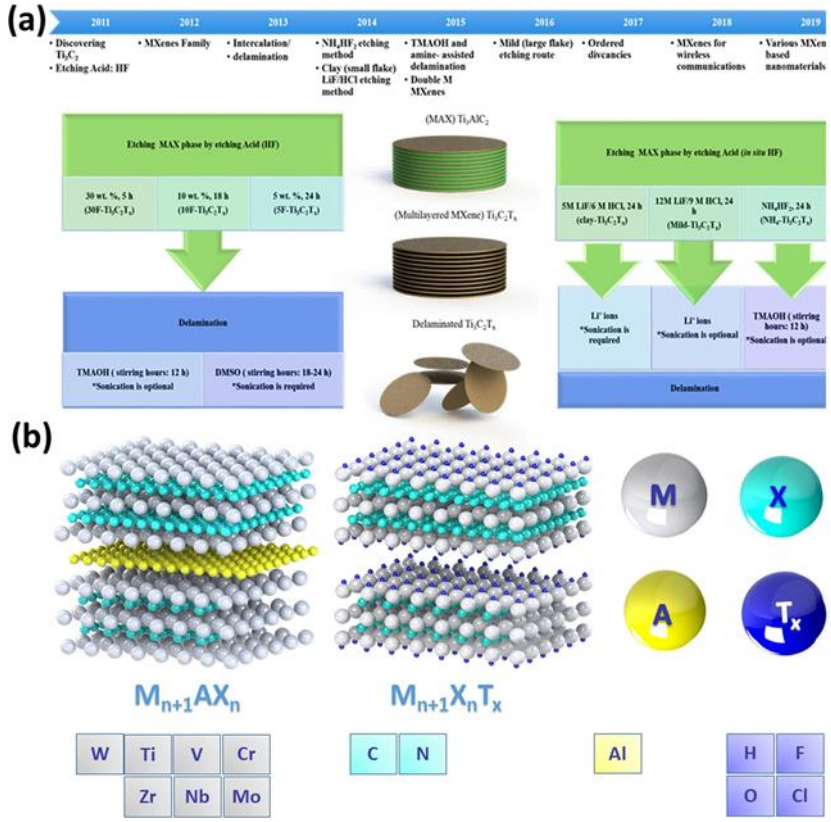


Fig. 13 (a) the chemical structure for MAX and MXene phase (b) Schematic illustration of the development path of MXenes synthesis. Copyright 2022 Elsevier [69].

preparation methods of MXenes

The development path of MXenes synthesis and its chemical structures until now shows in fig 13 [69], where there are two mainly preparation methods called direct and indirect HF etching via using a mixture of ($LiF+HCl+NH_2HF_2$) [70]. in the direct method, MXene was delaminated only to 2D layers by sonication. while in the indirect method, sonication is only required at low concertation of a mixture of (HCl/Lif and NH_4HF_2) [71]. There are other etching methods to overcome the hazardous effect of HF like LiF/HCl, NH_4HF_2, mechanical,

hydrothermal, molten, salt templating, and gas process etching methods [72-76].

Direct HF method

The HF etching method is the most popular synthesis method for 2D MXenes. The first experimental preparation was reported by Naguib et al. The process includes etching of the MAX phase (Ti_3AlC_2) in 50% pure HF for 2hr at RT [77]. At first, Al is etched by HF under sonication giving parallel Ti-C layers that are neighboring. (H_2O, urea, DMSO, TBAOH, hydrazine, and isopropyl amine) are used to add ions by intercalation with a large radius ($^-$OH and H_2O) into the framework of Ti-C mechanically or chemically through formation bonds of hydrogen, and thereafter enlarges the spacing between Ti_3AlC_2 layers by sonication assisting. HF has high etching power which etches all Al layers and also etch some neighboring Ti and C atoms causing single vacancies which able to reduce and accommodate positions for several metal ions [78, 79].

This method depends on the HF concentration and the time of etching, so numerous of MXenes like Mo_2CT_x, $Nb_{4/3}CT_x$, $W_{4/3}CT_x$, V_2CT_x, $Hf_3C_2T_x$, Ti_2NT_x, $V_4C_3T_x$, $Mo_2TiC_2T_x$, Nb_2CT_x, $Zr_3C_2T_x$, $Mo_{4/3}CT_x$, Ti_2CT_x, V_2CT_x, $Ti_3C_2T_x$, and $Nb_4C_3T_x$ were prepared using concentrations of 1, 5, 10, 35, 48, and 50 % [80-82]. The required time for etching ranged from 2 h to 165 h, related to the concentration of HF. The etching time is directly proportional to the HF concentration. 50 % HF is commonly used to allow etching of Al completely with uniformed 2D MXenes sheets. MXenes layers conserve the hexagonal close packing (hcp) like MAX phase structure after etching but with increased d-spacing lattice and decreasing the basal planes [80].

Indirect HF etching

This method is used to prevent using hazardous HF etching solutions for the synthesis of MXenes by using moderate and eco-friendly etchings such as NH_4HF_2 or acids like HCl and H_2SO_4 mixed with metals or its fluorides as LiF, FeF_3, NaF, CaF_2 KF, and CsF [83]. This permits the successive etching of A elements in conjunction with the interaction of cations (NH^{4+} and Li^+) with H_2O into the formed 2D sheets surface of MXenes to form highly exfoliated MXene with a higher interlayer spacing, higher oxygen content, larger defects, great electronegativity of fluorine, more attached hydroxyl, and higher stability than direct etched MXenes[84, 85]. Also, this method is controlled by time of etching and etchant concertation as the main effecting factors. The etching solution contains 6–12 M of HCl and

0.6–5 g of LiF formed different MXenes like Mo_2CT_x, $Cr_2TiC_2T_x$, $Ti_3C_2T_x$, V_2CT_x, and Ti_3CNT_x. for complete etching of (A) element of MAX phase via using LiF/HCl needs 12-384hr, 1M NH_4HF_2 needs only 12 hr to form $Ti_3C_2T_x$ [86].

both direct and indirect HF etching procedures, the sonication procedure such as water-bath and probe sonicating can govern the MXene interlayer spacing and sheets/flake sizes. Due to the higher irradiation power of the probe sonicator, it forms a more smaller sheets/flake size during the delamination of MXene than sonication in water-bath [53] as the probe sonicator carries the ultrasonic waves straight through the circular cross-section of the sonicator tip to MXene, as mentioned in detail in the review [87]. To prevent the formed active MXene from oxidation, it is protected by an inert environment like Ar or N_2 gas in an ice bath during the sonication process.

The preferred method used in this study

In this study, the direct etching method was employed via HF etching solution followed by the delamination process and the intercalation occurred under sonication using organic dimethyl sulfoxide (DMSO) solvent in an ice bath under continuous N_2 flow. This method is used due to: -

- Simple process with a high yield of 2D-MXene.
- High yield and low cost using abundant materials.
- Uniform 2D-MXene sheets formed and stably dispersed as large DMSO molecules inserted between flaks and also as dispersants at the same time.
- High HF concentration gave preferred 2D-MXene morphology with abundant defects and surface functionalities to synthesize different catalysts such as $Pt/Ti_3C_2T_x$, $Pd/Ti_3C_2T_x$, and $PtPd/Ti_3C_2T_x$. where the highly functionalized surface with abundant defects made MXene act as a reducing agent for the metal salts to form a uniform dispersed spherical NPs staked to the 2D-sheets without using any surfactant at RT with complete metal ions reduction under sonication.

References

1. Pan, X., et al., *Oxide–Zeolite-Based Composite Catalyst Concept That Enables Syngas Chemistry beyond Fischer–Tropsch Synthesis.* 2021. **121**(11): p. 6588-6609.
2. Abdulrasheed, A., et al., *A review on catalyst development for dry reforming of methane to*

syngas: Recent advances. 2019. **108**: p. 175-193.
3. Sun, X., et al., *Syngas fermentation process development for production of biofuels and chemicals: A review.* 2019. **7**: p. 100279.
4. Lebedeva, N., et al., *Mechanism and kinetics of the electrochemical CO adlayer oxidation on Pt (111).* 2002. **524**: p. 242-251.
5. Scott, S.B., et al., *Tracking oxygen atoms in electrochemical CO oxidation-Part II: Lattice oxygen reactivity in oxides of Pt and Ir.* 2021. **374**: p. 137844.
6. Eid, K., M.H. Sliem, and A.M.J.N. Abdullah, *Unraveling template-free fabrication of carbon nitride nanorods codoped with Pt and Pd for efficient electrochemical and photoelectrochemical carbon monoxide oxidation at RE.* 2019. **11**(24): p. 11755-11764.
7. Eid, K., et al., *Recent Advances in the Controlled Design of One-dimensional Carbon Nitrides for Thermal CO oxidation Reaction.* 2021.
8. Slavinskaya, E., et al., *Thermal activation of Pd/CeO2-SnO2 catalysts for low-temperature CO oxidation.* 2020. **277**: p. 119275.
9. Lu, Q., et al., *Engineering graphitic carbon nitride (gC 3 N 4) for catalytic reduction of CO 2 to fuels and chemicals: strategy and mechanism.* 2021. **23**(15): p. 5394-5428.
10. Eid, K., et al., *Precise fabrication of porous one-dimensional gC3N4 nanotubes doped with Pd and Cu atoms for efficient CO oxidation and CO2 reduction.* 2019. **107**: p. 107460.
11. Jones, J.P., G.S. Prakash, and G.A.J.I.J.o.C. Olah, *Electrochemical CO2 reduction: recent advances and current trends.* 2014. **54**(10): p. 1451-1466.
12. Bagger, A., et al., *Electrochemical CO2 reduction: a classification problem.* 2017. **18**(22): p. 3266-3273.
13. Lu, Q., et al., *Facile one-step aqueous-phase synthesis of porous PtBi nanosponges for efficient electrochemical methanol oxidation with a high CO tolerance.* 2022. **916**: p. 116361.
14. Dey, S. and G.C. Dhal, *Materials progress in the control of CO and CO2 emission at ambient conditions: an overview.* Materials Science for Energy Technologies, 2019. **2**(3): p. 607-623.
15. Salomons, S., et al., *CO and H2 oxidation on a platinum monolith diesel oxidation catalyst.* Catalysis Today, 2006. **117**(4): p. 491-497.
16. Petrov, L., et al., *Role of chemical kinetics in the heterogeneous catalysis studies.* Chinese Journal of Catalysis, 2011. **32**(6-8): p. 1085-1112.
17. Li, F., J. Zhao, and Z. Chen, *Fe-anchored graphene oxide: a low-cost and easily accessible catalyst for low-temperature CO oxidation.* The Journal of Physical Chemistry C, 2012. **116**(3): p. 2507-2514.
18. Lyu, P., J. He, and P. Nachtigall, *Theoretical investigation of CO catalytic oxidation by a Fe–PtSe 2 monolayer.* RSC advances, 2017. **7**(32): p. 19630-19638.
19. Dey, S. and G.C. Dhal, *A review of synthesis, structure and applications in hopcalite catalysts for carbon monoxide oxidation.* Aerosol Science and Engineering, 2019: p. 1-35.
20. Dey, S., et al., *Advances in transition metal oxide catalysts for carbon monoxide oxidation: a review.* Advanced Composites and Hybrid Materials, 2019: p. 1-31.
21. Guo, Y., et al., *Copper manganese oxides supported on multi-walled carbon nanotubes as an efficient catalyst for low temperature CO oxidation.* 2016. **146**(11): p. 2364-2375.
22. Xie, Y., et al., *A highly-efficient La–MnO x catalyst for propane combustion: the promotional role of La and the effect of the preparation method.* 2016. **6**(23): p. 8222-8233.
23. Yang, H., et al., *Effect of mesoporous g-C3N4 substrate on catalytic oxidation of CO over Co3O4.* 2017. **401**: p. 333-340.
24. Eid, K., et al., *Rational synthesis of one-dimensional carbon nitride-based nanofibers atomically doped with Au/Pd for efficient carbon monoxide oxidation.* 2019. **44**(33): p. 17943-17953.
25. Yu, Y., et al., *A rat RNA-Seq transcriptomic BodyMap across 11 organs and 4 developmental stages.* 2014. **5**(1): p. 1-11.
26. Kumar, R., et al., *Nanohole-structured and palladium-embedded 3D porous graphene for ultrahigh hydrogen storage and CO oxidation multifunctionalities.* 2015. **9**(7): p. 7343-7351.
27. Teixeira-Neto, A., et al., *Surface composition and structural changes on titanium oxide-supported AuPd nanoparticles during CO oxidation.* 2017. **7**(8): p. 1679-1689.
28. Ma, T.Y., Z.Y. Yuan, and J.L. Cao, *Hydrangea-like meso-/macroporous ZnO-CeO2 binary oxide materials: synthesis, photocatalysis and CO oxidation*. 2010, Wiley Online Library.

29. Fan, L., et al., *Structural Isomerism of Two Ce-BTC for Fabricating Pt/CeO2 Nanorods toward Low-Temperature CO oxidation* 2020. **16**(40): p. 2003597.
30. Royer, S. and D.J.C. Duprez, *Catalytic oxidation of carbon monoxide over transition metal oxides.* 2011. **3**(1): p. 24-65.
31. Njagi, E.C., et al., *Total oxidation of CO at ambient temperature using copper manganese oxide catalysts prepared by a redox method.* 2010. **99**(1-2): p. 103-110.
32. Shi, Y., et al., *CO oxidation over Cu 2 O deposited on 2D continuous lamellar gC 3 N 4.* 2015. **39**(8): p. 6642-6648.
33. Liu, S. and S.J.A.S.S. Huang, *Atomically dispersed Co atoms on MoS2 monolayer: a promising high-activity catalyst for CO oxidation.* 2017. **425**: p. 478-483.
34. Ma, D., et al., *CO catalytic oxidation on iron-embedded monolayer MoS2.* 2015. **328**: p. 71-77.
35. Li, D., W. Li, and J.J.A.S.S. Zhang, *Al doped MoS2 monolayer: a promising low-cost single atom catalyst for CO oxidation.* 2019. **484**: p. 1297-1303.
36. Yang, J., et al., *Oxygen vacancy promoted O2 activation over perovskite oxide for low-temperature CO oxidation.* 2019. **9**(11): p. 9751-9763.
37. Venezia, A., et al., *Activity of SiO2 supported gold-palladium catalysts in CO oxidation.* 2003. **251**(2): p. 359-368.
38. Suo, Z., et al., *The active phase of Au–Pd/Al2O3 for CO oxidation.* 2008. **9**(13): p. 2187-2190.
39. Roy, S., et al., *Creation of redox adsorption sites by Pd2+ ion substitution in nanoTiO2 for high photocatalytic activity of CO oxidation, NO reduction, and NO decomposition.* 2007. **111**(23): p. 8153-8160.
40. Hwang, S., M.C. Lee, and W.J.A.C.B.E. Choi, *Highly enhanced photocatalytic oxidation of CO on titania deposited with Pt nanoparticles: kinetics and mechanism.* 2003. **46**(1): p. 49-63.
41. Li, Q., et al., *Effect of photocatalytic activity of CO oxidation on Pt/TiO2 by strong interaction between Pt and TiO2 under oxidizing atmosphere.* 2006. **258**(1-2): p. 83-88.
42. Zhang, T., S. Wang, and F.J.T.J.o.P.C.C. Chen, *Pt–Ru bimetal alloy loaded TiO2 photocatalyst and its enhanced photocatalytic performance for CO oxidation.* 2016. **120**(18): p. 9732-9739.
43. McPherson, I.J., et al., *Electrochemical CO oxidation at platinum on carbon studied through analysis of anomalous in situ IR spectra.* 2017. **121**(32): p. 17176-17187.
44. Spendelow, J., et al., *Mechanism of CO oxidation on Pt (111) in alkaline media.* 2006. **110**(19): p. 9545-9555.
45. Davies, J.C., B.E. Hayden, and D.J.J.E.a. Pegg, *The electrooxidation of carbon monoxide on ruthenium modified Pt (110).* 1998. **44**(6-7): p. 1181-1190.
46. Ueda, A., et al., *Electrochemical oxidation of CO in sulfuric acid solution over Pt and PtRu catalysts modified with TaOx and NbOx.* 2003. **84**(3-4): p. 223-229.
47. Ciapina, E.G., S.F. Santos, and E.R.J.J.o.E.C. Gonzalez, *The electrooxidation of carbon monoxide on unsupported Pt agglomerates.* 2010. **644**(2): p. 132-143.
48. Wu, F., et al., *Unveiling one-pot template-free fabrication of exquisite multidimensional PtNi multicube nanoarchitectonics for the efficient electrochemical oxidation of ethanol and methanol with a great tolerance for CO.* 2020. **12**(28): p. 31309-31318.
49. Weir, M.G., et al., *In situ X-ray absorption analysis of ~ 1.8 nm dendrimer-encapsulated Pt nanoparticles during electrochemical CO oxidation.* 2010. **11**(13): p. 2942-2950.
50. Matsui, T., et al., *Electrochemical oxidation of CO over tin oxide supported platinum catalysts.* 2006. **155**(2): p. 152-156.
51. Eid, K., et al., *Rational one-step synthesis of porous PtPdRu nanodendrites for ethanol oxidation reaction with a superior tolerance for CO-poisoning.* 2017. **9**(47): p. 18881-18889.
52. Sun, M., et al., *CO-tolerant PtRu@ h-BN/C core–shell electrocatalysts for proton exchange membrane fuel cells.* 2018. **450**: p. 244-250.
53. Soliman, N.J.J.o.M.R. and Technology, *Factors affecting CO oxidationreaction over nanosized materials: A review.* 2019. **8**(2): p. 2395-2407.
54. Santos, V.P., et al., *Oxidation of CO, ethanol and toluene over TiO2 supported noble metal catalysts.* 2010. **99**(1-2): p. 198-205.
55. Zhou, Y., et al., *Covalent organic polymer supported palladium catalysts for CO oxidation.* 2013. **49**(50): p. 5633-5635.
56. Fang, C., et al., *Ru nanoworms loaded TiO2 for their catalytic performances toward CO*

oxidation. 2021. **13**(4): p. 5079-5087.
57. Tanikawa, K. and C.J.A.C.A.G. Egawa, *Effect of barium addition on CO oxidation activity of palladium catalysts.* 2011. **403**(1-2): p. 12-17.
58. Carlsson, P.-A. and M.J.A.C.B.E. Skoglundh, *Low-temperature oxidation of carbon monoxide and methane over alumina and ceria supported platinum catalysts.* 2011. **101**(3-4): p. 669-675.
59. Oran, U. and D.J.A.C.B.E. Uner, *Mechanisms of CO oxidation reaction and effect of chlorine ions on the CO oxidationreaction over Pt/CeO2 and Pt/CeO2/γ-Al2O3 catalysts.* 2004. **54**(3): p. 183-191.
60. Cheng, C., et al., *Single Pd atomic catalyst on Mo 2 CO 2 monolayer (MXene): unusual activity for CO oxidation by trimolecular Eley–Rideal mechanism.* 2018. **20**(5): p. 3504-3513.
61. Cheng, C., et al., *Cu3-cluster-doped monolayer Mo2CO2 (MXene) as an electron reservoir for catalyzing a CO oxidation reaction.* 2018. **10**(38): p. 32903-32912.
62. Alavi, A., P. Hu, and T.J.P.R.L. Deutsch, *Silvestrellij, PL Uuml, R. Hutter.* 1998. **80**: p. 3650-3653.
63. Zhang, C. and P.J.J.o.t.A.C.S. Hu, *Why must oxygen atoms be activated from hollow sites to bridge sites in catalytic CO oxidation?* 2000. **122**(9): p. 2134-2135.
64. Cheng, C., et al., *Identification of High-Performance Single-Atom Mxenes Catalysts for Low-TemperatureCO oxidation.* 2019. **2**(8): p. 1900006.
65. Cheng, C., X. Zhang, and Z.J.J.o.P.C.M. Yang, *Low-temperature preferential oxidation of CO over Ag monolayer decorated Mo2C (MXene) for purifying H2.* 2019. **31**(21): p. 215201.
66. Zhang, X., et al., *A Ti-anchored Ti 2 CO 2 monolayer (MXene) as a single-atom catalyst for CO oxidation.* 2016. **4**(13): p. 4871-4876.
67. Gogotsi, Y. and B.J.A.n. Anasori, *The rise of MXenes*. 2019, ACS Publications. p. 8491-8494.
68. Naguib, M., et al., *Two-dimensional nanocrystals produced by exfoliation of Ti3AlC2.* 2011. **23**(37): p. 4248-4253.
69. Ibrahim, Y., et al., *A review of MXenes as emergent materials for dye removal from wastewater.* 2022. **282**: p. 120083.
70. Ghidiu, M., et al., *Conductive 2-D titanium carbide 'clay'with high volumetric capacitance.* 2014. **516**(7529): p. 78-81.
71. Huang, K., et al., *2-D transition metal carbides and nitrides (MXenes) for biomedical applications.* 2018. **47**(14): p. 5109-5124.
72. Yang, S., et al., *Fluoride-free synthesis of two-dimensional titanium carbide (MXene) using a binary aqueous system.* 2018. **130**(47): p. 15717-15721.
73. Rasheed, P.A., et al., *Nb-based MXenes for efficient electrochemical sensing of small biomolecules in the anodic potential.* 2020. **119**: p. 106811.
74. Mei, J., et al., *2-D fluorine-free mesoporous Mo2C MXene via UV-induced selective etching of Mo2Ga2C for energy storage.* 2020. **25**: p. e00156.
75. Xiao, X., et al., *Salt-templated synthesis of 2D metallic MoN and other nitrides.* 2017. **11**(2): p. 2180-2186.
76. Gogotsi, Y.J.N.m., *Transition metal carbides go 2D.* 2015. **14**(11): p. 1079-1080.
77. Naguib, M., et al., *2-D transition metal carbides.* 2012. **6**(2): p. 1322-1331.
78. Zhao, D., et al., *MXene (Ti3C2) vacancy-confined single-atom catalyst for efficient functionalization of CO2.* 2019. **141**(9): p. 4086-4093.
79. Salah, B., et al., *Titanium Carbide (Ti3C2Tx) MXene Ornamented with Palladium Nanoparticles for Electrochemical COoxid.* 2022. **34**(4): p. 677-683.
80. Alhabeb, M., et al., *Guidelines for synthesis and processing of 2-D titanium carbide (Ti3C2T x MXene).* 2017. **29**(18): p. 7633-7644.
81. Feng, A., et al., *2-D MXene Ti3C2 produced by exfoliation of Ti3AlC2.* 2017. **114**: p. 161-166.
82. Ghidiu, M., et al., *Synthesis and characterization of 2-D Nb 4 C 3 (MXene).* 2014. **50**(67): p. 9517-9520.
83. Melchior, S.A., et al., *High-voltage symmetric supercapacitor based on 2D titanium carbide (MXene, Ti2CTx)/carbon nanosphere composites in a neutral aqueous electrolyte.* 2018. **165**(3): p. A501.
84. Hope, M.A., et al., *NMR reveals the surface functionalisation of Ti 3 C 2 MXene.* 2016. **18**(7): p. 5099-5102.
85. Zhan, X., et al., *MXene and MXene-based composites: synthesis, properties and environment-*

related applications. 2020. **5**(2): p. 235-258.
86. Halim, J., et al., *Transparent conductive 2-D titanium carbide epitaxial thin films.* 2014. **26**(7): p. 2374-2381.
87. Malaki, M., A. Maleki, and R.S.J.J.o.M.C.A. Varma, *MXenes and ultrasonication.* 2019. **7**(18): p. 10843-10857.

CHAPTER 3

Titanium Carbide ($Ti_3C_2T_x$) MXene Ornamented with Pallidum Nanoparticles for Electrochemical CO oxidation

Abstract

Titanium carbide ($Ti_3C_2T_x$) MXene possesses various unique physicochemical and catalytic properties. However, the electrochemical CO_{oxid} performance is not yet addressed experimentally. Herein, $Ti_3C_2T_x$ (T_X=OH, O, and F) ordered and exfoliated 2-D nanosheets ornamented with semi-spherical pallidum nanoparticles (2.5 Wt. %) with an average diameter of (10 ±1 nm) (denoted as $Pd/Ti_3C_2T_x$) is rationally designed for the electrochemical CO_{oxid}. The fabrication process is based on the selective chemical etching of Ti_3AlC_2 and delamination under sonication to form Ti_3C_2Tx nanosheets that are used as a substrate and reducing agent for supporting in situ growth of Pd nanoparticles via impregnation with Pd salt. Interestingly, Pd-free $Ti_3C_2T_x$ displayed inferior CO_{oxid} activity, while $Pd/Ti_3C_2T_x$ enhanced the CO_{oxid} activity substantially. This is attributed to the combination of outstanding physicochemical properties of $Ti_3C_2T_x$ and the catalytic merits of Pd nanoparticles.

Introduction

Proton exchange membrane fuel cells are promising green, sustainable, and efficient energy conversion technologies; however, the CO poisoning diminishes their performance [1-3] . Therefore, the CO_{oxid} reaction is of particular interest in industrial, fuel cells, and environmental applications. [4, 5] Wide varieties of noble metals [6], transition metals [7, 8], and carbon nitride [9-14] were used for catalytic $_{COoxid}$. Pd nanoparticles are among the most effective catalysts for the electrochemical CO_{oxid}, but their high cost and self-poisonings are critical issues precluding large-scale applications. These obstacles could be defeated by controlling the shape [15] and composition [16, 17] of Pd nanoparticle as well as using a metal-oxide support [18, 19].

Distinct from other supports, $Ti_3C_2T_x$ MXene possesses various unique physicochemical properties and catalytic properties such as high surface area, rich electron density, abundant active sites, great defects, and high electrical conductivity endowing their utilization in different energy and environmental applications [20-28]. Additionally, the surface of the multi-layered 2D structure can be terminated with abundant surface functionalities (i.e., O_2, OH, and F), which provides accessible catalytic sites, accelerates charge mobility, promotes chemisorption of reactants, and tolerates the

binding energies of both CO_{oxid} intermediates and products [25, 28-30]. Notably, MXene could be easily prepared in a high yield from earth-abundant and inexpensive resources that are highly required merits in the practical applications [31]. Despite the significant achievements in the controlling design of $Ti_3C_2T_x$ for various applications, their electrocatalytic CO_{oxid} performance is not yet addressed experimentally. To the best of our knowledge, the catalytic oxidation of CO on Ti_3C_2Tx has been addressed only theoretically [29, 32, 33]. For example, Mo_2CS_2 with non-noble metal single-atom catalyst showed a promising CO_{oxid} activity, owing to the charge transfer from the surface to the adsorbed CO and O_2, allowing their activation over the catalyst surface [34]. The CO_{oxid} activity of Pd single-atom on Mo_2CO_2 (Pd/Ov-Mo_2CO_2) was predicted to be superior to Pd (111) and was close to the activity of Pt (111) at low CO coverage [35]. Ti anchored on Nobel-metal free Ti_2CO_2 exhibited a great CO_{oxid} activity and could be achieved experimentally [33].

In this work, $Ti_3C_2T_x$ decorated with pallidum nanoparticles (Pd/$Ti_3C_2T_x$) were synthesized and used for the electrocatalytic CO_{oxid}. Ti_3AlC_2 was initially etched by hydrofluoric acid and then delaminated under sonication to form $Ti_3C_2T_x$. The formed $Ti_3C_2T_x$ nanosheets were subsequently impregnated with Pd salt to form Pd/$Ti_3C_2T_x$. The fabrication process was simple, reducing agent-free, and enabled the formation of uniform exfoliated 2D nanosheets decorated with well-dispersed semi-spherical Pd nanoparticles with an average diameter of (10 ±1 nm). The electrochemical CO_{oxid} activity of Pd/$Ti_3C_2T_x$ was investigated and compared with Pd-free $Ti_3C_2T_x$ in perchloric acid at RE.

Experimental

Chemicals and materials

Sodium tetrachloropalladate (II) ((Na_2PdCl_4), 99%), acetone (≥ 99.9 %), hydrofluoric acid (48 Wt. %), and dimethyl sulfoxide anhydrous ((DMSO), ≥ 99.9 %) were purchased from Sigma-Aldrich Chemie GmbH (Munich, Germany). Aluminum titanium carbide powder (Ti_3AlC_2, 99.9 %, 40 µm particle size) was purchased from Carbon-Ukraine ltd (Kiev, Ukraine).

Synthesis of Ti3C2Tx nanosheets

$Ti_3C_2T_x$ nanosheets were synthesized by etching of Ti_3AlC_2 (2 g) powder by HF (40 ml, 50 Wt. %) under magnetic stirring atRTovernight, then centrifuged at 3500 rpm and washed with double deionized H_2O (D-H_2O) till the pH ≥ 5. The wet sediment 2 g was dispersed in 30 mL DMSO under magnetic stirring overnight atRTand then centrifuged at 3500 rpm for 4 min and washed with D-H_2O three times before being sonicated under argon. The final product was purified by centrifugation at 4000 rpm for 1 hr, and the supernatant was finally dried overnight under vacuum at 50 ^oC.

Synthesis of Pd/Ti3C2Tx

An aqueous solution of $Ti_3C_2T_x$ (20 mL of 12 mg /mL) was slowly mixed with Na_2PdCl_4 (2 mL of 20 mM) under sonication atRTfor 15 min followed by addition of acetone (10 mL) and kept for 2 h. [36] The solution was centrifuged for 10 min three times at 7000 rpm and washed with D-H_2O. The as-obtained sediment was vacuum dried at 50 ^oC overnight and then kept for further characterization and usage.

Materials characterization

The shape of thus obtained materials was analyzed by scanning electron microscope ((SEM), Hitachi S-4800, Hitachi, Tokyo, Japan) and transmission electron microscope (TEM, TecnaiG220, FEI, Hillsboro, OR, USA) equipped with selected area diffraction pattern (SAED). The X-ray photoelectron spectroscopy (XPS) spectra were recorded on a Kratos Axis (Ultra DLD XPS Kratos, Manchester, UK). The X-ray diffraction patterns (XRD) were measured on an X-ray diffractometer (X'Pert-Pro MPD, PANalytical Co., Almelo, Netherlands).

Electrochemical CO oxidation reaction

The electrochemical CO_{oxid} tests were conducted using on Gamry work-station (reference 3000, Gamry Co., USA) using the traditional three-electrode cell including Pt wire (counter electrode), leak-free Ag/AgCl (KCl, 3 M)) (reference electrode), and glassy carbon electrode ((GCE) (WE). The catalyst inks were prepared by mixing 2 mg of each catalyst in 1 mL of deionized H_2O/ethanol (3/1 v/v ratio) contains Nafion solution (30 µL, 0.05 Wt %) under sonication until getting a homogeneous solution. The catalyst inks (10 µg of each catalyst) were cast onto GC electrodes and then left to dry under vacuum at 50 ^oC.

Results and discussion

Figure 1a shows the SEM image of $Ti_3C_2T_x$ formed in a multilayered 2-D nanosheets morphology with an average thickness of nearly 1.9 nm. The nanosheets are exfoliated with an interlayer space of 50 ± 10 nm (Figure 1b). The as-obtained $Ti_3C_2T_x$ nanosheets were used as a substrate and reducing agent for supporting the growth of Pd nanoparticles. The formation of Pd nanoparticles over $Ti_3C_2T_x$ nanosheets enhanced the exfoliation of the obtained nanosheets (Figure 1c). Figure 1d shows the TEM image of Pd/ $Ti_3C_2T_x$ that reveals the formation of 2-D thin nanosheets decorated with Pd nanoparticles.

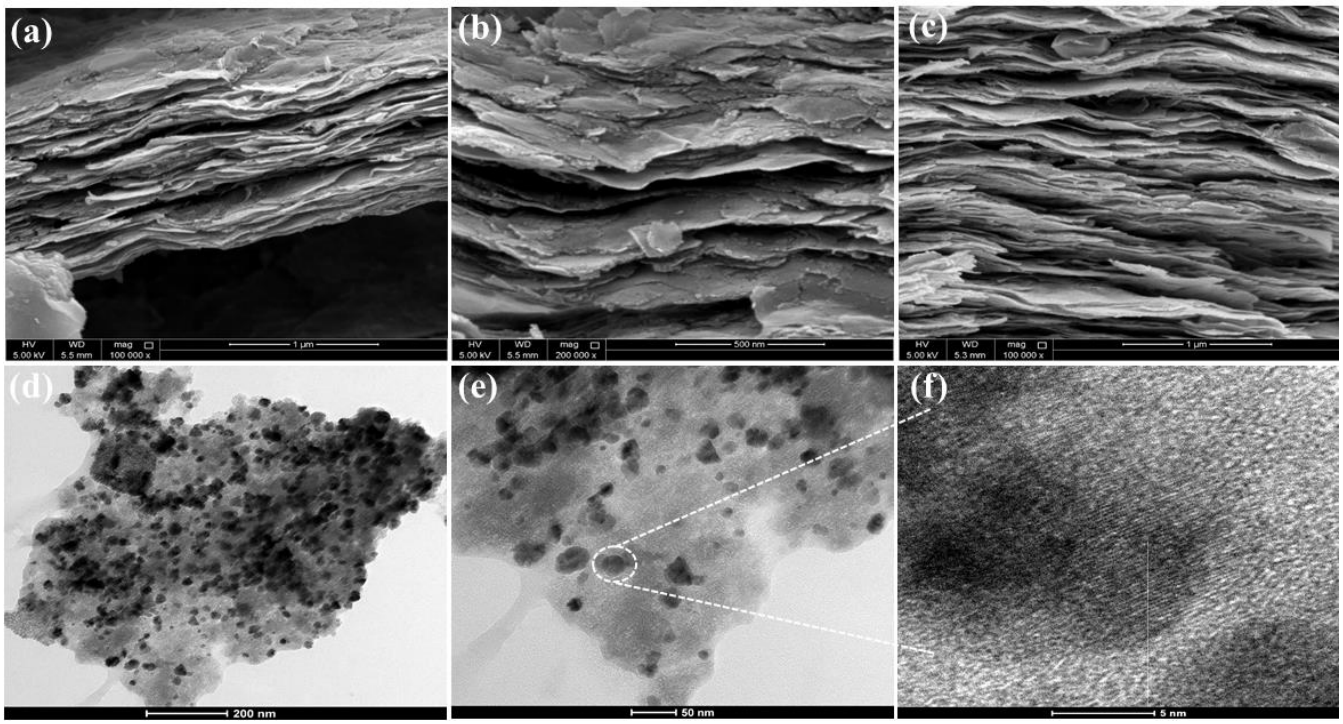


Figure 3.1 (a-b) SEM image of $Ti_3C_2T_x$ MXene. SEM image (c) and TEM images (d-e) of $Pd/Ti_3C_2T_x$, HRTEM (f) of the marked area in (e)

Interestingly, Pd nanoparticles were highly dispersed over $Ti_3C_2T_x$ and had a semispherical shape with an average size of (10 ±1 nm) (Figure 1e). The high-resolution TEM image of Pd nanoparticles depicts uniform lattice fringes arranged in one direction without any defects or lattice distortion, implying the absence of any undesired microscopic phases (Figure 1f). The interlayer d-spacing of the Pd lattice is estimated to be 2.29 A, attributed to the (111) facet of face-centered cubic (fcc) Pd. The selected area electron diffraction (SAED) pattern of randomly selected Pd nanoparticles shows the typical rings associated with the diffraction of (111), (200), and (220) facets of the fcc Pd structure (Figure 2a).

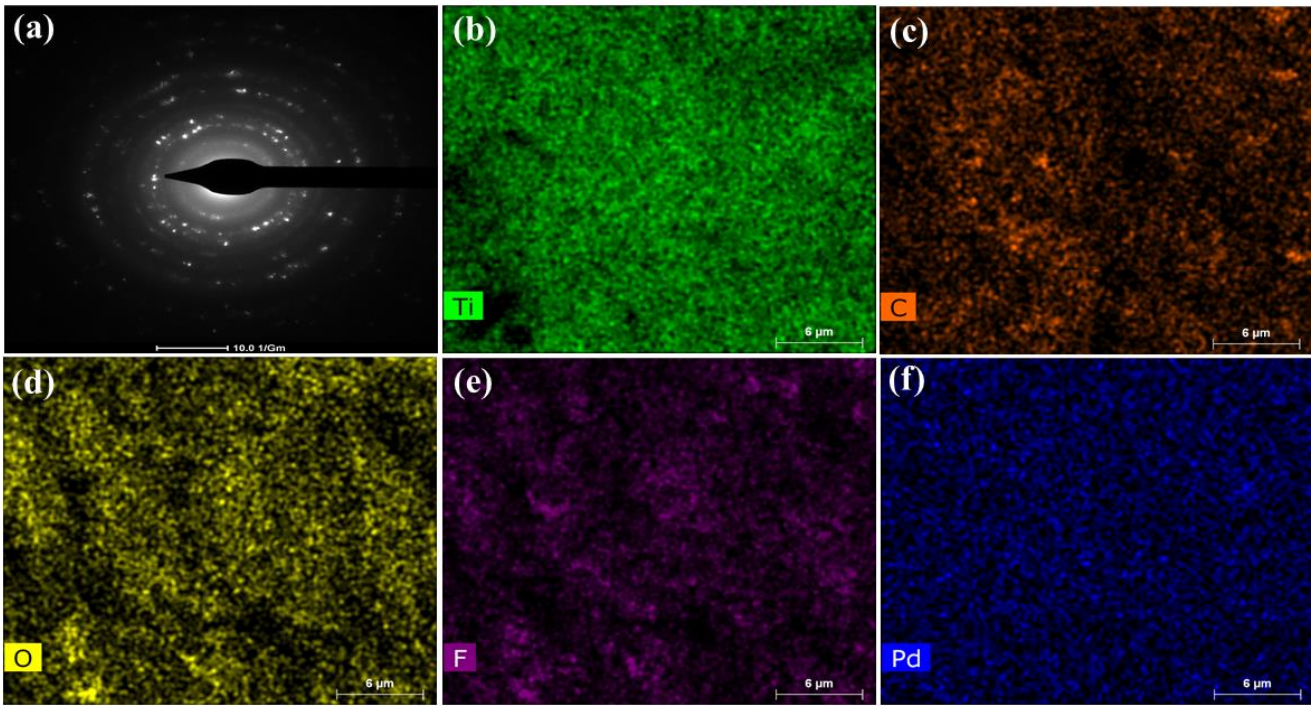


Figure 3.2 (a) SAED and elemental mapping images of (b) Ti, (c) C, (d) O, (e) F, and (f) Pd of $Pd/Ti_3C_2T_x$.

The elemental mapping analysis of thus formed $Pd/Ti_3C_2T_x$ reveals the presence of titanium (Ti) (Figure 2b), carbon (C) (Figure 2c), oxygen (O) (Figure 2d), fluoride (F) (Figure 2e), and palladium (Figure 2f) with atomic contents of 50.09, 30.79, 10.2, 6.7, 2.5 %, respectively. The presence of -F surface termination in $Ti_3C_2T_x$ is due to HF etching, while the detected -O surface termination is attributed to the intercalation by DMSO. The surface terminations T_x are plausibly important for enhancing the hydrophilicity of $Pd/Ti_3C_2T_x$, as well as promoting the adsorption and activation of gas molecules (CO and O_2) reactants during the CO_{oxid} [29, 32, 33].

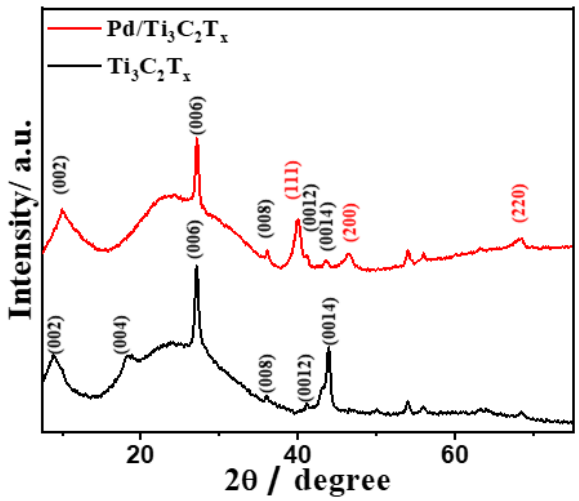


Figure 3.3 XRD analysis of $Pd/Ti_3C_2T_x$ and $Ti_3C_2T_x$

The crystalline structures of thus formed Pd/$Ti_3C_2T_x$ and $Ti_3C_2T_x$ were investigated by the XRD analysis (Figure 3). Pd-free $Ti_3C_2T_x$ exhibits the XRD diffraction patterns assigned to the (002), (004) ,(006), (008), (0012), (0014), facets of $Ti_3C_2T_x$ in line with reports elsewhere [11]. The absence of any peaks for TiO_2 nanoparticles reflects the uniformity of the formed $Ti_3C_2T_x$ MXene. Pd/$Ti_3C_2T_x$ display the diffraction peaks of $Ti_3C_2T_x$ in addition to (111), (200), and (220) facets of fcc Pd-metal [37]. The electronic structure and valence of Pd/$Ti_3C_2T_x$ relative to $Ti_3C_2T_x$ were investigated by the XPS analysis. Figure 4a discloses the XPS surveys for Pd/$Ti_3C_2TxT_x$ and $Ti_3C_2TxT_x$, which both display the valence band of Ti 2p, C 1s, O 1s, and F 1s, but Pd/$Ti_3C_2TxT_x$ shows an additional peak for Pd 3d. The high-resolution spectra of Ti 2p spectra display Ti-C [$2p_{3/2}$ (455.24 eV) and $2p_{1/2}$ (461.13 eV)], Ti^{2+} [$2p_{3/2}$ (456.25 eV), $2p_{1/2}$ (462.3 eV)], and Ti^{3+} [$2p_{3/2}$ (458 eV), $2p_{1/2}$ (463.38 eV) (Figure 4b). The C 1s spectra reveal C-C at (285 eV), C-OH at (286.95 eV), and C-O=C at (288.97 eV) (Figure 4c). The O 1s spectra exhibit O bonded to Ti at (530.02 eV) and OH at (531.03 eV) besides C-O at 532.8 eV (Figure 4d). The Fs1 spectra show Ti-F at (685 eV), and C bonded F (C-F) at (687.2 eV) (Figure 4e).

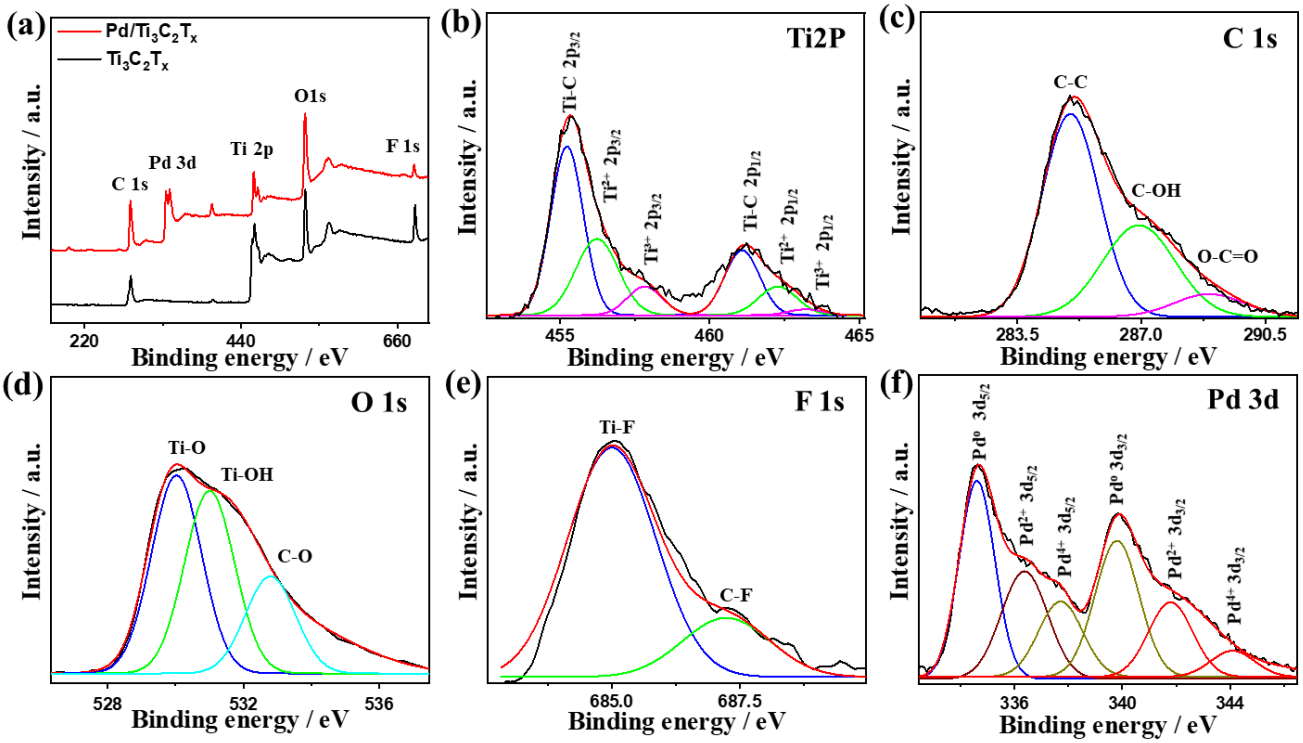


Figure 3.4 (a) XPS survey of Pd/$Ti_3C_2T_x$ and $Ti_3C_2T_x$. High-resolution XPS spectra of (b) Ti, (c) C, (d) O, (e) F, and (f) Pd

The Pd 3d spectra show Pd^0 ($3d_{3/2}$ at 339.79 eV and $3d_{5/2}$ at 334.6 eV), as a major phase and both Pd^{2+} ($3d_{3/2}$ at 341.75 eV and $3d_{5/2}$ at 336.34 eV) and Pd^{4+} ($3d_{3/2}$ at 344.08 eV and $3d_{5/2}$ at 337.72 eV)

as minor phases (Figure 4f). The presence of Pd^0 metallic state as a major phase indicates the great reduction power of $Ti_3C_2T_x$; meanwhile, the presence of Pd^{2+} and Pd^{4+} is plausibly attributed to the great content of O in $Ti_3C_2T_x$, which may facilitate partial oxidation of Pd.

The fabrication of $Ti_3C_2T_x$ with or without metal nanoparticles (i.e., Pd, Co, Au, and Ag) has attracted much great attention for various catalytic applications, but their utilization in the electrochemical CO_{oxid} reaction is not yet reported [38, 39]. In our study, the electrochemical CO_{oxid} reaction of $Pd/Ti_3C_2T_x$ as compared to $Ti_3C_2T_x$ was assessed by various techniques including the cyclic voltammogram (CVs), linear sweep voltammogram (LSV), electrochemical impedance spectroscopy (EIS), and chronoamperometry (I-T).

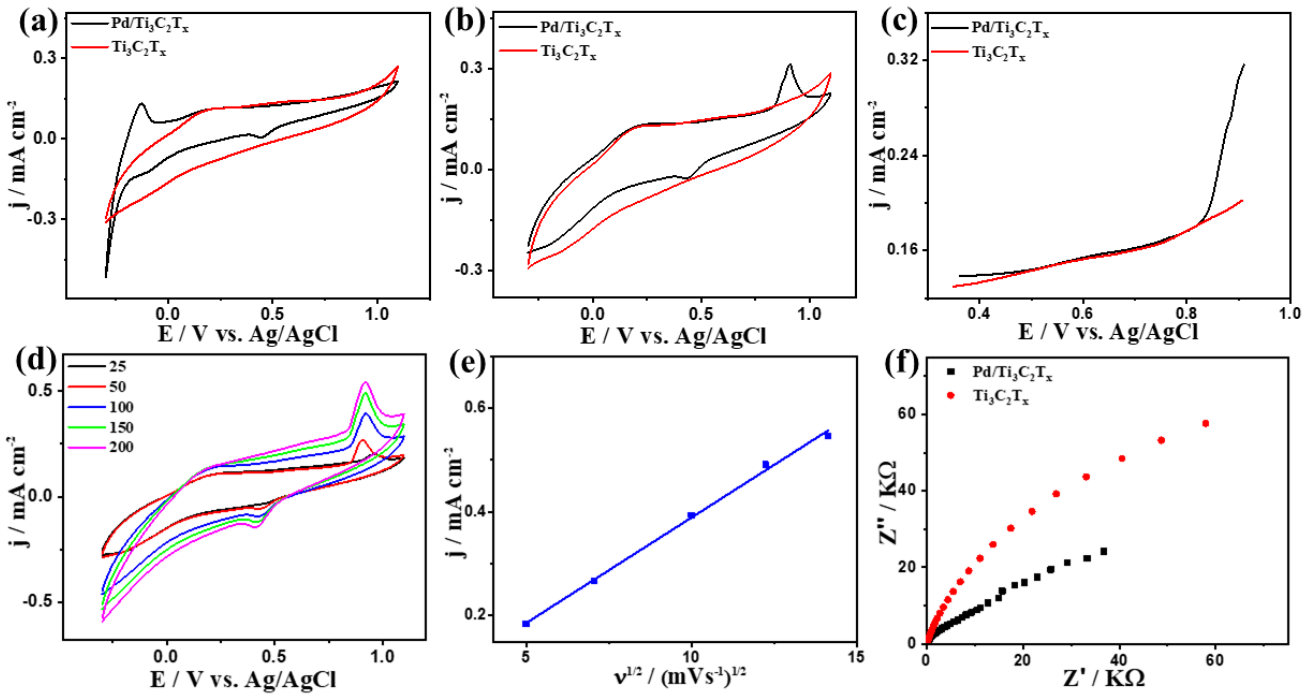


Figure 3.5 (a) CVs measured in a N_2 saturated 0.1 M $NaHCO_3$ of $Pd/Ti_3C_2T_x$ and $Ti_3C_2T_x$. (b) CVs and (c) LSV of $Pd/Ti_3C_2T_x$ and $Ti_3C_2T_x$. (d) CVs measured at different scan rates in a CO-saturated an aqueous solution of 0.1 M $HClO_4$ at 50 mV s^{-1} and (e) the corresponding plots of forwarding peak currents against the square root of the scan rates. (f) EIS of $Pd/Ti_3C_2T_x$ and $Ti_3C_2T_x$ measured in a frequency range from 100 kHz to 5 Hz with an AC voltage amplitude of 0.8 V at an open circuit potential in 0.1 M $HClO_4$.

Figure 5a shows the CVs measured in a nitrogen-saturated an aqueous solution of $HClO_4$ (0.1 M) at 50 mV s^{-1} at RE. It should be noted that initial CV were conducted at 200 mVs^{-1} for 50 segments to remove any impurities from the GCE surface. The CV curve of $Ti_3C_2T_x$ demonstrates quasi-

rectangular shape originating from the pseudo-capacitance effect, which is common in MXens or carbon-based materials. $Pd/Ti_3C_2T_x$ shows its typical voltammogram characteristics, including the double-layered $H_{ads/des}$ and Pd-O/Pd-H. The absence of any peak for TiO_2 or PdO in $Pd/Ti_3C_2T_x$ indicates its stability against oxidation or leaching in $HClO_4$ media. Figure 5b depicts the CVs curves of $Pd/Ti_3C_2T_x$, and $Ti_3C_2T_x$ measured in a CO-saturated an aqueous solution of $HClO_4$ (0.1 M) at RE. Pd-free $Ti_3C_2T_x$ voltammogram shows typical features of capacitive effect without any noticed activity for CO_{oxid}. Contrarily, $Pd/Ti_3C_2T_x$ has a prevalent CO_{oxid} activity with the typical voltammogram characteristics of CO-oxidation reaction, including a sharp anodic oxidation peak in the positive direction (0.82-1.01 V) and a small cathodic peak in the negative direction (0.37-0.51V). Figure 5c shows the LSV of $Pd/Ti_3C_2T_x$ tested in a CO-saturated $HCLO_4$ (0.1 M), which reveals the typical anodic oxidation features with a CO_{oxid} current density of (0.318 mA cm^{-2}), oxidation potential of (0.9 V) and onset potential around (0.75 V). The LSV of $Ti_3C_2T_x$ showed an inferior CO_{oxid} activity (Figure 5c). This is evident of the effect of Pd nanoparticles on boosting the CO_{oxid} activity of $Ti_3C_2T_x$.

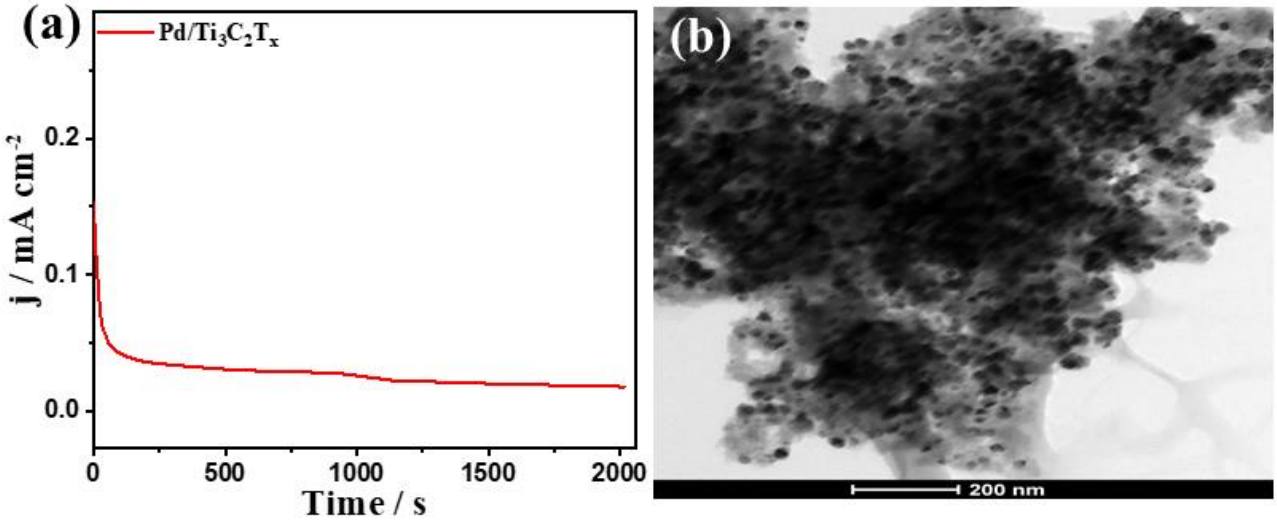


Figure 3.6 (a) The I-T tests measured for 2000 s at 0.8 V in a CO-saturated 0.1 M $HClO_4$, (b) TEM image of $Pd/Ti_3C_2T_x$ after CO_{oxid} stability test.

Figure 5d shows the CVs curves of $Pd/Ti_3C_2T_x$ measured at different sweeping rates of 25, 50, 100, 150, and 200 mV s^{-1} in a CO-saturated $HClO_4$ (0.5M), Incremental increases in the CO_{oxid} currents with increasing the sweeping rate can be seen. The maximum current density (0.544 $mAcm^{-2}$) was obtained at (200 mV s^{-1}) and the lowest current (0.2 $mAcm^{-2}$) was observed at (25 mV s^{-1}). Randles-Sevcik equation was used to demonstrate the effect of scan rate (v) over the CO_{oxid} current density as well as to determine the diffusion coefficient of the electroactive species (Figure 5e). Plotting current density vs. $v^{1/2}$ showed a linear relationship, which is evident of the diffusion-controlled

process for the electroactive species. The lower slope of the plot (0.04 mV dec^{-1}) indicates the fast reaction kinetics on $Pd/Ti_3C_2T_x$ surface. This is further seen in the EIS measurements, which display the lower charge transfer resistance of $Pd/Ti_3C_2T_x$ than that of $Ti_3C_2T_x$ (Figure 5f), which infers a better electrolyte-electrode interaction and quick charge transfer on $Pd/Ti_3C_2T_x$, owing to the presence of Pd nanoparticles. Figure 6a shows the I-T stability test measured on $Pd/Ti_3C_2T_x$ for 2000 s at 0.9 V in a CO-saturated 0.1 M $HClO_4$. $Pd/Ti_3C_2T_x$ showed good stability with a slight loss in the current density over time. The I-T test shows that $Pd/Ti_3C_2T_x$ maintains around 85 % of its initial current density (Figure 6a). The TEM image after stability tests shows the structural stability of $Pd/Ti_3C_2T_x$ without any significant leaching or aggregation for Pd nanoparticles (Figure 6b). These results warrants that coupling Pd nanoparticles with $Ti_3C_2T_x$ allows the slight enhancement in the CO_{oxid} activity. This is attributed to the combination of outstanding merits of $Ti_3C_2T_x$ (i.e., great surface area, rich electron density, accessible active sites, surface functionalities, hydrophilicity, and electrical conductivity) and unique catalytic properties of Pd (i.e., electronic effect, synergism, and adsorption/activation of CO/O_2 molecule). This facilitates the chemisorption of reactants and weakens the adsorption of CO_{oxid} intermediates or byproducts.

Conclusion

In summary, 2-D exfoliated $Ti_3C_2T_x$ (T_x = O, OH, and F) nanosheets covered with Pd nanoparticles ($Pd/Ti_3C_2T_x$) were prepared for the electrochemical CO_{oxid} reaction at RE. That is based on the initial HF etching of Ti_3AlC_2 and exfoliation under sonication to form $Ti_3C_2T_x$. The resultant was then mixed with Na_2PdCl_4 to allow its in-situ reduction with the assistance of highly active Ti vacancies without the need for a reducing agent. This allows the formation of uniform and exfoliated multilayered 2-D nanosheets decorated with semi-spherical Pd nanoparticles (2.5 Wt. %) with an average size of (10±1 nm). $Pd/Ti_3C_2T_x$ demonstrates a significant enhancement in the CO_{oxid} activity due to the combination of outstanding physiochemical of $Ti_3C_2T_x$ and catalytic merits of Pd nanoparticles such as synergism, electron density, quick charge mobility, and abundant active sites. This study may open new gates to synthesize $Ti_3C_2T_x$ decorated with various metal nanoparticles as catalysts for the CO_{oxid} reaction.

References

1. Lu, S., et al., *One-pot synthesis of PtIr tripods with a dendritic surface as an efficient catalyst for the oxygen reduction reaction.* 2017. **5**(19): p. 9107-9112.
2. Wang, H., et al., *Fabrication of mesoporous cage-bell Pt nanoarchitectonics as efficient catalyst for oxygen reduction reaction.* 2018. **6**(9): p. 11768-11774.
3. Wei, C., et al., *A Three-Dimensionally Structured Electrocatalyst: Cobalt-Embedded Nitrogen-Doped Carbon Nanotubes/Nitrogen-Doped Reduced Graphene Oxide Hybrid for Efficient Oxygen Reduction.* 2017. **23**(3): p. 637-643.

4. Tanaka, S., et al., *Gold nanoparticles supported on mesoporous iron oxide for enhanced CO oxidation reaction.* 2018. **10**(10): p. 4779-4785.
5. Grünert, W., et al., *Low-Temperature Oxidation of Carbon Monoxide with Gold (III) Ions Supported on Titanium Oxide.* 2014. **53**(12): p. 3245-3249.
6. Liu, X., et al., *Tuning the structure of bifunctional Pt/SmMn 2 O 5 interfaces for promoted low-temperature CO oxidation activity.* 2019. **11**(17): p. 8150-8159.
7. Xu, H., et al., *Identification of activity trends for CO oxidation on supported transition-metal single-atom catalysts.* 2017. **7**(24): p. 5860-5871.
8. Elias, J.S., et al., *In situ spectroscopy and mechanistic insights into CO oxidation on transition-metal-substituted ceria nanoparticles.* 2017. **7**(10): p. 6843-6857.
9. Eid, K., et al., *Data on structural and composition-related merits of gC3N4 nanofibres doped and undoped with Au/Pd at the atomic level for efficient catalytic CO oxidation.* 2019. **27**: p. 104734.
10. Eid, K. and A.M.J.D.i.b. Abdullah, *Data on the catalytic CO oxidation and CO2 reduction durability on gC3N4 nanotubes Co-doped atomically with Pd and Cu.* 2019. **26**: p. 104495.
11. Eid, K., et al., *Precise fabrication of porous one-dimensional gC3N4 nanotubes doped with Pd and Cu atoms for efficient CO oxidation and CO2 reduction.* 2019. **107**: p. 107460.
12. Eid, K., et al., *Rational synthesis of one-dimensional carbon nitride-based nanofibers atomically doped with Au/Pd for efficient carbon monoxide oxidation.* 2019. **44**(33): p. 17943-17953.
13. Eid, K., et al., *Rational synthesis of porous graphitic-like carbon nitride nanotubes codoped with Au and Pd as an efficient catalyst for carbon monoxide oxidation.* 2019. **35**(9): p. 3421-3431.
14. Eid, K., M.H. Sliem, and A.M.J.N. Abdullah, *Unraveling template-free fabrication of carbon nitride nanorods codoped with Pt and Pd for efficient electrochemical and photoelectrochemical carbon monoxide oxidation at RE.* 2019. **11**(24): p. 11755-11764.
15. Liu, X., et al., *Superior catalytic performance of atomically dispersed palladium on graphene in CO oxidation.* 2020. **10**(5): p. 3084-3093.
16. Xie, S., et al., *Highly Active and Stable Palladium Catalysts on Novel Ceria–Alumina Supports for Efficient Oxidation of Carbon Monoxide and Hydrocarbons.* 2021. **55**(11): p. 7624-7633.
17. Salama, R.S., et al., *Palladium supported on mixed-metal–organic framework (Co–Mn-MOF-74) for efficient catalytic oxidation of CO.* 2021. **11**(8): p. 4318-4326.
18. Zhang, X., et al., *Regulation of CO oxidation with Pd additives on Nb2CO2 MXene.* 2021. **46**(12): p. 8477-8485.
19. Farrag, M., et al., *Ligand-Protected Ultrasmall Pd Nanoclusters Supported on Metal Oxide Surfaces forCO oxidation: Does the Ligand Activate or Passivate the Pd Nanocatalyst?* 2021. **22**(3): p. 312-322.
20. Ibrahim, Y., et al., *Unveiling fabrication and environmental remediation of MXene-based nanoarchitectures in toxic metals removal from wastewater: strategy and mechanism.* 2020. **10**(5): p. 885.
21. Ibrahim, Y., et al., *The recent advances in the mechanical properties of self-standing 2-D MXene-based nanostructures: deep insights into the supercapacitor.* 2020. **10**(10): p. 1916.
22. Shi, Y.M., et al., *2D Accordion-like MXene Nanosheets as a Sensitive Electrode Material for Baicalin Sensing.* 2021. **33**(5): p. 1308-1314.
23. Lorencova, L., et al., *2D MXenes as perspective immobilization platforms for design of electrochemical nanobiosensors.* 2019. **31**(10): p. 1833-1844.
24. Alarcon-Angeles, G., M. Palomar-Pardavé, and A.J.E. Merkoçi, *2D materials-based platforms for electroanalysis applications.* 2018. **30**(7): p. 1271-1280.
25. Tahini, H.A., X. Tan, and S.C.J.C. Smith, *Facile CO oxidationon Oxygen-functionalized MXenes via the Mars-van Krevelen Mechanism.* 2020. **12**(4): p. 1007-1012.
26. Yang, C., et al., *Pd nanocrystals grown on MXene and reduced graphene oxide co-constructed three-dimensional nanoarchitectures for efficient formic acid oxidation reaction.* 2021. **46**(1): p. 589-598.
27. Li, X., et al., *Applications of MXene (Ti 3 C 2 T x) in photocatalysis: A review.* 2021. **2**(5): p. 1570-1594.
28. Cheng, C., et al., *Identification of High-Performance Single-Atom Mxenes Catalysts for Low-Temperature CO oxidation.* 2019. **2**(8): p. 1900006.
29. Zhang, Y., et al., *Recent progress of MXenes as the support of catalysts for the CO oxidation and*

oxygen reduction reaction. 2020. **31**(4): p. 931-936.
30. Morales-Garcia, A., F. Calle-Vallejo, and F.J.A.C. Illas, *MXenes: new horizons in catalysis.* 2020. **10**(22): p. 13487-13503.
31. Alhabeb, M., et al., *Guidelines for synthesis and processing of 2-D titanium carbide (Ti3C2T x MXene).* 2017. **29**(18): p. 7633-7644.
32. Cheng, C., et al., *Cu3-cluster-doped monolayer Mo2CO2 (MXene) as an electron reservoir for catalyzing a CO oxidation reaction.* 2018. **10**(38): p. 32903-32912.
33. Zhang, X., et al., *A Ti-anchored Ti 2 CO 2 monolayer (MXene) as a single-atom catalyst for CO oxidation.* 2016. **4**(13): p. 4871-4876.
34. Talib, S.H., et al., *Non-noble metal single-atom catalyst of Co1/MXene (Mo2CS2) for CO oxidation.* 2021. **64**(3): p. 651-663.
35. Engel, T. and G.J.T.J.o.C.P. Ertl, *A molecular beam investigation of the catalytic oxidation of CO on Pd (111).* 1978. **69**(3): p. 1267-1281.
36. Zhao, D., et al., *MXene (Ti3C2) vacancy-confined single-atom catalyst for efficient functionalization of CO2.* 2019. **141**(9): p. 4086-4093.
37. Li, C., et al., *One-pot synthesis of bimetallic PdCu nanoframes as an efficient catalyst for the methanol oxidation reaction.* 2018. **42**(2): p. 798-801.
38. Satheeshkumar, E., et al., *One-step solution processing of Ag, Au and Pd@ MXene hybrids for SERS.* 2016. **6**(1): p. 1-9.
39. Bharath, G., et al., *Hybrid Pd50-Ru50/MXene (Ti3C2Tx) nanocatalyst for effective hydrogenation of CO2 to methanol toward climate change control.* 2021. **414**: p. 128869.

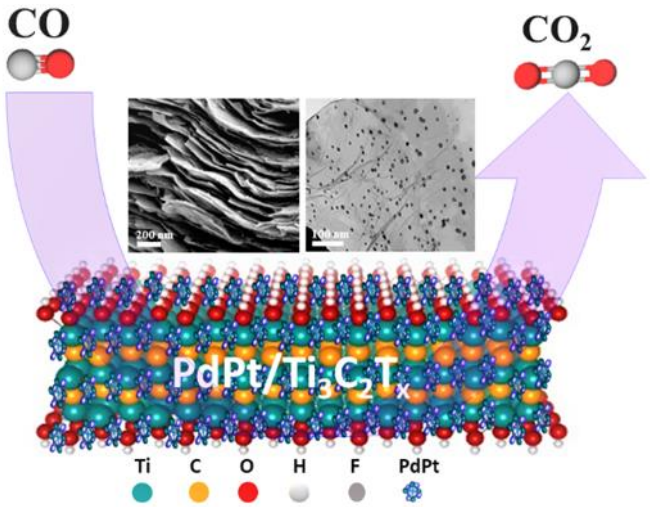
CHAPTER 4

Ti3C2Tx MXene Supported PdPt Nanoparticles for Electrochemical Oxidation of CO Over a Wide pH Range

Abstract

The engineering of CO_{oxid} electrocatalysts operating in various electrolytes is essential for multidisciplinary energy conversion technologies. Herein, unprecedented formation of titanium carbide ($Ti_3C_2T_x$) (T_X=OH, O, and F) ultrathin MXene nanosheets functionalized with palladium-platinum ($PdPt/Ti_3C_2T_x$) is reported; etching of Al in Ti_3AlC_2 followed by delamination under ultrasonic irradiation led to the fabrication of $Ti_3C_2T_x$ that is used as a reducing agent for Pd/Pt precursors to form PdPt nanoparticles. Mechanistically, the chemical etching of Al results in the formation of Ti-single vacancies/clusters and Ti-deficit defects that are not only highly reactive and reductive for Pd and Pt salts but also are ideal sites for adjust and stabilizing the ensuing PdPt nanoparticles at RT. Experimentally, the electrocatalytic CO_{oxid} activity of $PdPt/Ti_3C_2T_x$ was substantially superior to $Pd/Ti_3C_2T_x$, $Pt/Ti_3C_2T_x$, and pristine $Ti_3C_2T_x$ in neutral ($NaHCO_3$), acidic ($HClO_4$), and alkaline (KOH) electrolytes, owing to the electronic and synergetic effect of PdPt and physicochemical merits of $Ti_3C_2T_x$. Notably, the CO_{oxid} activity of $PdPt/Ti_3C_2T_x$ in $HClO_4$ is greater than that in $NaHCO_3$, and KOH under the same reaction conditions. This study may worship the way for the general utilization of $Ti_3C_2T_x$ in electrochemical CO_{oxid}.

Graphical Abstract

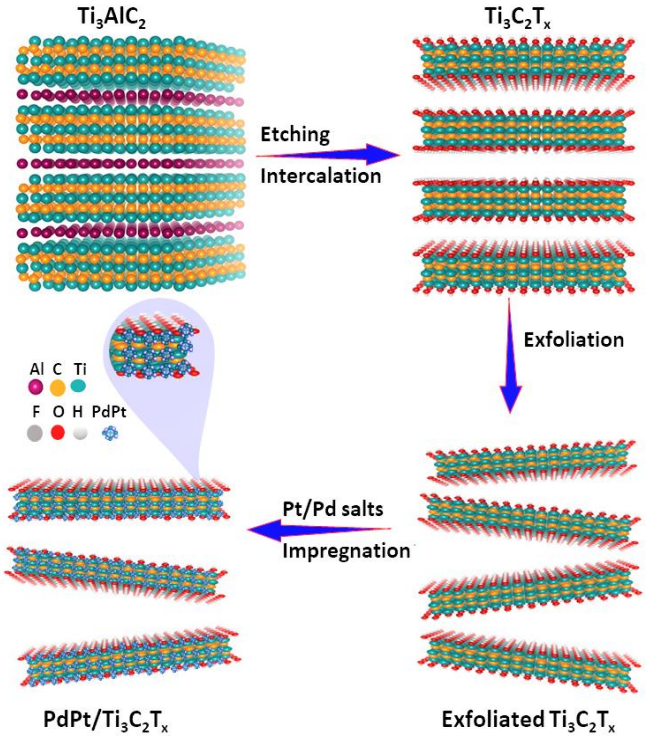


Introduction

The gas conversion reactions, especially the CO_{oxid} and CO_2 reduction are imperative in various

industrial, fuel cells, and environmental applications. [1-5] To date, wide varieties of noble/non-noble-metals (Au, Pd, Ag, and Pt [6-9]), transition metals/oxides (i.e., Mo, Ce, Mg, Ti, Fe, and Cu) [10-12], carbon nitride [13, 14], metal-organic framework [15], and MXenes [16] have been documented for CO_{oxid}. Pd and Pt nanoparticles remain the most promising electrocatalysts for CO_{oxid}, but their higher costs, low natural abundance, and instability for the long-term usage are the main barriers for their industrial applications. [17-19] Various efforts have been expanded to circumvent these limitations inducing altering the morphology (i.e., 0D, 1D, and 3D structures) and composition (i.e., alloying, intermetallic, and using support) of Pd and Pt nanoparticles. [20-24] Alloying Pd with Pt is among the most effective ways for enhancement of their catalytic activity and stability for various electrocatalytic appliances. [20-25] That is attributed to the electronic effect and synergism of PdPt, which improves the adsorption of CO and O_2 and facilitates the dissociation of O_2 and its subsequent binding with CO to form CO_2 at lower potential or low temperature leading to higher activity. [20, 21] Also, PdPt can weaken the adsorption of CO_{oxid} intermediates thus resulting in higher stability. For example, $Pd_{52}Pt_{48}$ showed a superior CO tolerance than commercial (Pt/C) catalyst in perchloric acid ($HClO_4$) solution. [26] The electrocatalytic CO_{oxid} activity of PtPdRu nanodendrites was superior to PtPdRu nanoflowers, PdPt nanodendrites, and commercial Pt/C catalysts in NaOH solution, indicating the shape and compositional effect. [27] Moreover, PdPt/carbon nitride nanorods significantly enhanced the CO_{oxid} activity than Pt/C and carbon nitride in KOH solution. [14] Besides, using a supporter with PdPt is an attractive alternative for enhancing the CO_{oxid} activity and stability duo to the interaction between PdPt and supporter can strengthen the adsorption of reactants in addation weaken the adsorption of intermediates and products. [21] Carbon materials (graphene oxide and carbon nanotubes) and transition metal oxides (i.e., TiO_2, Fe_2O_3, Cu_2O, and Ce_2O_3) are the most common supports for PdPt nanoparticles. [28-32] Unlike these supports, $Ti_3C_2T_x$ MXene is known for its abundant active sites, rich electron density, abundant surface functionalities (i.e., OH, O_2, and F), great defects, and great electrical conductivity, which are significant merits in various catalytic applications. [30, 33-39] Furthermore, $Ti_3C_2T_x$, with its 2-D multi-layered structure, can deliver abundant accessible catalytic positions for the reactants along with facilitating the desorption of products during the CO_{oxid} process. [34, 40-43] Notably, the CO_{oxid} reaction on MXenes or $Ti_3C_2T_x$ in different electrolytes has not been addressed yet experimentally, as earlier reports have been primarily theoretical, with Ti-based MXene being scarcely reported. [16, 34, 40, 44, 45] Most recently, we have prepared Pd nanoparticles supported on $Ti_3C_2T_x$ that enhanced the electrochemical CO_{oxid} significantly than bare $Ti_3C_2T_x$. [46] Thus, we envisioned that the combination of PdPt and $Ti_3C_2T_x$, can augment the CO_{oxid} performance.

Herein, PdPt nanoparticles-supported on $Ti_3C_2T_x$ (T_X=OH, O, and F) MXene were prepared for the electrochemical CO_{oxid}, including the initial preparation of $Ti_3C_2T_x$ by the HF method. The delamination under sonication facilitated the formation of exfoliated nanosheets with abundant Ti-defects and vacancies that subsequently served as an in situ powerful reducing agent for the reduction and growth of PdPt nanoparticles. That is a facile, surface-free, and reducing agent-free protocol that allows the production of uniform and exfoliated 2-D nanosheets with monodispersed PdPt NPs (10 ± 2 nm). In this unprecedented report, the electrochemical CO_{oxid} activity of PdPt/$Ti_3C_2T_x$ was benchmarked experimentally compared to individual components Pt/$Ti_3C_2T_x$, Pd/$Ti_3C_2T_x$, and metal-free $Ti_3C_2T_x$ over wide pH ranges in different electrolytes (i.e., $HCLO_4$, KOH, and $NaHCO_3$).



Scheme 4.1 The fabrication process of PdPt/$Ti_3C_2T_x$ N.

Results and discussion

Scheme 1 depicts the preparative procedure for PdPt/$Ti_3C_2T_x$, which comprises the etching of Ti_3AlC_2 by HF to incise Al and then intercalation with DMSO followed by ultrasonic treatment to exfoliate the sheets. Besides (Al, HF) leaches out some (Ti and C) resulting in abundant Ti single atom vacancies or vacancy clusters and Ti-deficit defects that are highly reactive and reductive attribute facilitate the reduction of Pd/Pt precursors beside accommodating the results PdPt nanoparticles. Meanwhile, both HF and DMSO interrelation results in abundant surface functionalities of F, OH, and O on the ensuing nanosheets. The SEM image of $Ti_3C_2T_x$ revealed

its uniform multilayered 2D nanosheets (Figure 1a), which are exfoliated with an average interlayer spacing of 20 nm ± 3. After the in-situ formation of Pd nanoparticles over $Ti_3C_2T_x$ ($Pd/Ti_3C_2T_x$ (Figure 1b) and Pt NPs over $Ti_3C_2T_x$ ($Pt/Ti_3C_2T_x$) (Figure 1c), multilayered 2D $Ti_3C_2T_x$ nanosheets which were additionally exfoliated with a larger interlayer spacing than the pristine $Ti_3C_2T_x$. The interlayer spacing of $Pd/Ti_3C_2T_x$ (60 nm ± 3) is little larger than that of $Pt/Ti_3C_2T_x$ (50 nm ± 3), plausibly attributed to atomic radius of Pd (140 pm) larger than Pt (135 pm). The growth of PdPt nanoparticles over $Ti_3C_2T_x$ ($PdPt/Ti_3C_2T_x$) rendered the nanosheets to be thinner and more exfoliated (Figure 1d). This is obvious in the larger interlayer spacing (80 nm ± 3) of $PdPt/Ti_3C_2T_x$ (Figure 1e) than $Pd/Ti_3C_2T_x$ or $Pt/Ti_3C_2T_x$ or bare $Ti_3C_2T_x$, due to the insertation of PdPt nanoparticles inside to the vacancies and defects of $Ti_3C_2T_x$. The TEM image reveals the well distribution of PdPt nanoparticles over $Ti_3C_2T_x$ ultrathin nanosheets (Figure 1f); PdPt nanoparticles have a spherical-like shape with diameter of around (13 ± 1 nm) (Figure 1g). This result is of particular interest, as the one-step formation of sub-20 nm binary PdPt atRThas been a grand challenge, as metal atoms collide to form small clusters, which are highly unstable thermodynamically and tend to continually grow into larger clusters to minimize the critical free energy barrier and finally forming nanoparticles. These results are of great significance as routinely, the formation of small-sized binary PdPt nanoparticles requires a strong reducing agent and heating to elevated temperature, while herein $Ti_3C_2T_x$ acts as a reducing agent and ensuing growth of PdPt nanoparticles at RE.

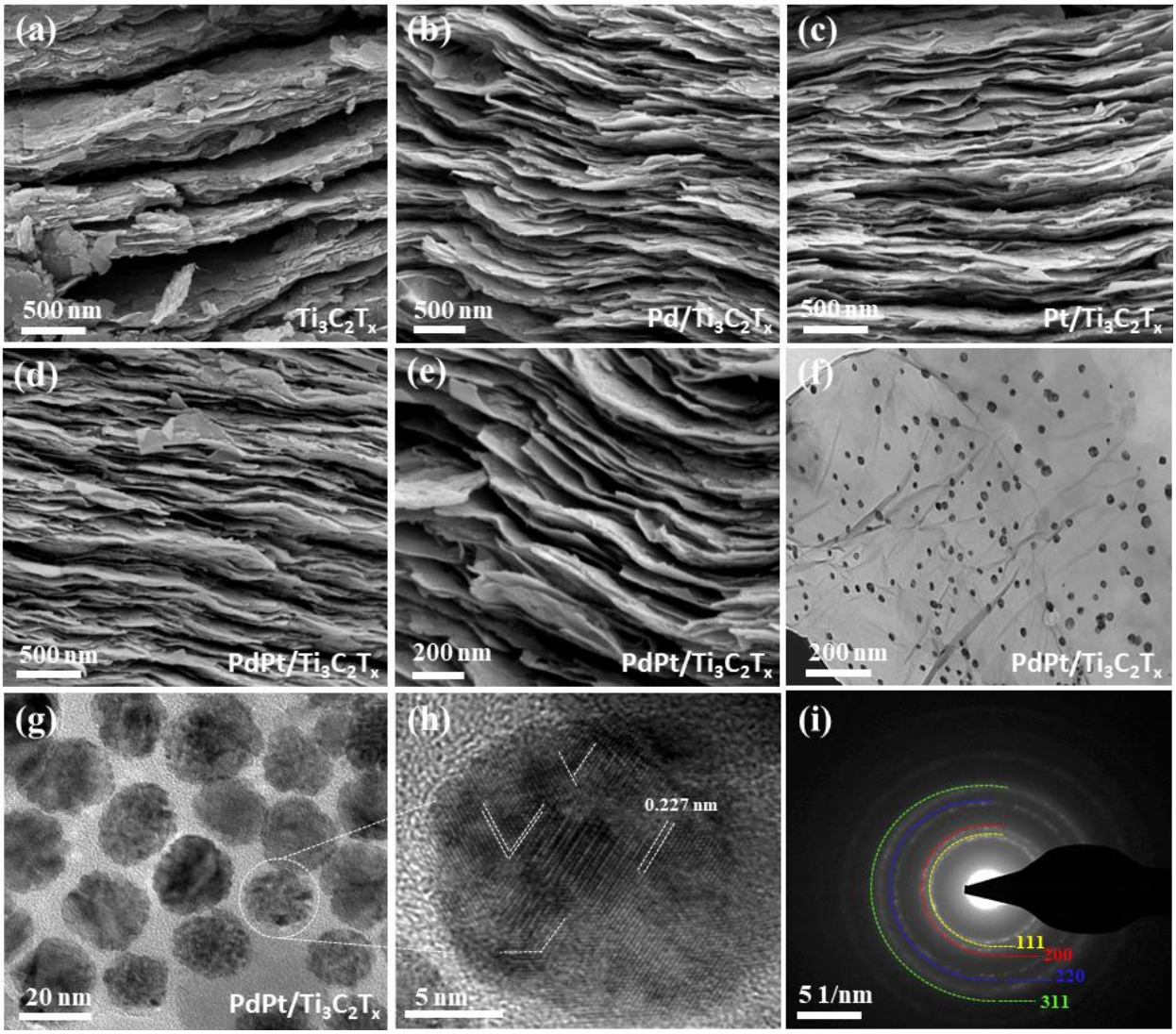


Figure 4.1 images of SEM for (Ti_3AlC_2 MXene, (b) $Pd/Ti_3C_2T_x$, (c) $Pt/Ti_3C_2T_x$, (d-e) $PdPt/Ti_3C_2T_x$. (f-g) TEM images of $PdPt/Ti_3C_2T_x$ and (i) HRTEM of PdPt NPs and (j) SAED of PdPt NPs The fabrication process of $PdPt/Ti_3C_2T_x$.

The high-resolution TEM image (HRTEM) image of PdPt NPs discloses the uniform and ordered lattice fringes arranged in different directions that infer the non-epitaxial growth of PdPt alloy nanoparticles as marked by the dashed lines in (Figure 1h). The lattice fringes of PdPt nanoparticles are free of defects or lattice distortions, thus implying the nonexistence of any undesired macroscopic phases. Where, the d-spacing of the PdPt lattice, ~ 0.227 nm, is assigned to the (111) facet of face-centered cubic (fcc) Pt, and implies the alloying of Pd with Pt. That is furthered seen in the selected area electron diffraction (SAED) patterns of the same nanoparticle, which reveal the typical rings related to the diffraction of (111), (200), (220), and (311) facets of the fcc Pt structure as in (Figure 1i). This indicates the formation of PdPt alloy originating from the significant synergism with an inferior lattice mismatch of nearly 0.77% between Pd and Pt. [47]

The HAADF-SEM image displays the formation of monodispersed spherical-like PdPt nanoparticles well-distributed over multilayered 2D $Ti_3C_2T_x$ nanosheets (Figure 2a). The elemental mapping analysis demonstrates a coherent distribution of Pt and Pd through Ti, C, F, and O (Figure 2b-g). The EDS scan line profile across the selected nanoparticles displays the formation of PdPt alloy (Figure 2h). The atomic percentage of Ti, C, O, F, Pt, and Pd are ~ 48.81, 29.79, 10.2, 7.1, 2.0, and 2.1 %, respectively. The abundance of surface functionalities surface O and F are crucial for possibly enhancing the hydrophilicity of PdPt/$Ti_3C_2T_x$ and inducing the chemisorption of reactants during the CO_{oxid} process. The EDX analysis also proved the presence of Ti, C, O, F, Pd, and Pt (Figure 2i) and the atomic contents similar to those determined by the element mapping analysis.

The XRD analysis of bare $Ti_3C_2T_x$ shows the main diffraction patterns assigned to (002), (004), (006), (008), (0012), and (0014) facets (Figure 3a), which all are also resolved in PdPt/$Ti_3C_2T_x$, Pd/$Ti_3C_2T_x$, and Pt/$Ti_3C_2T_x$, alongside the diffractions attributed to (111) (200), and (220) facets of fcc Pt, Pd, and PdPt, as has been commonly observed for Pt-based nanostrcutres. [23, 27, 43] The absence of any Ti-O, Pt-O, Pd-O oxides peaks imply the uniformity of thus obtained materials. The diffraction pattern assigned to (002) facet in PdPt/$Ti_3C_2T_x$ has positively shifted relative to that of Pd/$Ti_3C_2T_x$, and Pt/$Ti_3C_2T_x$, and $Ti_3C_2T_x$, duo to the insertion of PdPt in the lattice structure of $Ti_3C_2T_x$, culminating in decreasing unit cell. Furthermore, the (111) peak of PdPt nanoparticles is slightly shifted to a lower 2Θ value compared to both Pt and Pd nanoparticles, due to the alloying effect, which results in a slight upsurge in the interatomic distance of (Pt-Pt) and, consequently, the lattice contraction as revealed in the lower value of lattice parameter (a) of PdPt/$Ti_3C_2T_x$ (0.29 nm) relative to that of pure Pt/$Ti_3C_2T_x$ (0.31 nm), and Pd/$Ti_3C_2T_x$ (0.33 nm). The alloying degree of PdPt using Vegard's law is as high as 99.1 % because of the great lattice matching between Pt and Pd. [24] The crystallite size of PtPd/$Ti_3C_2T_x$ obtained from (111) peak by Scherrer's equation is around 3.5 nm, in agreement with the HRTEM. The great PtPd/$Ti_3C_2T_x$ synergism may be advantageous for providing a great adsorption site for CO and O_2 and facilitating the dissociation of O_2 and its subsequent binding with CO to form CO_2.

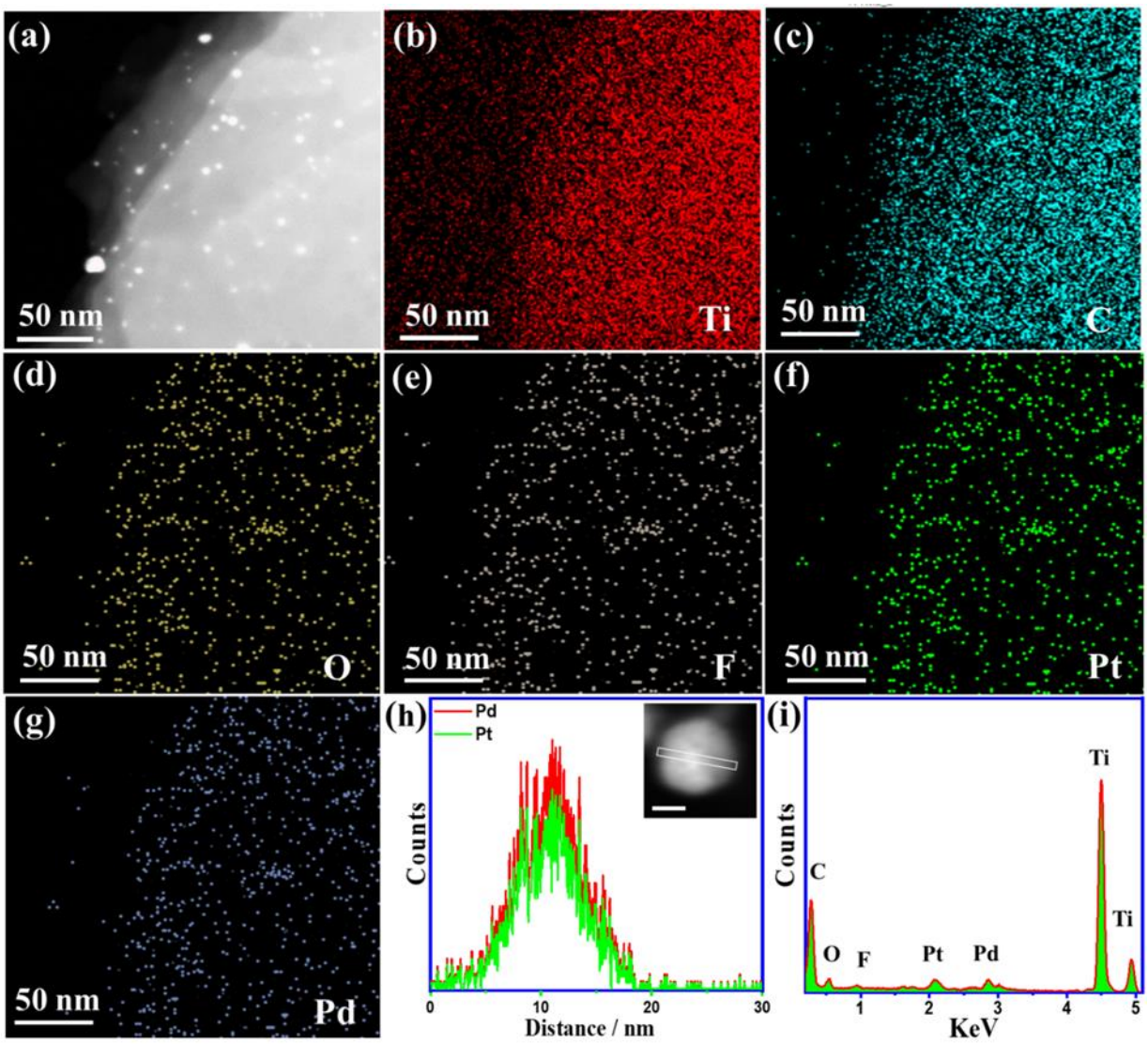


Figure 4.2 Elemental mapping of elements for PdPt/$Ti_3C_2T_x$: (a) HAADF/STEM, (b) Ti, (c) C, (d) O, (e) F, (f) Pt, (g) Pd. (h) EDS, and (i) EDX.

The electronic structure as well as the surface composition of PdPt/$Ti_3C_2T_x$, Pd/$Ti_3C_2T_x$, Pt/$Ti_3C_2T_x$, and $Ti_3C_2T_x$ were investigated by applied the XPS analysis. Where, the XPS survey spectra of $Ti_3C_2TxT_x$ showed the core-level of Ti 2p, C 1s, O 1s, and F 1s, which all were observed with additional Pd 3d/Pt 4f in PdPt/$Ti_3C_2T_x$, Pd 3d in Pd/$Ti_3C_2T_x$, and Pt 4f in Pt/$Ti_3C_2T_x$ (Figure 3b). Table S1 shows the detailed binding energies of Ti, C, F, O, d, and Pt in thus formed materials. Notably, the Ti 2p spectra in PdPt/$Ti_3C_2T_x$ were slightly negatively shifted due to the metal-free $Ti_3C_2T_x$, owing to electron transfer between PdPt nanoparticles and $Ti_3C_2T_x$, resulting in additional electronic interaction, which is important for facilitating the adsorption of CO/O_2 reactants during in CO_{oxid} reaction. The Ti 2p spectra of PdPt/$Ti_3C_2TxT_x$ show Ti-C ($2p_{3/2}$ and $2p_{½}$) as the main peak along with small shoulders of both Ti^{2+}($2p_{3/2}$ and $2p_{½}$) and Ti^{3+}($2p_{3/2}$ and $2p_{½}$)

(Figure 3c). The C 1s spectra were fitted into C-C as the core phase alongside small shoulders for both C-O, and C-F (Figure 3d), whereas fitting O 1s spectra display the main phases of O bonded to Ti (Ti-O) and OH attached to Ti (Ti-OH) with a small peak for C-O as minor phase (Figure 3e). The F 1s spectra reveal F bonded to Ti (Ti-F) and F bonded to C (C-F) (Figure 3f) this implying the abundance of surface functionalities (i.e., O, OH, and F) on PdPt/$Ti_3C_2TxT_x$. The Pd 3d spectra show the main phase of Pd^0 ($3d_{5/2}$ and $2p_{3/2}$) and the minor phase of Pd^{2+} ($3d_{5/2}$ and $2p_{3/2}$), and the inferior phase of Pd^{4+} ($3d_{5/2}$ and $2p_{3/2}$) (Figure 3g), denoting the appearance of Pd in the metallic phase, as its alloy formation with Pt. That is further observed in the resolved Pt^0 ($4f_{7/2}$ and $4f_{5/2}$) as the dominant phase with the petty phase of Pt^{2+} ($4f_{7/2}$ and $4f_{5/2}$) (Figure 3h). The XPS further indicates the formation of PdPt/$Ti_3C_2T_x$. The surface composition of PdPt/$Ti_3C_2T_x$ indicates the atomic contents for Ti, C, O, F, Pt, and Pd are ~ 49.1, 30.2, 10.1, 6.65, 1.95, and 2.0 %, respectively, which matches with the EDS and EDX.

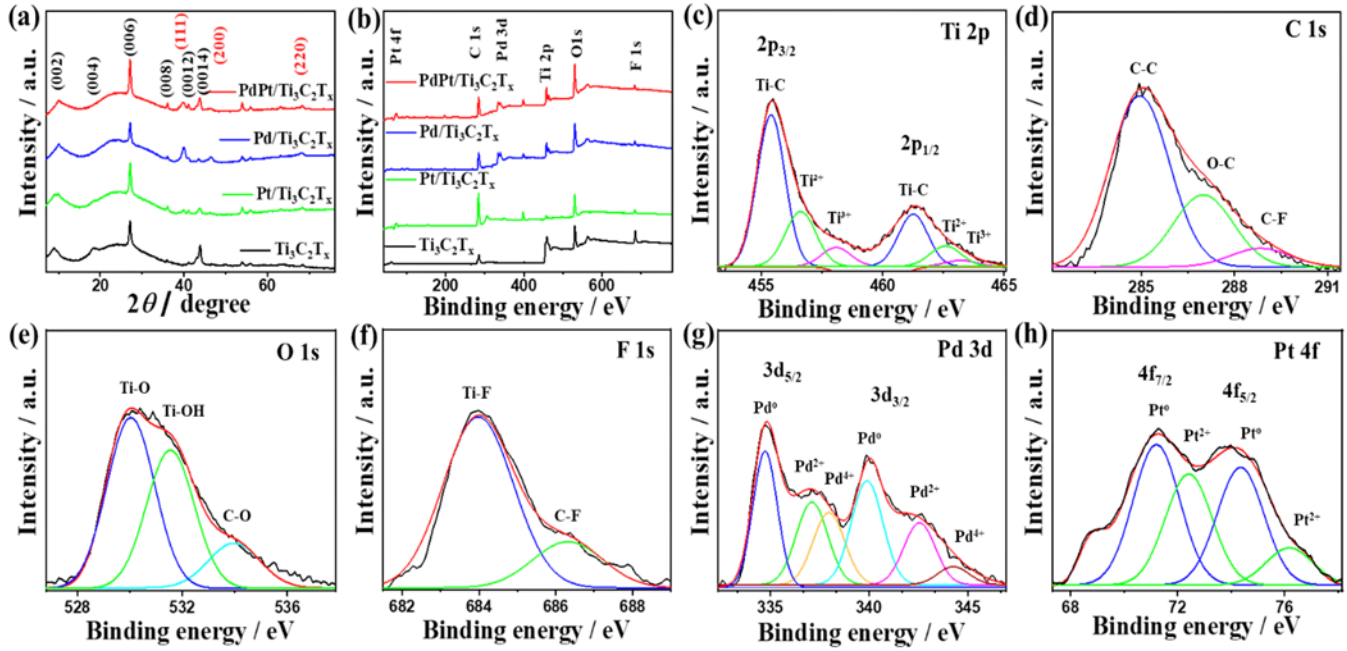


Figure 4.3 (a) XRD and (b) XPS surveys of the as-prepared catalyst. High-resolution XPS spectra of (c) Ti, (d) C, (e) O, (f) F, and (g) Pd, and (h) Pt.).

Controlled synthesis of $Ti_3C_2T_x$ with metal NPS (i.e., Co, Au, Pd, and Ag) has been reported for various catalytic reactions. However, [46, 48] the CO_{oxid} performance of $Ti_3C_2T_x$ with and without metal nanoparticles has not yet been addressed experimentally over a wide pH value. Meanwhile, the utilization of $Ti_3C_2T_x$ as a reducing agent for the rational design of bimetallic PdPt nanoparticles has not been attended yet. This contemplates us to benchmark the electrochemical CO_{oxid} reaction of PdPt/$Ti_3C_2T_x$ relative to Pd/$Ti_3C_2T_x$, Pt/$Ti_3C_2T_x$, and $Ti_3C_2T_x$ in different electrolytes.

Electrocatalytic CO oxidation activity in acidic media

Figure S1a shows the cyclic voltammogram (CVs) tested in nitrogen-saturated $HClO_4$ at rate of 50 mVs^{-1}, where pristine $Ti_3C_2T_x$ displays the quasi-rectangular feature related to the effect the pseudo-capacitance usually observed in MXenes. Meanwhile, PdPt/$Ti_3C_2T_x$ and Pd/$Ti_3C_2T_x$ display the voltammogram features of PdPt comprises the double-layered of hydrogen-adsorption/desorption ($H_{ads}/_{des}$) from -0.3V to -0.1 V and PdPt-H from 0.45V to 0.53 V. The $H_{ads}/_{des}$ of PdPt/$Ti_3C_2T_x$ was significantly greater than that of Pd/$Ti_3C_2T_x$, indicating the occurrence of more accessible active sites and higher electroactive surface area (EASA); EASA of PdPt/$Ti_3C_2T_x$ (39 m^2/g) was almost 1.34 times higher than Pd/$Ti_3C_2T_x$ (29 m^2/g). Interestingly, both PdPt/$Ti_3C_2T_x$ and Pd/$Ti_3C_2T_x$ did not show any oxide peaks for Pt-O, Pd-O, and Ti-O, indicating the stability of PdPt alloy in $Ti_3C_2T_x$ against oxidation or leaching in $HClO_4$ electrolyte. That is an interesting result, as usually Pd and Pt suffer from instability in acidic electrolytes. Notably, PdPt/$Ti_3C_2T_x$ reveals higher half-wave potentials at 0.47 V than Pd/$Ti_3C_2T_x$ (0.44 V) and Pt/$Ti_3C_2T_x$ (0.44 V), indicating the alloying effect that stabilizes Pd/Pt against oxidation as well as improving the reaction kinetics at a lower potential.

After pursing CO gas into the $HClO_4$ electrolyte, both PdPt/$Ti_3C_2T_x$ and Pd/$Ti_3C_2T_x$ reveal the typical voltammogram shape of CO_{oxid} reaction including a sharp anodic oxidation peak in the positive potential direction and a small cathodic reduction peak in the negative direction as showed by the arrows in Figure 4a. In contrast, Pt/$Ti_3C_2T_x$ and bare $Ti_3C_2T_x$ did not reveal any noticeable CO_{oxid} activity, thus implying the substantial effect of PdPt on enhancing the catalytic performance of $Ti_3C_2T_x$. This is seen in the greater CO-adsorption ability of Pd/$Ti_3C_2T_x$ (42.87 Q) than that of Pd/$Ti_3C_2T_x$ (12.44 Q) calculated by the integration of the anodic peak of current area (Table 1). Notably, the CO_{oxid} potential (E_{oxid}) of PdPt/$Ti_3C_2T_x$ (0.78 V) is lower than that of Pd/$Ti_3C_2T_x$ (0.91 V), by nearly 0.13 V. Meanwhile, the CO_{oxid} current density of PdPt/$Ti_3C_2T_x$ (0.79 mA/cm^2) is higher than Pd/$Ti_3C_2T_x$ (0.24 mA/cm^2) by 3.33 times, resulting from the alloying effect. That indicates that PdPt/$Ti_3C_2T_x$ consumes less energy to carry a higher current density than Pd/$Ti_3C_2T_x$ as further seen in the linear sweep voltammogram (LSV), which revealed the higher obtained CO_{oxid} current density at any applied potential as showed by the dashed line in (Figure 4b). This reveals the quick CO_{oxid} kinetics on PdPt/$Ti_3C_2T_x$, as shown in its lower onset potential of (0.71 V) than Pd/$Ti_3C_2T_x$ (0.84 V). The LSV of on Pt/$Ti_3C_2T_x$ and $Ti_3C_2T_x$ did not reveal any noticeable CO_{oxid} activity. The CVs measured at a different sweeping rates to get more insights onto the CO_{oxid} kinetics revealed the significant increment in the anodic oxidation peak current with increasing the sweeping rates to reach the maximum current density value of (1.57 mA/cm^2) at (200 mV/s) on PdPt/$Ti_3C_2T_x$ (Figure 4c) and (0.544 mA/cm^2) on Pd/$Ti_3C_2T_x$ (Figure 4e).

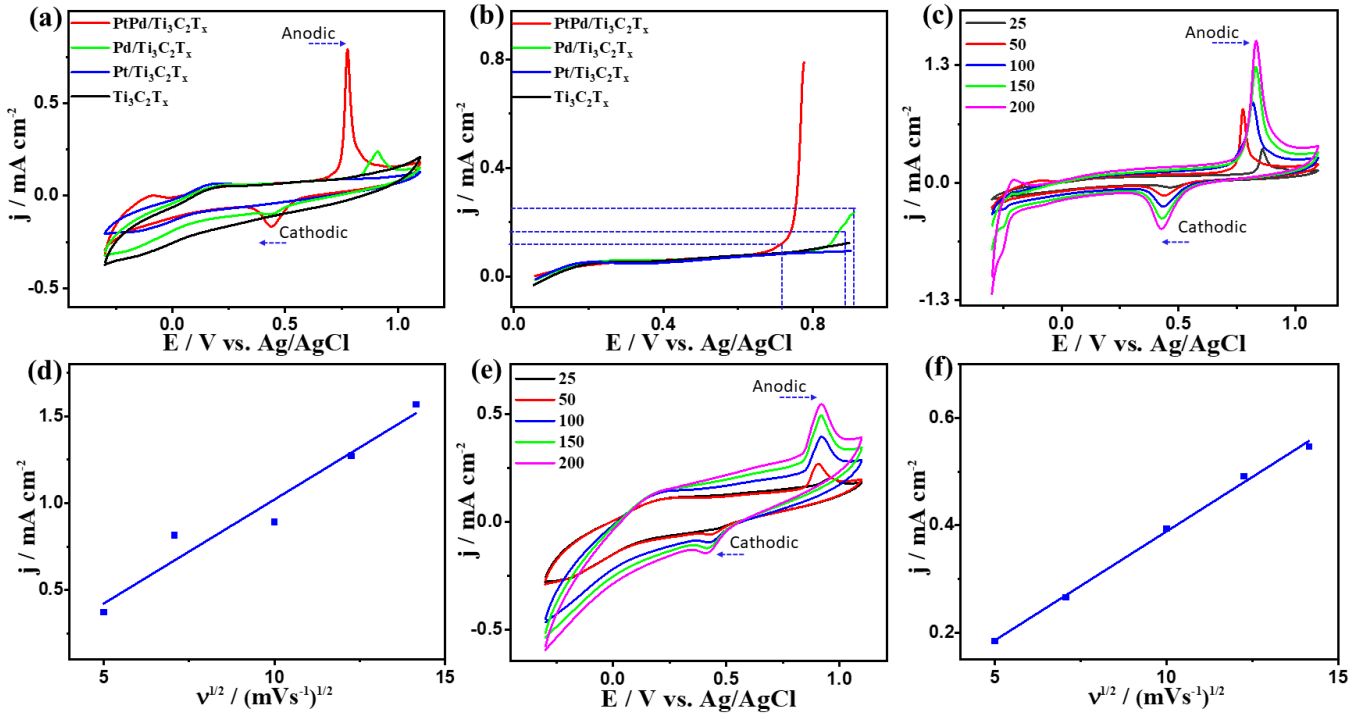


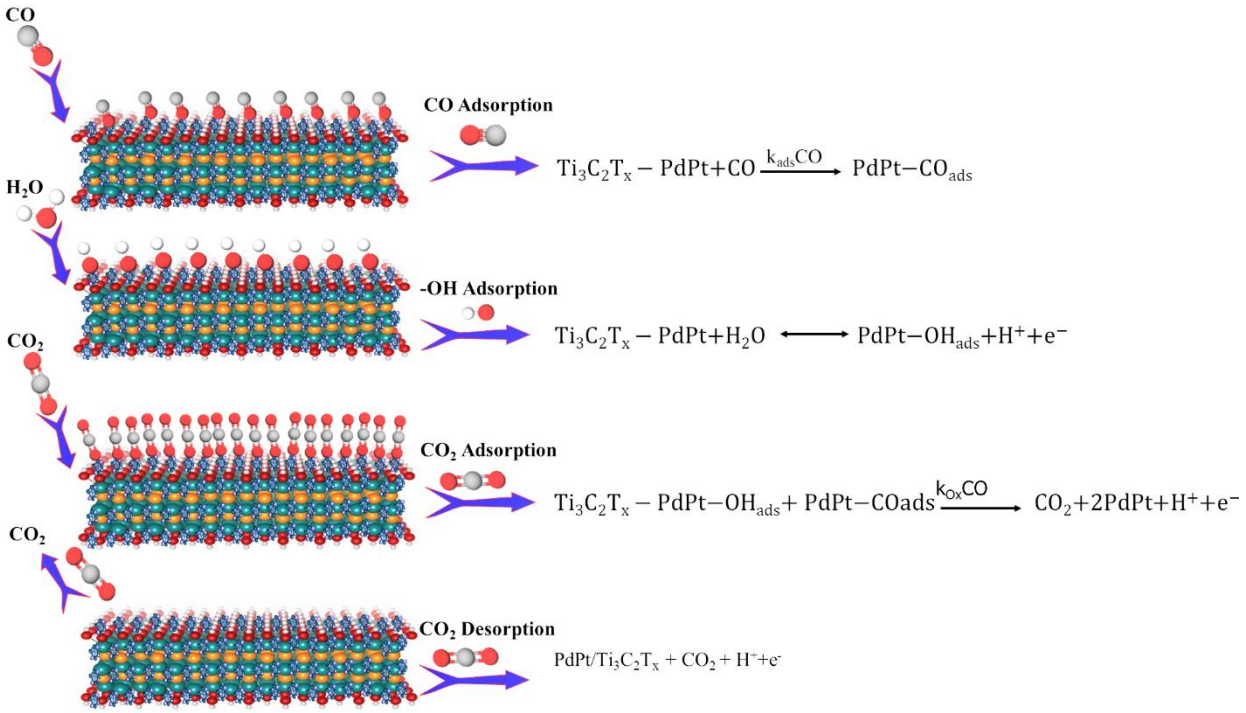
Figure 4.4 (a) CVs, and (b) LSVs of the as-prepared catalysts. CVs measured under different scan rates in saturated 0.1 M $HClO_4$ aqueous solution by CO at 25 ^oC at 50 mV s^{-1} of (c) $PdPt/Ti_3C_2T_x$ and (e) $Pd/Ti_3C_2T_x$ with the corresponding plots of the forward peaks currents against the square root of the scan rates of (d) $PdPt/Ti_3C_2T_x$ and (f) $Pd/Ti_3C_2T_x$.

Plotting the anodic peak current density against the square root of scan rate ($v^{1/2}$) using Randles-Sevcik equation, both $PdPt/Ti_3C_2T_x$ (Figure 4d) and $Pd/Ti_3C_2T_x$ (Figure 4f) display a linear relationship that serves as an indication that the CO_{oxid} on the as-prepared catalysts is a diffusion-controlled process. $PdPt/Ti_3C_2T_x$ displayed a larger slope (0.12 mV dec^{-1}) (Figure 4d) than $Pd/Ti_3C_2T_x$ (0.04 mV dec^{-1}) (Figure 4f) inferring the faster transportation kinetics on $PdPt/Ti_3C_2T_x$ surface. [14]

Catalyst Stability in acidic media

The catalyst's durability is among the most critical factors in practical electrocatalytic applications, so the durability of $PdPt/Ti_3C_2T_x$ was studied thoroughly relative to $Pd/Ti_3C_2T_x$. The chronoamperometry (CA) test shows the slower current attenuation along with greater retention of current after 2000 sec on $PdPt/Ti_3C_2T_x$ than $Pd/Ti_3C_2T_x$, demonstrating the higher CO_{oxid} durability of $PdPt/Ti_3C_2T_x$ (Figure S2a). That is additionally perceived in the CVs measured after stability on $PdPt/Ti_3C_2T_x$ that shows the CO_{oxid} voltammogram features as the initial but with a nearly 17 % decrease in the current density (Figure S2b) as has also been observed in the LSV (Figure S2c). $Pd/Ti_3C_2T_x$ reveals a significant change in the CVs voltammogram feature after

stability (Figure S2d) besides ~ 25 % loss in the current density as shown in the LSV (Figure 2e). The measurements of impedance spectroscopy (EIS) depict a lower charge transfer resistance of PdPt/$Ti_3C_2T_x$ than that of Pd/$Ti_3C_2T_x$, Pt/ $Ti_3C_2T_x$, and $Ti_3C_2T_x$ (Figure S2f), revealing the effect of PdPt on the enhancement of the charge transfer through the electrolyte-electrode interface. The image of TEM after stability tests displays the absence of any significant aggregation or degradation of PdPt from $Ti_3C_2T_x$ nanosheets, indicating greater morphological stability (Figure S3a). The EDX analysis after stability displays the stable composition without any significant changes (Figure S3b). Scheme 2 shows the proposed electrochemical CO_{oxid} mechanism in $HClO_4$ electrolyte that involves the initial CO adsorption (CO_{ads}) on the surface of PdPt/$Ti_3C_2T_x$ to form ($Ti_3C_2T_x$-PdPt-CO_{ads}). Simultaneously, the few free sites of PdPt liberated after the CO_{ads} resulting in facilitating the oxidation of hydrogen to form ($Ti_3C_2T_x$-PdPt-OH_{ads}) as the rate constant of CO



Scheme 4.2 The proposed CO_{oxid} mechanism on PdPt/$Ti_3C_2T_x$ in $HClO_4$ electrolyte

adsorption ($k_{ads}CO$)is greater than the rate constant for CO_{ads} oxidation ($k_{ox}CO$).[49] Then, the CO_{ads} is oxidized by the PdPt-OH_{ads} to form CO_2 that is subsequently desorbed from the surface of PdPt/$Ti_3C_2T_x$. The maximum hydrogen oxidation activity occurs at the similar potential where the Pt-OH oxidized the CO_{ads} , so Pd supplies abundant OH species that attach Pt atoms covered by CO_{ads} along with adsorbing less CO results in outstanding CO_{oxid} activity and stability. [49]

CO oxidation activity in neutral electrolyte

The CO_{oxid} performance of thus obtained materials was also evaluated in 0.5 M $NaHCO_3$ solution as a trial to go a step closer to the real application. The CV curves of PdPt/$Ti_3C_2T_x$ showed the typical CO_{oxid} voltammogram featured with clear anodic and cathodic peak currents, whereas PdPt/$Ti_3C_2T_x$ reveal a small CO_{oxid} activity, and Pt/$Ti_3C_2T_x$ and $Ti_3C_2T_x$ did not show any noticed activity (Figure 5a). This is seen in the greater great greater CO-adsorption ability of Pd/$Ti_3C_2T_x$ (34.6Q) than that of Pd/$Ti_3C_2T_x$ (1.97 Q) which obtained by the integration of the current area of the anodic peak (Table 1). The LSV showed a substantial enhancement in the current density of PdPt/$Ti_3C_2T_x$ than Pd/$Ti_3C_2T_x$, Pt/$Ti_3C_2T_x$, and $Ti_3C_2T_x$ at any applied potential (Figure 5b). At a 0.3 V, PdPt/$Ti_3C_2T_x$ shows a CO_{oxid} current density of (0.45 mA/cm^2), while Pd/$Ti_3C_2T_x$, Pt/$Ti_3C_2T_x$, and $Ti_3C_2T_x$ deliver only 0.152, 0.14, and 0.09 mA/cm^2, respectively. The E_{oxid} of PdPt/$Ti_3C_2T_x$ (0.3 V) is lower than Pd/$Ti_3C_2T_x$ (0.48 V) by around 0.18 V, indicating the effect of PdPt on promoting the CO_{oxid} kinetics. The CV was measured at different scan rates (25-200 mV/s) on PdPt/$Ti_3C_2T_x$ (Figure 5c) and Pd/$Ti_3C_2T_x$ (Figure 5e), which reveals the improvement in the anodic current density with increasing the scan rate, owing to the improved electron transfer by increasing the scan rate. Furthermore, the relation between the anodic peak current and $v^{1/2}$ on PdPt/$Ti_3C_2T_x$ (Figure 5d) and Pd/$Ti_3C_2T_x$ (Figure 5f) is linear, showing a larger slope of PdPt/$Ti_3C_2T_x$ (0.15 mV dec^{-1}) than Pd/$Ti_3C_2T_x$ (0.013 mV dec^{-1}), thus indicating that CO_{oxid} is a process of diffusion-controlled on both PdPt/$Ti_3C_2T_x$ and Pd/$Ti_3C_2T_x$. [14] The CA test indicated the higher stability of PdPt/$Ti_3C_2T_x$ with higher retention of current after 2000 sec than Pd/$Ti_3C_2T_x$ (Figure S4a). After the CA test, PdPt/$Ti_3C_2T_x$ (Figure S4b) and Pd/$Ti_3C_2T_x$ (Figure S4d) retained their initial voltammogram features but with less degradation in the anodic current density of PdPt/$Ti_3C_2T_x$ than $Ti_3C_2T_x$. This is also reflected in the LSV that shows the lower degradation in the current density of PdPt/$Ti_3C_2T_x$ (14 %) (Figure S4c) than $Ti_3C_2T_x$ (25%), along with a slight increase in the E_{oxid} (Figure S4e). The EIS measurements reveal the decrease in the charge transfer resistance of PdPt/$Ti_3C_2T_x$ relative to Pd/$Ti_3C_2T_x$, Pt/$Ti_3C_2T_x$, and $Ti_3C_2T_x$ (Figure S4f), owing to the fast charge transfer through the electrolyte/electrode interface in case of PdPt-bearing catalyst.

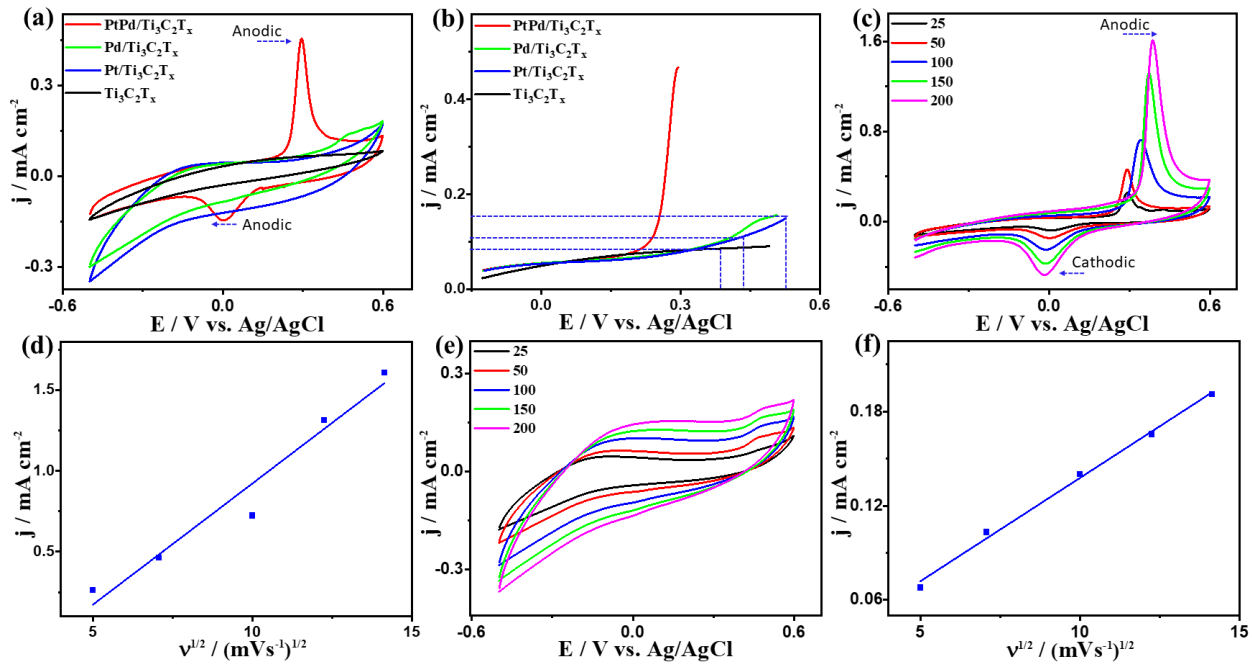


Figure 4.5 (a) CVs and (b) LSV of the as-prepared materials. CVs measured under different scan rates in saturated 0.5 M $NaHCO_3$ aqueous solution by CO at 25 ^oC at 50 mVs^{-1} of (c) of $PdPt/Ti_3C_2T_x$ (e) $Pd/Ti_3C_2T_x$ with the corresponding plots of the forward peaks currents against the square root of the scan rates (d) of $PdPt/Ti_3C_2T_x$, and (f) of $Pd/Ti_3C_2T_x$.

Table 4.1 The CO adsorption capacity on thus obtained materials in different electrolytes calculated by the integration of the anodic peak current area.

	0.1 M HClO4 (C, Q)	0.5 M Na2HCO3 (C, Q)	M KOH (C, Q)
PdPt/Ti3C2Tx	42.87	34.6	7.3
Ti3C2Tx	12.44	1.97	3.1

CO oxidation activity in alkaline electrolyte

The CO_{oxid} performance of $PdPt/Ti_3C_2T_x$ was additionally measured in KOH solution relative to $Pd/Ti_3C_2T_x$, $Pt/Ti_3C_2T_x$, and $Ti_3C_2T_x$. Both, the $PdPt/Ti_3C_2T_x$ and $Pd/Ti_3C_2T_x$ show a CO_{oxid} voltammogram, but with a noticeably higher activity of $PdPt/Ti_3C_2T_x$ than $Pd/Ti_3C_2T_x$, while $Ti_3C_2T_x$ did not show any activity (Figure 6a). This is seen in the greater CO-adsorption ability of $Pd/Ti_3C_2T_x$ (7.3 Q) than that of $Pd/Ti_3C_2T_x$ (3.1 Q) which calculated by the integration of the anodic peak current area (Table 1). The E_{oxid} of $PdPt/Ti_3C_2T_x$ (-0.15 V) was substantially negatively shifted than $Pd/Ti_3C_2T_x$ (0.1 V). The LSV showed the greater CO_{oxid} current density of

PdPt/$Ti_3C_2T_x$ than Pd/$Ti_3C_2T_x$ at any applied potential point (Figure 6b); at -0.15 V, the current density of PdPt/$Ti_3C_2T_x$ (0.21 mA cm^{-2}) at (-0.15 V) was 4 times greater than Pd/$Ti_3C_2T_x$ (0.05 mA cm^{-2}). The anodic peak current of PdPt/$Ti_3C_2T_x$ (Figure 6c) and Pd/$Ti_3C_2T_x$ (Figure 6e) increased from (0.14 to 0.64 mA/cm^2) and (0.05 to 0.3 mA/cm^2), respectively by increase in the scan rate from 25 to 200 mV/s. Furthermore, the CO_{oxid} process on PdPt/$Ti_3C_2T_x$ (Figure 6d) and Pd/$Ti_3C_2T_x$ (Figure 6f) is diffusion-controlled as shown in the linear relationship between the anodic current and $v^{1/2}$ presented a larger slope of PdPt/$Ti_3C_2T_x$ (0.056 mV dec^{-1}) than Pd/$Ti_3C_2T_x$ (0.028 mV dec^{-1}). The CA test displays the greater stability of PdPt/$Ti_3C_2T_x$ compared to Pd/$Ti_3C_2T_x$ over 2000 sec (Figure S5a). The CV of PdPt/$Ti_3C_2T_x$ (Figure S5b) and Pd/$Ti_3C_2T_x$ (Figure S5d) reserved the initial voltammogram characteristics after the CA test. The LSV indicate the lower degradation in the current density of PdPt/$Ti_3C_2T_x$ by (10 %) (Figure S5c) than Pd/$Ti_3C_2T_x$ (70 %) (Figure S5e) after CA test. The EIS measurements display the significant decrease in the charge transfer resistance of PdPt/$Ti_3C_2T_x$ compared to Pd/$Ti_3C_2T_x$, Pt/$Ti_3C_2T_x$, and $Ti_3C_2T_x$ (Figure S5f), owing to the facile charge transfer across the electrolyte-electrode interface in the case of the PdPt catalyst. [14] These results demonstrate the noticeable effect of

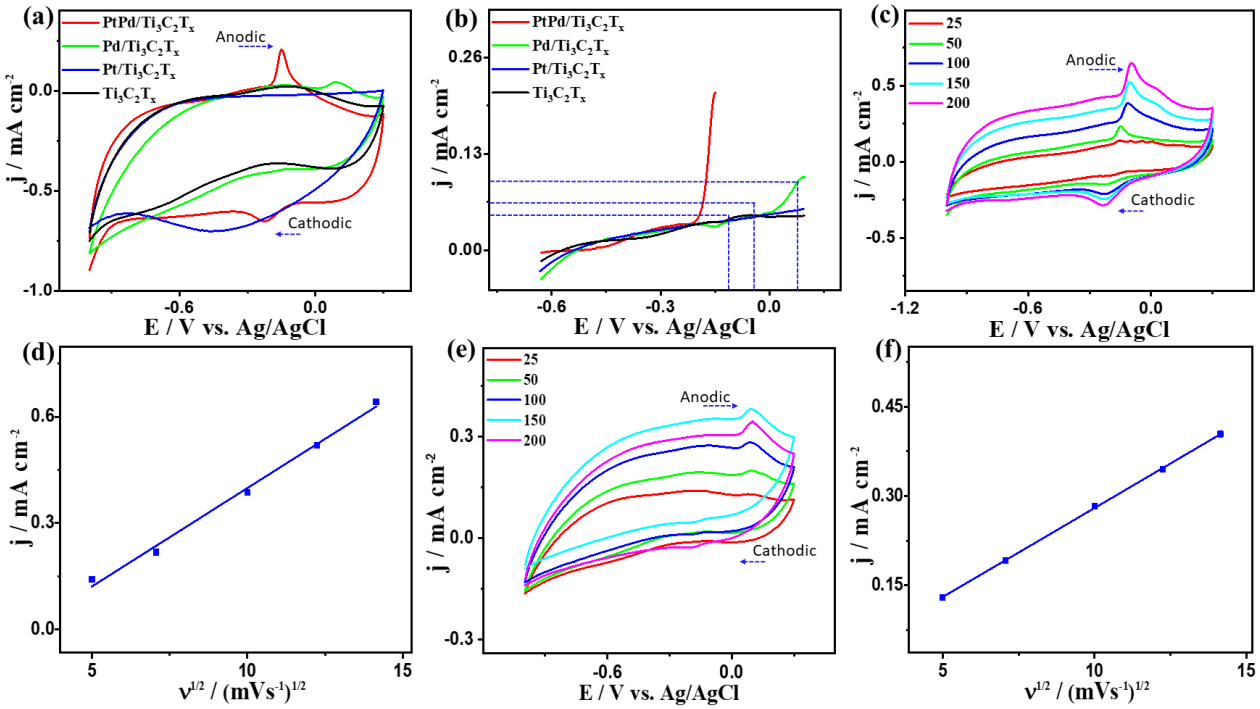


Figure 4.6 (a) CVs and (b) LSV of the as-prepared catalyst. CVs measured under different scan rates in saturated 0.1 M KOH aqueous solution by CO at 25 ^oC at 50 mV s^{-1} of (c) of PdPt/$Ti_3C_2T_x$ (e) of Pd/$Ti_3C_2T_x$ with the corresponding plots of the forward peaks currents vs the square root of the scan rates of (d) PdPt/$Ti_3C_2T_x$, and (f) Pd/$Ti_3C_2T_x$.

PdPt nanoparticles on the enhancement of the $_{COoxid}$ performance of $Ti_3C_2T_x$ in different electrolytes over a wide pH ranges. That is plausibly originating from the electronic effect and synergism of PdPt alloy that enhances the adsorption of both (CO and O_2) molecules and facilitates the dissociation of O_2 to allow the formation of CO_2 along with desorption of intermediates or CO_2 products. Notably, the CO_{oxid} activity of PdPt/$Ti_3C_2T_x$ in $HClO_4$ is greater than that observed in Na_2HCO_3, and KOH under the same reaction conditions. That is probably ascribed to large CO adsorption on PdPt $Ti_3C_2T_x$ in $HClO_4$ than in $NaHCO_3$ and KOH; integration of the anodic peak current area on PdPt $Ti_3C_2T_x$ in $HClO_4$ (3.2 Q) is higher than that in $NaHCO_3$ (1.2 Q) and KOH (0.3 Q).

Conclusions

In brief, we have rationally designed and synthesized PdPt nanoparticles (15 nm) – adorned on $Ti_3C_2T_x$ (T_X=OH, O, and F) MXene exfoliated nanosheets (PdPt/$Ti_3C_2T_x$) for the electrochemical CO_{oxid} in various electrolytes over wide pH values that is unprecedented so far. The preparative process includes the HF etching for Ti_3AlC_2 followed by intercalation by DMSO and exfoliation by sonication to give Ti_3C_2Tx that is subsequently deployed as a reducing agent that work as in situ reductions of Pd and Pt precursors to form PdPt nanoparticles. The synthetic mechanism is attributed to the formation of highly reactive single vacancies of Ti atoms or clusters of vacancy and Ti-deficit defects upon HF etching that can reduce Pd and Pt precursors and provide adsorption sites for accommodating the ensuing PdPt nanoparticles at RT. The electrochemical CO_{oxid} activity of PdPt/$Ti_3C_2T_x$ was substantially superior to Pd/$Ti_3C_2T_x$, Pt/$Ti_3C_2T_x$, and metal-free $Ti_3C_2T_x$ under all tested pH values, owing to the electronic effect and synergism displayed by the PdPt nanoparticles. The CO_{oxid} performance activity of PdPt/$Ti_3C_2T_x$ in $HClO_4$ is greater than that in $NaHCO_3$, and KOH below the same reaction conditions, because of the superior CO adsorption capacity in $HClO_4$, which is greater than that in $NaHCO_3$ and KOH. This article may stimulate further investigations and open up new avenues to utilize $Ti_3C_2T_x$ in the synthesis of various bi-metallic Pt-based alloys for CO_{oxid} reaction.

Experimental methods

Chemicals and materials

Sodium tetrachloropalladate (II)[(Na_2PdCl_4), 99%], potassium platinum(II) chloride [(K_2PtCl_4), 98 %] acetone (CH_3COCH_3, ≥ 99.9 %) hydrofluoric acid [(HF) 48 Wt. %], and dimethyl sulfoxide anhydrous [(DMSO), ≥ 99.9 %] were purchased from Sigma-Aldrich, Chemie GmbH in Munich, Germany. Aluminum titanium carbide powder [(Ti_3AlC_2, 99.9 %, 40 μm particle size] was purchased from Carbon-Ukraine Ltd

(Kiev, Ukraine).

Synthesis of $Ti_3C_2T_x$ nanosheets

2D $Ti_3C_2T_x$ nanosheets were produced by the traditional HF etching method as reported previously. [43] Briefly, Ti_3AlC_2 (4 g) powder was dispersed in the aqueous solution of HF (80 mL, 50 Wt. %) under magnetic stirring at RT for 1day after that a series of centrifugation cycles at 3500 rpm and washing with double deionized water DI-H_2O until the pH of supernatant be ≥ 5. [43] The wet precipitate was taken in DMSO (60 mL) under mechanical stirring for 24 h at RE, followed by centrifugation at 3500 rpm for 4 min and washing with D-H_2O 4 times. The resultant solution was purged with Ar gas and sonicated (100 W, 40 Hz) for 6h, under ice-bath, and then centrifuged at 4000 rpm for 1 hr. Finally, $Ti_3C_2T_x$ supernatant was dried under vacuum at 50 ^oC for 24 h. The concentration of $Ti_3C_2T_x$ in the obtained solution was nearly 5 mg/mL.

Synthesis of PdPt/$Ti_3C_2T_x$

PdPt/$Ti_3C_2T_x$ was prepared by dispersion of the as-formed $Ti_3C_2T_x$ (4 mL) in water (100 mL) solution under magnetic stirring at 25 ^oC till the solution color turned to pale gray. Meanwhile, an aqueous solution (1 mL) comprising Na_2PdCl_4 (20 mM) and K_2PtCl_4 (20 mM) was added dropwise into $Ti_3C_2T_x$ under sonication (100 W, 40 Hz) for 15 min at 25 ^oC. After sonication, acetone solution (200 mL) was added, and then the solution was kept for 2 h and then centrifuged 4 times at 8000 rpm and washed with acetone. [48] Finally, the precipitate was dried at 60 ^oC for 4 h under vacuum. The same method was used for the preparation of Pd/$Ti_3C_2T_x$ and Pt/$Ti_3C_2T_x$ but using individual 0.5 mL Na_2PdCl_4 (20 mM) and 0.5 mL K_2PtCl_4 (20 mM), respectively.

Materials characterization

The scanning electron microscope ((SEM) was conducted on (SEM, Hitachi S-4800, Hitachi, Tokyo, Japan) equipped with Energy Dispersive X-Ray Analyzer (EDX). The transmission electron microscope (TEM) was performed on (TEM, TecnaiG220, FEI, Hillsboro, OR, USA) equipped with high-angle annular dark-field scanning transmission electron microscopy (HAADF-SEM), and energy dispersive spectrometer (EDS) were used for imaging and compositional analysis. The X-ray photoelectron spectroscopy (XPS) spectra were recorded on a Kratos Axis (Ultra DLD XPS Kratos, Manchester, UK). The X-ray diffraction patterns (XRD) were measured on an X-ray diffractometer (X'Pert-Pro MPD, PANalytical Co., Almelo, Netherlands).

Supporting information

Electrochemical CO oxidation reaction

The catalyst inks were prepared via mixing 1 mg of each catalyst with Nafion^R solution (10 µL,

0.5 Wt %) in deionized H_2O (1.5 mL) with ethanol (0.5 mL) (absolute grade, Sigma Aldrich Chemicals) (3/1 v/v ratio) under sonication in the ice bath until a homogeneous solution was obtained. The glassy carbon electrode (GCE) (⌀15 mm x 1 mm) was used as a WE, that was initially polished using (1 µm) and then (0.3 µm)of Al_2O_3 slurry and was rinsed in double deionized water (DDI-H_2O) for 30 sec under ultrasonic treatment atRTafter each polishing step. The inks were deposited volumetrically over the polished (GC) electrodes with a 0.1 mg/cm^{-2} loading amount followed by drying in oven at 55 ^oC for 1 h. The electrocatalytic CO_{oxid} performances were investigated using cyclic voltammogram (CVs), linear sweep voltammogram (LSV), impedance spectroscopy (EIS), and chronoamperometry (CA) tests on Gamry potentiostat (Reference 3000, Gamry Co., Warminster, PA, USA) using the three-electrode cell of Pt wire (counter electrode), leak-free Ag/AgCl (KCl, 3 M)) (reference electrode), and GCE (WE). The PdPt, Pd, and Pt concentration measurements were measured by inductively coupled plasma optical emission spectrometry (ICP-OES, Agilent 5800). The electrochemical active surface area (EASA) was calculated by this equation: ECSA= QH/m× 424; where Q_H is the charge for H_{upd} adsorption obtained after the double layer correction area, m is the loading amount of PdPt or Pd on the GCE, and 424 µC cm^{-2} is the charge required for monolayer adsorption of hydrogen onto PdPt surface.

Table 4.S1 Detailed XPS binding energies of Ti, C, F, O, d, and Pt in as-synthesized PdPt/$Ti_3C_2T_x$

elements	Core level	Binding energy (ev)	elements	Core level	Binding energy (ev)
Ti	Ti-C $2P_{3/2}$	455.4	F	Ti-F	683.97
	Ti^{2+} $2P_{3/2}$	456.6		C-F	686.29
	Ti^{3+} $2P_{3/2}$	458	Pd	Pd^0 $3d_{5/2}$	334.73
	Ti-C $2P_{1/2}$	461.24		Pd^{+2} $3d_{5/2}$	337.09
	Ti^{2+} $2P_{1/2}$	462.58		Pd^{+4} $3d_{5/2}$	337.96
	Ti^{3+} $2P_{1/2}$	463.24		Pd^0 $3d_{3/2}$	339.91
C	C-C	284.94		Pd^{+2} $3d_{3/2}$	342.55
	C-O	287		Pd^{+4} $3d_{3/2}$	344.33
	C-F	288.93	Pt	Pt^0 $4f_{7/2}$	71.2
O	Ti-O	530.03		Pt^{+2} $4f_{7/2}$	72.42
	Ti-OH	532.55		Pt^0 $4f_{5/2}$	74.35

	O-C	533.92		Pt^{+2} $4f_{5/2}$	76.14

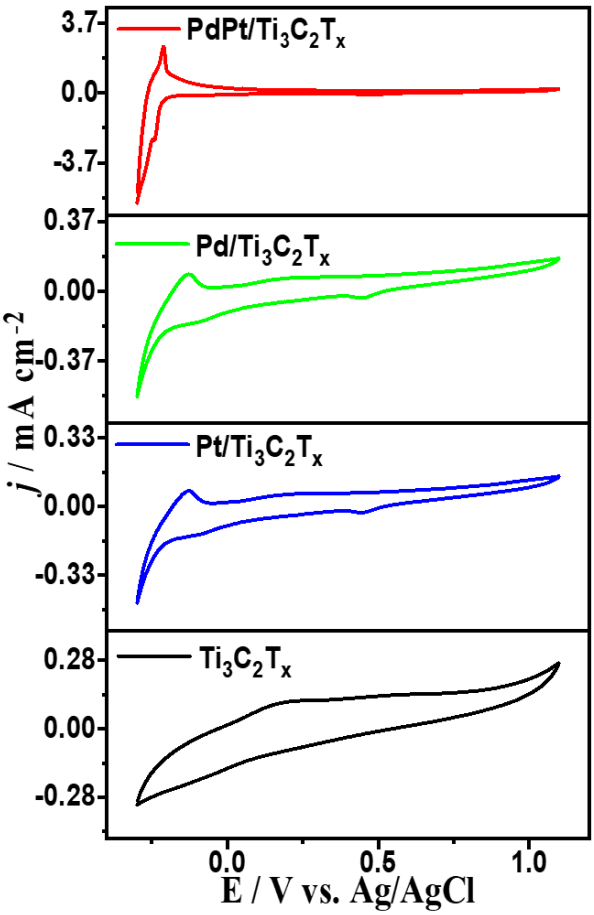


Figure 4. S1 cyclic voltammetry measured in N_2 saturated 0.1 M $HClO_4$ at 50 mV s^{-1} of the as-prepared catalyst.

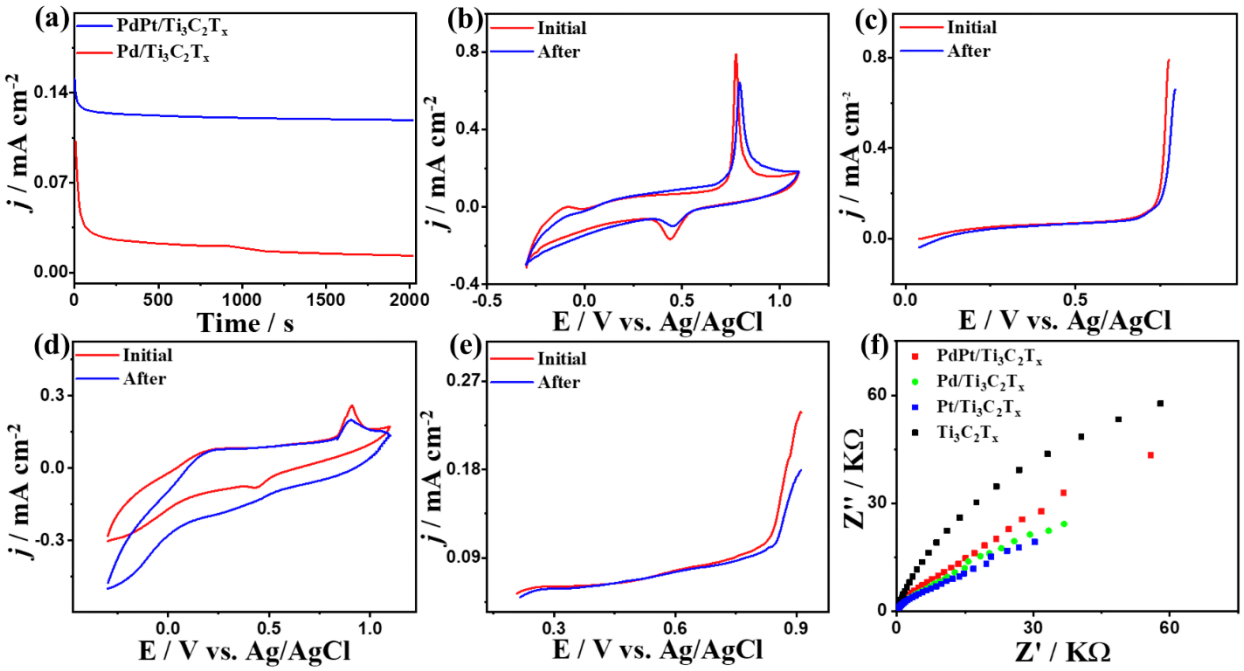


Figure 4.S2 (a) The I-T tests measured for 2000 s in CO-saturated 0.1 M $HClO_4$ of $PdPt/Ti_3C_2T_x$ at 0.71 V and $Pd/Ti_3C_2T_x$ at 0.84V. CVs before and after stability tests (b) of $PdPt/Ti_3C_2T_x$, and (d) of $Pd/Ti_3C_2T_x$. LSV before and after stability tests (c) of $PdPt/Ti_3C_2T_x$, and (e) of $Pd/Ti_3C_2T_x$ tested in 0.1 M $HClO_4$ aqueous solution saturated by CO at 50 mV s^{-1} and (f) EIS of the as-prepared catalyst (frequency, 100 kHz - 5 Hz) of 0.78V in 0.1 M $HClO_4$.

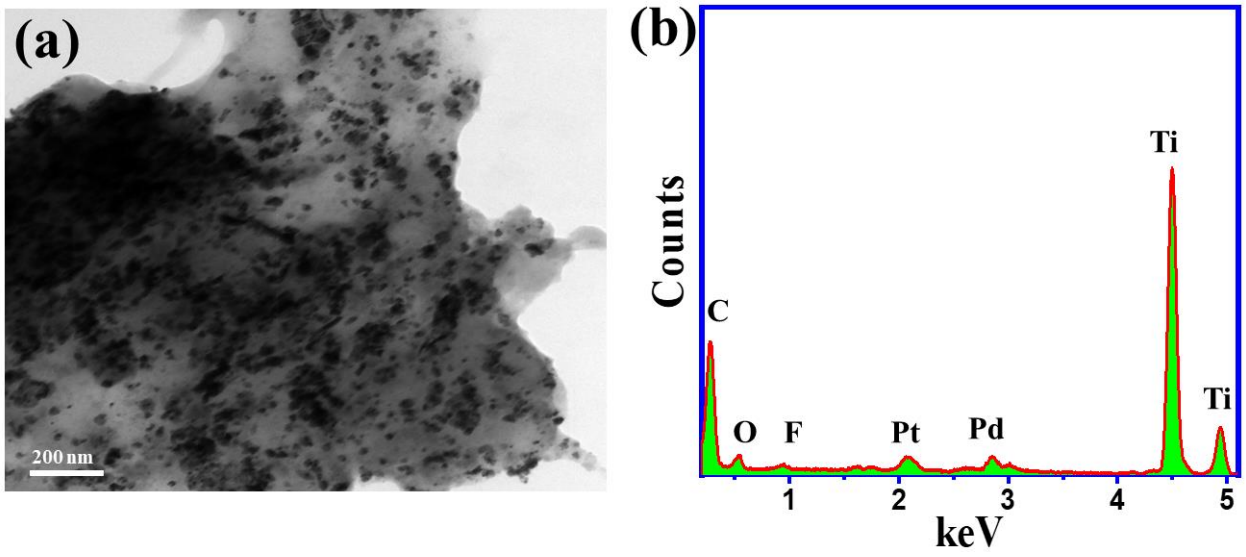


Figure 4.S3 (a)TEM, and (b) EDX of PdPt/ $Ti_3C_2T_x$ after CO_{oxid} stability test in 0.1 M $HClO_4$.

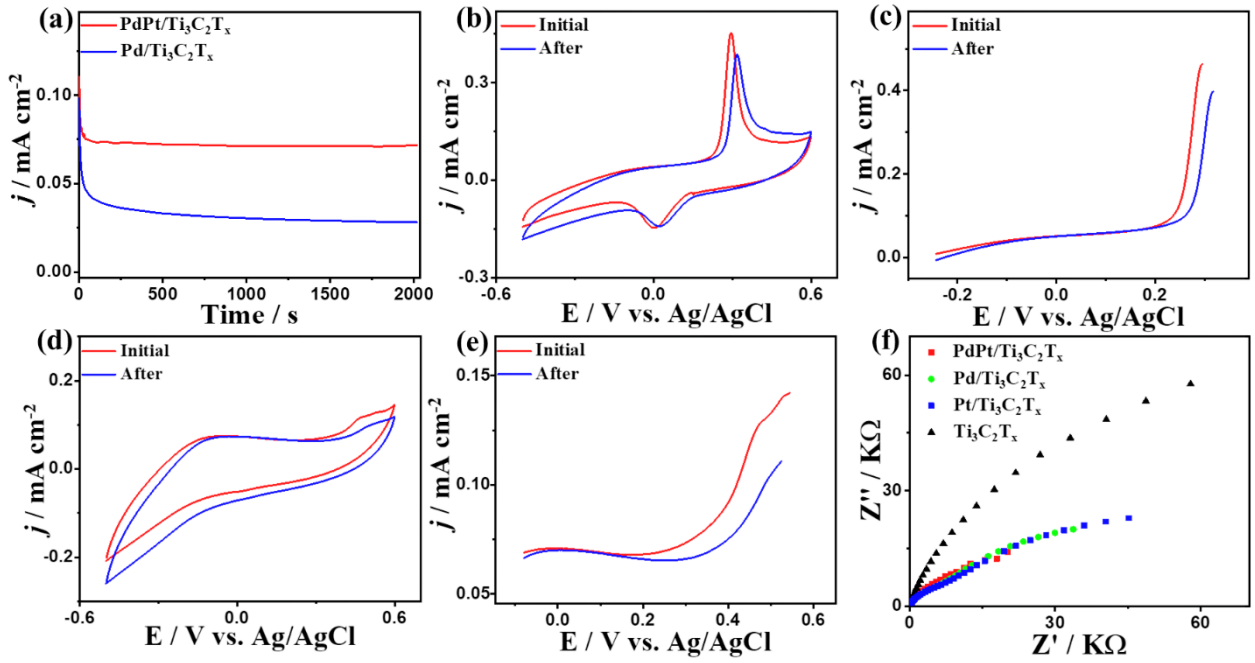


Figure 4.S4 (a) The I-T tests recorded for 2000 s in CO-saturated 0.5 M $NaHCO_3$ of PdPt/ $Ti_3C_2T_x$ at 0.23 V and Pd/ $Ti_3C_2T_x$ at 0.39V. CVs before and after stability tests (b) of PdPt/ $Ti_3C_2T_x$, and (d) of Pd/$Ti_3C_2T_x$. LSV before and after stability tests (c) of PdPt/ $Ti_3C_2T_x$, and (e) of Pd/ $Ti_3C_2T_x$ tested in 0.5 M $NaHCO_3$ aqueous solution saturated by CO of at 50 mV s^{-1} and (f)) EIS of the as-prepared catalyst (frequency, 100 kHz - 5 Hz) of 0.3V in 0.5 M $NaHCO_3$.

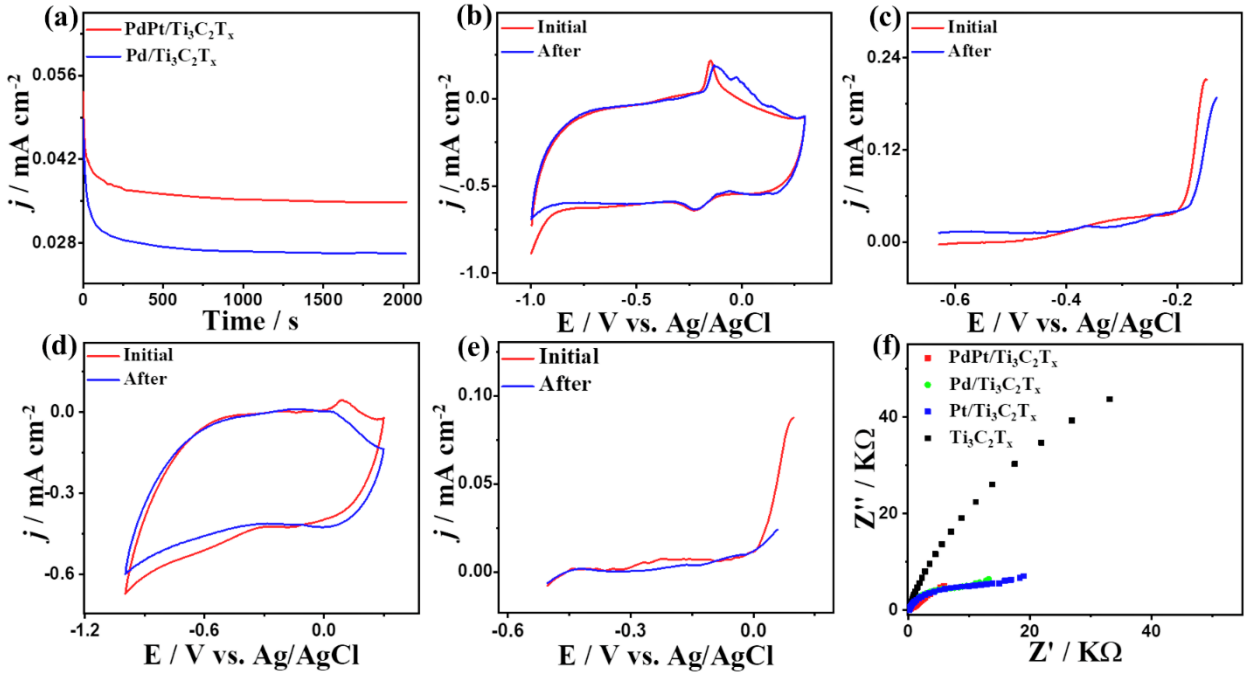


Figure 4.S5 (a) The I-T tests measured for 2000 s in CO-saturated 0.1 M KOH of PdPt/$Ti_3C_2T_x$ at -0.19 V and Pd/$Ti_3C_2T_x$ at 0.02 V. CVs before and after stability tests (b) of PdPt/$Ti_3C_2T_x$, and

(d) of Pd/$Ti_3C_2T_x$. LSV before and after stability tests (c) of PdPt/ $Ti_3C_2T_x$, and (e) of Pd/T $Ti_3C_2T_x$ tested in 0.1 M KOH aqueous solution saturated by CO at 50 mV s^{-1} and (f) EIS of the as-prepared catalyst (frequency, 100 kHz - 5 Hz) of 0.15V in 0.1 M KOH.

References

1. Tanaka, S., et al., *Gold nanoparticles supported on mesoporous iron oxide for enhanced CO oxidation reaction.* 2018. **10**(10): p. 4779-4785.
2. Lu, Q., et al., *Engineering graphitic carbon nitride (gC 3 N 4) for catalytic reduction of CO 2 to fuels and chemicals: strategy and mechanism.* 2021. **23**(15): p. 5394-5428.
3. Wang, K., et al., *Insights into the development of Cu-based photocathodes for carbon dioxide (CO 2) conversion.* 2021. **23**(9): p. 3207-3240.
4. Huang, S., et al., *Green catalysis for selective CO oxidation in hydrogen for fuel cell.* 2009. **2**(10): p. 1060-1068.
5. Finke, C.E., et al., *Economically advantageous pathways for reducing greenhouse gas emissions from industrial hydrogen under common, current economic conditions.* 2021. **14**(3): p. 1517-1529.
6. Liu, X., et al., *Tuning the structure of bifunctional Pt/SmMn 2 O 5 interfaces for promoted low-temperature CO oxidation activity.* 2019. **11**(17): p. 8150-8159.
7. Guo, Z., et al., *Recent advances in heterogeneous selective oxidation catalysis for sustainable chemistry.* 2014. **43**(10): p. 3480-3524.
8. Carnis, J., et al., *Twin boundary migration in an individual platinum nanocrystal during catalytic CO oxidation.* 2021. **12**(1): p. 1-10.
9. Liu, L. and A.J.C.r. Corma, *Metal catalysts for heterogeneous catalysis: from single atoms to nanoclusters and nanoparticles.* 2018. **118**(10): p. 4981-5079.
10. Xu, H., et al., *Identification of activity trends for CO oxidationon supported transition-metal single-atom catalysts.* 2017. **7**(24): p. 5860-5871.
11. Elias, J.S., et al., *In situ spectroscopy and mechanistic insights into CO oxidationon transition-metal-substituted ceria nanoparticles.* 2017. **7**(10): p. 6843-6857.
12. Davo-Quinonero, A., et al., *Mineral Manganese Oxides as Oxidation Catalysts: Capabilities in the CO-PROX Reaction.* 2021. **9**(18): p. 6329-6336.
13. Eid, K., et al., *Rational synthesis of porous graphitic-like carbon nitride nanotubes codoped with Au and Pd as an efficient catalyst for carbon monoxide oxidation.* 2019. **35**(9): p. 3421-3431.
14. Eid, K., M.H. Sliem, and A.M.J.N. Abdullah, *Unraveling template-free fabrication of carbon nitride nanorods codoped with Pt and Pd for efficient electrochemical and photoelectrochemical carbon monoxide oxidation at RE.* 2019. **11**(24): p. 11755-11764.
15. Wang, C., et al., *Enhanced CO oxidation on CeO 2/Co 3 O 4 nanojunctions derived from annealing of metal organic frameworks.* 2016. **8**(47): p. 19761-19768.
16. Zhang, X., et al., *A Ti-anchored Ti 2 CO 2 monolayer (MXene) as a single-atom catalyst for CO oxidation.* 2016. **4**(13): p. 4871-4876.
17. van Spronsen, M.A., J.W. Frenken, and I.M.J.C.S.R. Groot, *Surface science under reaction conditions: CO oxidation on Pt and Pd model catalysts.* 2017. **46**(14): p. 4347-4374.
18. Zhang, B., et al., *Construction of graphene-wrapped Pd/TiO2 hollow spheres with enhanced anti-CO poisoning capability toward photoassisted methanol oxidation reaction.* 2021. **9**(3): p. 1352-1360.
19. Muravev, V., et al., *Interface dynamics of Pd–CeO2 single-atom catalysts during CO oxidation.* 2021. **4**(6): p. 469-478.
20. Li, X. and X.J.C.C. Hong, *PdPt@ Au core@ shell nanoparticles: alloyed-core manipulation of CO electrocatalytic oxidation properties.* 2016. **83**: p. 70-73.
21. Rosseler, O., et al., *Structural and electronic effects in bimetallic PdPt nanoparticles on TiO2 for improved photocatalytic oxidation of CO in the presence of humidity.* 2015. **166**: p. 381-392.

22. Lv, H., et al., *One-pot aqueous synthesis of ultrathin trimetallic PdPtCu nanosheets for the electrooxidation of alcohols.* 2019. **21**(9): p. 2367-2374.
23. Eid, K., et al., *Trimetallic PtPdRu dendritic nanocages with three-dimensional electrocatalytic surfaces.* 2015. **119**(34): p. 19947-19953.
24. Eid, K., et al., *Rational design of porous binary Pt-based nanodendrites as efficient catalysts for direct glucose fuel cells over a wide pH range.* 2017. **7**(13): p. 2819-2827.
25. Hong, W., et al., *Bimetallic PdPt nanowire networks with enhanced electrocatalytic activity for ethylene glycol and glycerol oxidation.* 2015. **8**(10): p. 2910-2915.
26. Zhang, Y., et al., *One-step synthesis of the PdPt bimetallic nanodendrites with controllable composition for methanol oxidation reaction.* 2018. **61**(5): p. 697-706.
27. Eid, K., et al., *Rational one-step synthesis of porous PtPdRu nanodendrites for ethanol oxidation reaction with a superior tolerance for CO-poisoning.* 2017. **9**(47): p. 18881-18889.
28. Jang, J.-H., et al., *Emerging carbon shell-encapsulated metal nanocatalysts for fuel cells and water electrolysis.* 2021. **13**(36): p. 15116-15141.
29. Kim, Y., et al., *Star-shaped Pd@ Pt core–shell catalysts supported on reduced graphene oxide with superior electrocatalytic performance.* 2014. **2**(19): p. 6976-6986.
30. Chen, Z., et al., *Grafted MXene/polymer electrolyte for high performance solid zinc batteries with enhanced shelf life at low/high temperatures.* 2021. **14**(6): p. 3492-3501.
31. Choi, H., et al., *Influence of lattice oxygen on the catalytic activity of blue titania supported Pt catalyst for CO oxidation.* 2021. **11**(5): p. 1698-1708.
32. Zhang, Z., et al., *An overview of metal oxide materials as electrocatalysts and supports for polymer electrolyte fuel cells.* 2014. **7**(8): p. 2535-2558.
33. Li, X., et al., *Applications of MXene (Ti 3 C 2 T x) in photocatalysis: A review.* 2021. **2**(5): p. 1570-1594.
34. Tahini, H.A., X. Tan, and S.C.J.C. Smith, *Facile CO oxidation on Oxygen-functionalized MXenes via the Mars-van Krevelen Mechanism.* 2020. **12**(4): p. 1007-1012.
35. You, Z., et al., *State-of-the-art recent progress in MXene-based photocatalysts: a comprehensive review.* 2021. **13**(21): p. 9463-9504.
36. Zhao, R., et al., *Self-assembled Ti 3 C 2 MXene and N-rich porous carbon hybrids as superior anodes for high-performance potassium-ion batteries.* 2020. **13**(1): p. 246-257.
37. Gao, Q., et al., *Tracking ion intercalation into layered Ti 3 C 2 MXene films across length scales.* 2020. **13**(8): p. 2549-2558.
38. Peng, Y.-Y., et al., *All-MXene (2D titanium carbide) solid-state microsupercapacitors for on-chip energy storage.* 2016. **9**(9): p. 2847-2854.
39. Zhao, D., et al., *Alkali-induced 3D crinkled porous Ti 3 C 2 MXene architectures coupled with NiCoP bimetallic phosphide nanoparticles as anodes for high-performance sodium-ion batteries.* 2019. **12**(8): p. 2422-2432.
40. Zhang, Y., et al., *Recent progress of MXenes as the support of catalysts for the CO oxidation and oxygen reduction reaction.* 2020. **31**(4): p. 931-936.
41. Cheng, C., et al., *Identification of High-Performance Single-Atom Mxenes Catalysts for Low-Temperature CO oxidation.* 2019. **2**(8): p. 1900006.
42. Morales-Garcia, A., F. Calle-Vallejo, and F.J.A.C. Illas, *MXenes: new horizons in catalysis.* 2020. **10**(22): p. 13487-13503.
43. Alhabeb, M., et al., *Guidelines for synthesis and processing of 2-D titanium carbide (Ti3C2T x MXene).* 2017. **29**(18): p. 7633-7644.
44. Talib, S.H., et al., *Non-noble metal single-atom catalyst of Co1/MXene (Mo2CS2) for CO oxidation.* 2021. **64**(3): p. 651-663.
45. Cheng, C., et al., *Cu3-cluster-doped monolayer Mo2CO2 (MXene) as an electron reservoir for catalyzing a CO oxidation reaction.* 2018. **10**(38): p. 32903-32912.
46. Salah, B., et al., *Titanium Carbide (Ti3C2Tx) MXene Ornamented with Palladium Nanoparticles for Electrochemical CO oxidation.* 2022. **34**(4): p. 677-683.
47. Lim, B., et al., *Facile synthesis of bimetallic nanoplates consisting of Pd cores and Pt shells through seeded epitaxial growth.* 2008. **8**(8): p. 2535-2540.
48. Zhao, D., et al., *MXene (Ti3C2) vacancy-confined single-atom catalyst for efficient functionalization of CO2.* 2019. **141**(9): p. 4086-4093.

49. Grgur, B.N., et al., *Electrochemical oxidation of carbon monoxide: from platinum single crystals to low temperature fuel cells catalysts. Part I: Carbon monoxide oxidation onto low index platinum single crystals.* 2001. **66**(11-12): p. 785-797.

Chapter 5

Conclusion

Chapter 1

This chapter presented the motivation and objectives of this research project, as well as the structure of the dissertation.

Chapter 2

Chapter 2 had the literature review, starting with an overview of the general CO_{oxid} reaction and is then divided into sections and subsections. First, the contribution of different sources of Co pollution was discussed in details. Second, the effect of CO toxicity on human health at different concentration of Co in the air was presented. Furthermore, the effect of Co on the environment and plants is discussed. The 3 main reaction mechanisms for COoxid: (Langmuir-Hinshelwood (LH), Mars-van Krevelen (MvK)), and Eley-Rideal (ER) mechanisms) were explained. The CO_{oxid} catalytic reaction methods including thermal, photocatalytic, and electrochemical reactions were discussed with examples. The thermal method depends on external heating, the rate of CO conversion, catalyst type, loading amount, and gas flow rate. Various examples of different catalysts, like noble metals, metal oxides, and carbon-based materials, were discussed in detail as well as the effect of different reaction parameters on the catalyst efficiency . The Photocatalytic CO_{oxid} method depends on the generated (e^- and h^+), and the reaction rate is proportional to the rate generated photocurrent. TiO_2, CeO_2, and carbon materials are mostly used in photocatalytic COoxid. Furthermore, the electrochemical CO_{oxid} rate can be enhanced under photo-sources. In the case of using electrochemical COoxid, the CO molecules are converted to CO_2 under applied voltage in various pH and can indirectly be converted to valuable fuels. This method is essential for the catalysis used in the fuel cell. The effect of different factors on the CO_{oxid} activity and efficiency like shape, morphology catalyst type, loading amount, supporter type, and other factors were discussed. Additionally, A table for different CO_{oxid} catalysts, including structure, obtained current density, and the type of electrolyte was presented . A section was devoted to the parameters that can affect the CO_{oxid} activity of various methods with comparison and different examples. This was followed by another section for carbon-based nanomaterials, especially MXene, and their role in electrocatalytic COoxid. Due to the lack of experimental work on using Mxence in CO_{oxid} in the literature, only a summary of the previous theoritical work was presented. Herein, It is used for the first time in the electrochemical CO_{oxid} in wide PH concentrations as new low-cost novel materials. The chemical composition of MXene and its morphology were discussed in detail, and the different compositions besides the different preparation methods (direct and indirect HF etching) were discussed as well as why direct HF etching was used in this study.

Chapter 3

In brief, 2-D exfoliated MXene ($Ti_3C_2T_x$) (Tx = O, OH, and F) nanosheets decorated with Palladium ($Pd/Ti_3C_2T_x$) were successfully synthesized and used for the first time experimentally in the electrochemical

CO_{oxid} in acidic (0.1M $HClO_4$) at RE. Where the MAX phase ($Ti_3C_2T_x$) was etched by HF overnight, followed by the exfoliation using dimethyl sulfoxide anhydrous (DMSO) to form $Ti_3C_2T_x$ nanosheets. Then the precipitate was mixed with Pd salt (Na_2PdCl_4) under sonication, which led to the formation of Pd NPs with a size of around 10 nm and about 2.5 Wt %. Where the active Ti vacancies assist the reduction of Pd ions without using any reducing agent or stabilizer. XRD and XPS confirmed the formation of the fcc Pd structure without the formation TiO_2. The electrochemical CO_{oxid} for the Pd/$Ti_3C_2X_x$ in acidic $HClO_4$ gave a higher activity with a current density 0.318 mA cm^{-2} at a low oxidation potential 0.9V and stability with 85 % of its initial current density after IT test. The higher activity is attributed to the combination between the unique physicochemical merits and the outstanding catalytic properties of $Ti_3C_2T_x$ and Pd like higher electron density, synergism, rabid charge mobility, and rich active sites.

Chapter 4

Briefly, we successfully designed and fabricated exfoliated MXene $Ti_3C_2T_x$ (T_X=OH, O, and F) nanosheets ornate by PdPt nanoparticles (15 nm) (PdPt/$Ti_3C_2T_x$) for the electrochemical CO_{oxid} in different electrolytes (acidic, basic, and neutral) which is so far unprecedented. The preparation process comprises the etching of MAX (Ti_3AlC_2) by HF atRTto form 2-D $Ti_3C_2T_x$ nanosheets, then intercalation and exfoliation via using DMSO in an inert atmosphere under sonication. Thereafter, the formed Ti_3AlC_2 worked as a reducing agent for the in situ uniform growth of PdPt NPs over $Ti_3C_2T_x$ nanosheets. The highly reducing properties of $Ti_3C_2T_x$ due to highly active Ti single vacancies and defects resulting from the HF etching facilitate the reduction of Pd and Pt precursors (Na_2PdCl_4, Na_2PtCl_4) at RE. SEM and TEM were used to confirm the morphology structure, where the exfoliated multilayer 2D $Ti_3C_2X_x$ nanosheets decorated with spherical PdPt nanoparticles with (10 ± 2 nm) and its interlayer spacing between sheets is (60 nm ± 3) higher than Pt and Pd NPs (50 nm ± 3). TEM and HRTEM showed PdPt NPS gave uniform and ordered lattice fringes arranged in different directions (non-epitaxial growth) related to the alloying effect and arranged in one direction Pt and Pd. XRD and XPS confirm the chemical structure and stability of Ti3C2Tx, and no TiO2 is formed. The EDS and EDX confirm the surface atomic percentage, which showed both Pd and Pt less than 2%.

The electrochemical CO_{oxid} activity of PdPt/$Ti_3C_2T_x$ was substantially superior to Pd/$Ti_3C_2T_x$, Pt/$Ti_3C_2T_x$, and metal-free $Ti_3C_2T_x$ under all tested pH values, owing to the electronic effect and synergism displayed by the PdPt nanoparticles. The CO_{oxid} performance activity of PdPt/$Ti_3C_2T_x$ in $HClO_4$ is greater than that in $NaHCO_3$, and KOH under the same reaction conditions, due to the superior CO adsorption capacity in $HClO_4$, which is greater than that in $NaHCO_3$ and KOH. In the acidic $HClO_4$ medium. The $H_{ads/des}$ of PdPt/$Ti_3C_2T_x$ was significantly higher compared to the mono metals related to the presence of more accessible active sites and higher electroactive surface area (EASA), and the EASA of PdPt/$Ti_3C_2T_x$ was 1.34 times higher than Pd/$Ti_3C_2T_x$. Also, Pd and Pt suffer from instability in acidic electrolytes, and the CV showed no oxide peaks appeared for Pt-O, Pd-O, and Ti-O. The alloying effect stabilizes Pd/Pt against oxidation as well as improves the reaction kinetics at a lower potential. The CO_{oxid} potential was lower for PdPt/$Ti_3C_2T_x$ compared to Pd/$Ti_3C_2T_x$ with a higher current density by 3.33 times that, elucidating

$PdPt/Ti_3C_2T_x$ needs low energy for carrying a higher current density due to the quick reaction kinetics and low charge transfer resistance as proved by the low slope from the linear relationship of current density vs. $v^{1/2}$ and the EIS measurements. The durability test in the acidic medium after 2000sec showed good stability with losing current density of about only 17% for $PdPt/Ti_3C_2T_x$ compared to 25% for $Pd/Ti_3C_2T_x$. The losing related to the aggregation or degradation during the test, as proved by TEM images.

Interestingly, the $PdPt/Ti_3C_2T_x$ demonstrates a superior catalytic activity and stability in neutral $NaHCO_3$ and basic KOH solution too. $PdPt/Ti_3C_2T_x$ showed higher CO_{oxid} activity with current 2.9 and 4 times more than $Pd/Ti_3C_2T_x$ in neutral medium and basic medium respectively, and also at the lower applied potential for both mediums. That is related to the fast kinetic reaction and lower charge transfer resistance, as confirmed by the slope from the linear relationship of current density vs. $v^{1/2}$ and EIS measurements. The stability test (CA) was performed for 2000 sec and the current density for $PdPt/Ti_3C_2T_x$ decreased by 14% compared with 25% in the case of $Pd/Ti_3C_2T_x$ in a neutral medium, while it decreased by 10% for $PdPt/Ti_3C_2T_x$ and 75% for $Pd/Ti_3C_2T_x$ in basic medium. The alloying effect enhanced the stability of the catalyst towards the degradation in solution, especially in the basic medium, which superior improved both the stability and activity. The outstanding catalytic properties of alloying PtPd boost the charge transfer across the electrolyte/electrode interface at lower applied potential and higher CO_{oxid} activity with higher stability in the different mediums. According to these studies, it will pave the way for using $Ti_3C_2T_x$ or other MXenes structures for electrochemical CO_{oxid}.

Future Prospects

The great development in designing of various 2D-MXenes as (i.e., $W_{4/3}CT_x$, $Zr_3C_2T_x$, $Mo_2TiC_2T_x$, $Nb_4C_3T_x$, $V_4C_3T_x$, and $Nb_{4/3}CT_x$) via using different etchants as HF, NH_4HF_2 and HCl+ LiF, and NaF/LiF/KF with different concentration and high mass production. HF (50 %) is the most etchant used. Despite the great development in the synthesis of MXenes, the preparation methods used suffered from using several complex reaction steps, the etchant hazard effect, the long etching time (1-165 h), and stabilization by the addition of organic molecules as dispersant and stabilizers (i.e., hydrazine, TBAOH, DMSO, and urea). So it is crucial to develop new facile one-step or one-pot fabrication methods to qualify in practical applications. As well as varying engineering the morphology of MXene where the 2D shape is the most addressed for MXenes. The morphologies with diverse dimensional (i.e., 1D, 0D, and 3D) with different surface characteristics (i.e., branches, active sites, cavities porosity, and multiple adsorption sites) with superior properties like high activated surface area within low density need to be studied to choose the best MXene based structure to maximize the catalytic CO_{oxid} activity in a wide PH range with long term electrocatalytic stability. Also, computational simulation should be studied side by side with the experimental results for more understanding of the relationship between CO_{oxid} performance and the structure of MXene-based catalysts electrochemically in addition to their mechanism or pathway.

In contrast, Pt-based catalysts with different structures are the most efficient catalyst for the CO_{oxid}, which

is essential in various industrial applications, especially in fuel cell applications. However, it suffers from CO poisoning as well as the high production cost of Pt-based catalysts. The tailoring of different architectures of Pt-based with 0,1, 2, and 3-dimensional nanostructure combined with the MXene with different structures is highly important to enhance the activity and long-term stability in the electrochemical CO_{oxid} for their utilization in large-scale in the industry. In addition, it is important to enlarge facial, one-step methods in an aqueous medium under ambient conditions in a high yield for the rational engineering of multimetallic Pt-based nanocrystals with multiplicity in bulk/surface features (i.e., branches, cavities, porosities, and defects) and unique catalytic merits (i.e., fast mass transfer, stability against aggregation, easy activation, good adsorption capacity of reactants, and great tolerance for intermediates). Furthermore, the engineering of binary and ternary Pt-based nanocrystals with core-shell, alloy, and branched could agree to scalability as their outstanding mixed catalytic advantages via strain, synergistic, and electronic interaction.

The hiatus between industrial utilization of MXene-based/Pt-based catalysts and research should be filled by combining experimental and theoretical studies to get a well understanding of the composition/shape-related properties of catalysts and their mechanism and prediction of their behavior based on model interactions or operation conditions.